DEVELOPMENTS IN FORCE DETECTION:

INTEGRATED CANTILEVER MAGNETOMETRY AND

ELECTRIC FORCE MICROSCOPY OF

ORGANIC SEMICONDUCTORS

A Dissertation

Presented to the Faculty of the Graduate School

of Cornell University

in Partial Fulfillment of the Requirements for the Degree of

Doctor of Philosophy

by

Tse Nga Ng

May 2006

DEVELOPMENTS IN FORCE DETECTION:

INTEGRATED CANTILEVER MAGNETOMETRY AND

ELECTRIC FORCE MICROSCOPY OF

ORGANIC SEMICONDUCTORS

Tse Nga Ng, Ph.D.

Cornell University 2006

The first part of this thesis will present integrated cantilever magnetometry, which determines the average magnetization and low-frequency thermomagnetic fluctuations of single sub-micron magnets in order to evaluate their suitability for magnetic resonance force microscopy (MRFM). With a custom-built, cryogenic frequency-shift magnetometer, magnets of different sizes and materials are measured and compared to find the parameters that would minimize magnetic dissipation and fluctuations. Our measurements indicate that for proton MRFM, a magnet with low anisotropy is preferable because its low-frequency thermomagnetic fluctuations are more easily damped by high applied fields.

The second part of this thesis will investigate organic semiconductors by electric force microscopy (EFM), which provides microscopic insights essential for understanding the processes of device degradation, charge injection, and charge transport. EFM has identified two distinct degradation mechanisms; operation at elevated temperatures and crystallization both lead to higher contact resistance, despite that the bulk mobility is improved by the former and decreased by the later.

Using a custom-built variable temperature microscope, charge injection into a molecularly doped polymer system is studied and interpreted in terms of ener-

getic disorder. The temperature-dependent disorder contribution is readily distinguished from the mobility effect in the injected current by comparing the current density at the injecting and extracting electrodes. The field-assisted barrier lowering is more efficient than expected from the Schottky theory due to energetic disorder. Direct potential and electric-field measurements allow the injected charge density to be inferred, and it does not follow simple Arrhenius behavior. This can be explained by incorporating energetic disorder into the activation energy.

We also have explored charge trapping in molecularly doped polymers, which may appear trap-free at the short-time scale probed by time-of-flight studies. However, deep traps do exist and their release kinetics and diffusion is observed with EFM. For polymeric semiconductors, the kinetics of trap formation and dissociation are measured in organic field-effect transistors with different processing parameters for the semiconductor/dielectric interfaces, to determine how trap energies are affected by processing. Trap formation and dissociation is faster for devices with octadecyl-trichlorosilane interfaces than for devices with untreated silicon oxide interfaces. Compared to polycrystalline pentacene, the trap distribution is more spatially homogeneous in polymers, regardless of the dielectric surface treatments.

BIOGRAPHICAL SKETCH

Tse Nga Ng was born in Hong Kong on the longest day of the year (the summer solistice) in 1980. She is the youngest daughter of Kwok Keung Ng and Hoi Ngan Poon, and she has an older sister, Tze Wan Ng. Her family moved to Saipan when she was eleven, due to the uncertainties arising from the British handover of Hong Kong to China. Saipan is a beautiful tropical island in the Pacific Ocean, near the Marianas Trench which is the deepest place in the earth's crust. It is an English-speaking place, and there her name has morphed into Tina. Since Saipan is part of a US commonwealth and follows the American education system, Tse Nga/Tina chose to attend college in the United States. She went to Knox College, Galesburg, IL, where she was inspired by Professor Larry Welch to study chemistry and undertake research. She decided to attend graduate school at Cornell University and joined Professor John Marohn's laboratory, because he is always excited about science. In the last year of graduate school, Tse Nga was fortunate to have the chance to intern at Palo Alto Research Center, and upon graduation she will take up a postdoctoral position there.

ACKNOWLEDGEMENTS

I thought this acknowledgements section is going to be easier to write than the other parts of my thesis, but it is not true at all. I cannot express enough my infinite gratitude for all the support and guidance that I have received from so many good people, without whom this thesis could never exist. I really really thank John for being a great advisor, for helping me to grow both in science and in life. You set high standards for us, but at the same time your enthusiasm is so contagious I never feel hopeless. I have learned so much from you, from the cool math tricks to the "old white man" test for an exciting introduction. I will always check extreme cases too, after any derivations. Thank you for being very kind, supportive, and patient!

My colleagues in the Marohn group are unbelievably awesome. Bill Silveira, Sean Garner, and Erik Muller have been the pioneers of our lab, and they not only built up the lab but also set up a fun atmosphere. They helped me so much, and even left me an inheritance of a painstaking probe (thanks Bill!). I had a great time laughing at puns (Sean), chatting with Bill across the diagonal computer desks (this applies to Seppe too), and looking at cute cat pictures (Erik). Neil Jenkins has been my supplier of cantilevers for a long while; thanks Neil, for motivating me to watch more movies too! Seppe Kuehn and Jahan Dawlaty have been my helium-filling associates. I need to thank them not just for that but also for many interesting conversations, from scientific topics (Seppe always helps!) to other crazy subjects like attending a wedding with machine guns (Jahan). Michael Jaquith, Showey Yazdanian, and Steve Hickman represent the bright future of the Marohn group. Showey, thanks for your questions, they always make me think. I wish all of my colleagues the best, and I am sure they will be good at whatever profession they choose, be it a scientist/professor or medical doctor.

The "Chinese" girls in chemistry, Bao Hailing, Yuan Min, and Wu Min, are my support system through thick and thin. The computer scientists, Pang Bo (my lovely roommate), Guo Lin, and Wang Yanling, always bring happy dinner memories. Girls, you help me grow so much, as we travel together and explore museums, national parks, restaurants, movies, TV programs, etc. It is amazing how we are compatible given the opposite personalities, from very organized to care-free, from emotional to logical. You are very kind, considerate, and giving, and I am so lucky to be your friend. I also want to thank Jenny Oaksmith, Dan Baird, and Mark Witinski, for being nice and very funny. Janny Thipphogprahas, my dear, you always provide me ears when I need to complain, and I cherish all the fun we had together.

My parents are unconditionally supportive no matter what I do, and I am so grateful for their love. I still remember all the poker games we played at night when I was a kid, when Dad's excuse for that was that it would make us less afraid of math. I think it worked. Mom has always been my source of wisdom, and my sister is the cool one from whom I rub off some reasonable fashion sense. How I want to go shopping with you right now!

Hmm, Mark, which paragraph should I put you in? I will let you have one all by yourself, just for you~ Thanks for proofreading my whole thesis, and I cannot make it through without all your cyber hugs, quiet calls, and dinner reminders.

I thank the staff at Palo Alto Research Center (PARC); they are examples of good industrial scientists. I also acknowledge the professors who have helped me analyze my data: George Malliaras, Dave Dunlap, and Sergey Novikov. My work was supported by Cornell University, the Army Research Office, and the National Science Foundation. It was done with the help of excellent facilities in the Cornell Nanoscale Science and Technology Facility, the Cornell Center for

TABLE OF CONTENTS

LIST OF FIGURES

LIST OF TABLES

Chapter 1

Introduction to cantilever magnetometry

Applications of sub-micron magnets in spintronics, quantum computing, and data storage continue to demand a critical look at magnetic behavior. One particularly promising application is single-spin MRFM [1], in which magnetic resonance is registered as a change in the force between a sample spin and a magnet attached to the tip of a cantilever. A force-gradient approach has been demonstrated to detect nuclear magnetic resonance with a sensitivity of $\sim 10^6$ protons using a magnetic tip of 9 µm diameter [2]. Calculations show that reduction of the tip size to 0.5 µm can increase sensitivity to $\sim 10^3$ protons. So to improve MRFM sensitivity, low spring-constant cantilevers with sub-micron nickel magnets have been fabricated using a modified version of the process developed by Stowe *et al.* [3, 4]. The use of Ni allows batch fabrication and avoids the time-consuming manipulation required by high anisotropy materials (Sm_5Co_{17}, $Pr_{12}Fe_{14}B$), which were individually glued and then milled to the preferred dimensions by a focused ion beam [5].

While batch fabrication makes more reproducible magnetic tips with higher resolution, there are possible problems with these modified cantilevers. First, it is not clear if the nickel magnets are adequately protected from oxidation during processing steps. Second, simulations [6, 7] have shown that magnetic fluctuations due to the vibrating cantilever can cause an undesirable faster relaxation rate of the sample spins. Since nickel has lower anisotropy than Sm_5Co_{17} or $Pr_{12}Fe_{14}B$, it needs to be determined whether the fluctuations from a nickel tip will be acceptable. Both problems are elucidated by cantilever magnetometry, which determines the average magnetization and low-frequency thermomagnetic fluctuations of sin-

gle sub-micron magnets in order to evaluate their suitability for future MRFM experiments.

A micromachined silicon cantilever is a very sensitive sensor that can measure forces as small as 6 aN [3]. Cantilever magnetometry has previously been shown to be a sensitive technique for the study of ferromagnetic tips used in magnetic/magnetic resonance force microscopes [8–11], single particles [12–15], and thin films [16]. This characterization technique has the ability to measure magnetic properties of individual particles over a large range of temperatures. Commercial superconducting quantum interference devices (SQUIDs), with minimum detectable magnetic moments of $\sim 10^{-12}\,\mathrm{Am}^2$, do not have the sensitivity to measure an individual sub-micron magnet, although integrated SQUIDs are capable of detecting quantum effects in nanoscale particles [17, 18]. Cantilever magnetometers have been used to study magnetization reversal [19], magnetic anisotropy and magnetostriction [20, 21], as a paramagnetic oxygen sensor [22], and to investigate 2D electron gases [23, 24] and superconductors [25, 26]. Because cantilever magnetometry measures small-angle fluctuations at low frequencies [15,27], it complements ferromagnetic resonance spectroscopy, which detects fluctuations at the Larmor frequencies (typically range between $50-300\,\mathrm{MHz}$). Our magnetic cantilevers are integrated magnetometers, in which magnetic properties are inferred from the force generated by the interaction between each sub-micron magnet and the external field. This chapter will discuss the principles of cantilever magnetometry, which has been applied to address our specific concern— whether our custom magnetic cantilevers are suitable for use in magnetic resonance force microscopy (MRFM) [1, 28–31].

In this thesis two types of cantilever magnetometry, a frequency-shift technique and an alternating force gradient method, have been explored. Frequency-shift

magnetometry is more sensitive than the alternating force gradient method and is able to measure transverse magnetic fluctuations, but it is limited to samples with anisotropy. For spherical or paramagnetic samples, an alternating force gradient magnetometer will be necessary [8, 22, 32–34].

1.1 Frequency-shift magnetometry

In frequency-shift cantilever magnetometry, the sample is attached to the tip of a cantilever, which is driven into motion at its resonant frequency [12, 13, 15]. When an external magnetic field $\boldsymbol{B}$ is applied, the cantilever tip experiences a torque coupling ($\boldsymbol{\tau} = \boldsymbol{\mu} \times \boldsymbol{B}$) due to the shape or the crystalline anisotropy[*] of the magnet with magnetization $\boldsymbol{\mu}$. A torque about the direction of the cantilever width is kinematically equivalent to a force in the direction of the thickness, $F_t = \tau_w \alpha/l$, which gives $F_t = \mu_t B_l \alpha/l$, where l is the length of the cantilever and $\alpha = 1.377$ for a beam cantilever [30]. This force effectively changes the cantilever spring constant and in turn shifts the cantilever resonant frequency. Thus by measuring frequency the magnetization can be inferred. Compared to torque detection [35], frequency-shift magnetometry does not directly measure magnetization hysteresis; later we will present a detailed procedure for recovering the magnetization hysteresis and caution about potential measurement artifacts in Chapter 2.

1.1.1 Instrumentation

Experiments were carried out at a pressure of $\leq 10^{-5}$mbar and at a temperature of 4.2K. Details of the custom-built cryogenic apparatus can be found in Appendix B. A magnetic field was applied along the length of each cantilever [Fig. 1.1(a)], and the field-dependent resonance frequency f and quality factor Q were measured

---

[*]See Appendix A for details on anisotropy and demagnetizing field

as the applied field was swept from -6 to $+6$ T. The cantilever was capacitively driven into motion by applying a voltage to a nearby wire [3]; the driving allowed us to measure the frequency of the cantilever by making it the resonant element in a positive feedback loop [36, 37]. We typically set the amplitude of oscillation to a zero-field value of $x_0 = 90$ nm and simultaneously record the steady-state frequency and cantilever amplitude at constant drive. For each cantilever in zero field, the intrinsic resonance frequency f_0 and quality factor Q_0 were inferred from cantilever ring-down transients ($Q_0 = \pi f_0 \tau$, where τ is the amplitude decay time), while the spring constant k_0 was obtained by measuring thermomechanical position fluctuations with a fiber optic interferometer [38, 39]. For the magnets measured here, the shift in cantilever resonance frequency versus magnetic field for a magnetic cantilever was at least thirty times larger than the shift for bare Si or Si_3N_4 cantilevers [Fig. 1.1(b)]. Tip magnetization was inferred from the frequency-shift data as detailed in Chapter 2.

Besides magnetization, we also computed the magnetic friction $\Gamma_m = \Gamma(B) - \Gamma(0)$ from Q, using $\Gamma = 2\pi f m / Q$ where $m = k_0/(2\pi f_0)^2$ is the cantilever effective mass. Cantilever Q was obtained by either recording the ringdown transients ($Q = \pi f \tau$) or measuring the steady-state cantilever amplitude x at constant drive ($Q = x Q_0 / x_0$) [40, 41]. The first method yielded absolute Q but required a waiting time longer than the amplitude decay time τ; the second method was much faster but gave only relative Q, which might require correction for interferometer drifts. The second method was used here [Fig 1.2(a)]; the result was checked by taking ringdown transients at several magnetic fields.

Frequency-shift cantilever magnetometry is more sensitive for measuring magnetization than for detecting magnetic friction. The magnetic cantilever shows a frequency response at least thirty times larger than a bare cantilever [Fig. 1.1(b)]
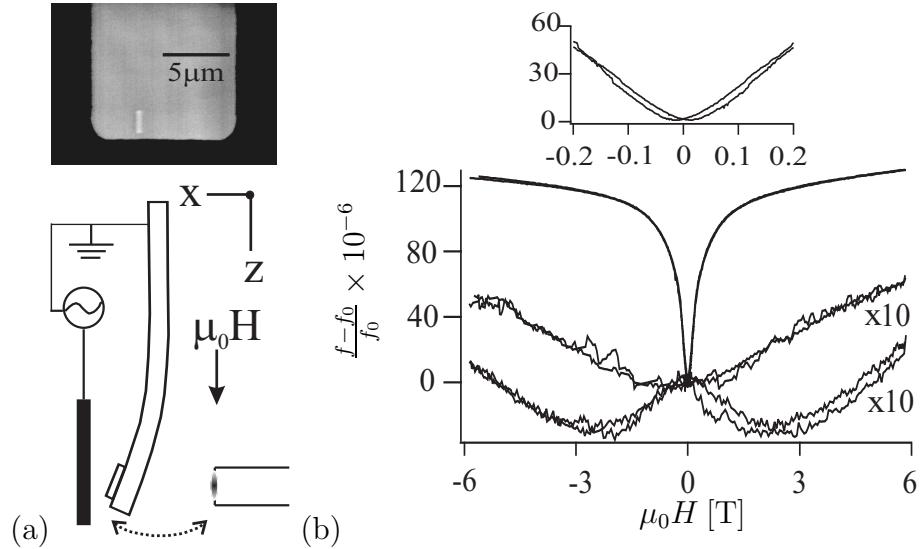
Figure 1.1: (a) Top: SEM image of a cantilever tip with Ni magnet. Bottom: schematic of the frequency-shift cantilever magnetometer, showing capacitive drive wire (left) and optical fiber (right). (b) Cantilever frequency shift versus applied magnetic field. Upper curve: cantilever with magnet ($200\mu m \times 10\mu m \times 0.34\mu m$, $f_0 = 10863\,Hz$, $k_0 = 5.8\,mN\,m^{-1}$, and $Q_0 = 19000$; magnet dimensions $= 1310\,nm \times 680\,nm \times 200\,nm$). Middle curve: bare Si_3N_4 cantilever ($200\mu m \times 10\mu m \times 0.60\mu m$, $f_0 = 19198\,Hz$, $k_0 = 20\,mNm^{-1}$, and $Q_0 = 1000$). Lower curve: bare silicon cantilever ($200\mu m \times 10\mu m \times 0.34\mu m$, $f_0 = 8087\,Hz$, $k_0 = 1.6\,mNm^{-1}$, and $Q_0 = 11500$). The inset zooms in on the hysteretic part of the upper curve.
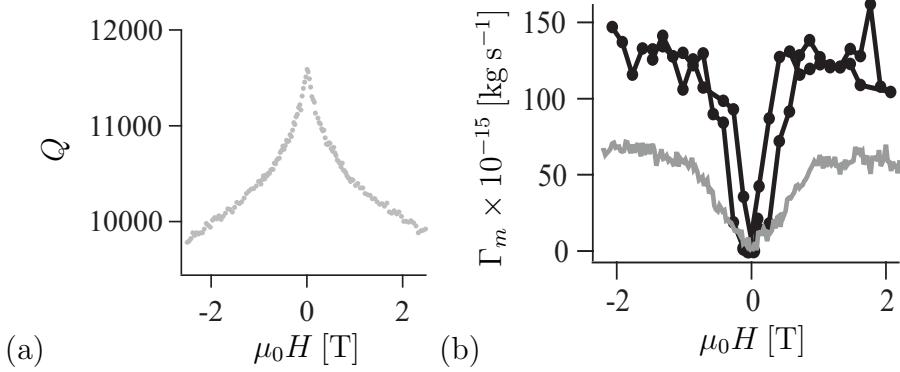
Figure 1.2: (a) Quality factor versus applied magnetic field for a bare silicon cantilever. (b) Magnetic friction versus applied magnetic field. Upper curve: cantilever with magnet. Lower curve: bare silicon cantilever. These cantilevers are same as the ones in Fig. 1.1.

while its magnetic friction is only three times that of a bare cantilever [Fig. 1.2(b)]. The sensitivity of these measurements are limited by thermal force fluctuations [3]. In the following section, we will derive the scaling laws for magnetization and magnetic friction in terms of cantilever dimensions and material parameters.

1.1.2 Scaling laws for minimum detectable magnetization and magnetic friction

Because the magnetization, or magnetic moment, is inferred from the induced changes in a cantilever spring constant, the minimum detectable magnetic moment is derived from the minimum detectable spring constant change $k_{m,\min} = \sqrt{2}F_{\min}/x_{\mathrm{pk}}$, where x_{pk} is the cantilever peak displacement and $F_{\min}$ is the minimum detectable force [36, 37, 42]. $F_{\min}$ is given by

$$F_{\min} = S_F(b)^{1/2} = \left(\frac{2\,k\,k_B T}{\pi Q f}\right)^{1/2} (b)^{1/2},\qquad(1.1)$$

where T is temperature in Kelvin, k_B is Boltzmann's constant, b is the measurement bandwidth, and S_F stands for thermomechanical force spectral density.

The magnetic contribution [13, 15] to the cantilever spring constant is

$$k_m = \left(\frac{\alpha}{l}\right)^2 \mu B \frac{\mu_0 \mu \Delta N/V}{B + \mu_0 \mu \Delta N/V}, \tag{1.2a}$$

where $\alpha = 1.377$ for a beam cantilever [30], l is the length of the cantilever, μ is the tip magnetization, $B = \mu_0 H$ is the applied magnetic field, $\mu_0 = 4\pi \times 10^{-7}$ Tm/A is the free-space permittivity, V is the volume of the magnetic particle, and $\Delta N = N_t - N_l$ is the difference in the tip's demagnetization factors along the direction of the cantilever's thickness and length [43]. At high field where we can assume that $B \gg \mu_0 \mu \Delta N/V$ and that the magnet is saturated, the spring constant expression takes on the limiting value

$$k_m = \left(\frac{\alpha}{l}\right)^2 \mu_s B_s \Delta N, \tag{1.2b}$$

where $B_s = \mu_0 \mu_s / V$ is the saturation field and μ_s is the saturation magnetization. It follows that

$$\mu_{\min} = \left(\frac{l}{\alpha}\right)^2 \frac{k_{m,\min}}{B_s \Delta N} = \left(\frac{l}{\alpha}\right)^2 \frac{\sqrt{2} F_{\min}}{B_s \Delta N x_{\mathrm{pk}}}. \tag{1.3}$$

$F_{\min}$ can be written in terms of cantilever dimensions and material parameters. The resonance frequency and spring constant for a beam cantilever of length l, width w, and thickness t are

$$f_0 = \frac{3.516}{2\pi} \frac{t}{l^2} \left(\frac{E}{12\rho}\right)^{1/2}, \tag{1.4}$$

$$k = 0.2575 \frac{Ewt^3}{l^3}, \tag{1.5}$$

where E is Young's modulus and ρ is the density ($E = 1.9 \times 10^{11}$ N m^{-2} and $\rho = 2.3 \times 10^3$ kg m^{-3} for silicon). In terms of cantilever properties, Eq. 1.1 can be recast as

$$F_{\min} = 1.007 \left(\frac{k_B T}{Q}\right)^{1/2} (\rho E)^{1/4} \left(\frac{w}{l}\right)^{1/2} t(b)^{1/2}. \tag{1.6}$$

In terms of cantilever properties, the minimum detectable magnetic moment is

$$\mu_{\min} = \frac{1.424}{\alpha^2 B_s \Delta N x_{\mathrm{pk}}} \left(\frac{k_B T}{Q}\right)^{1/2} (\rho E)^{1/4} w^{1/2} l^{3/2} t(b)^{1/2}. \tag{1.7}$$

The minimum detectable magnetic moment decreases (and therefore improves) with increasing amplitude of cantilever oscillation. For best magnetic moment sensitivity, the cantilever should be made thin, narrow, and short, whereas the cantilever needs to be long for maximum force sensitivity. For our most sensitive cantilever at $4.2\,\mathrm{K}$ (cantilever C3 in Table 2.1), the smallest detectable Ni magnet at 1 Hz bandwidth is projected to have a volume of $360 \times 10 \times 10\,\mathrm{nm}^3$, assuming that bulk magnetic behavior applies[†].

The thermal limit for detecting magnetic friction is $\Gamma_{m,\mathrm{min}} = \sqrt{2}F_{\mathrm{min}}/2\pi f x_{\mathrm{pk}}$ [15, 40]. In terms of cantilever properties, the minimum detectable magnetic friction is

$$\Gamma_{m,\mathrm{min}} = \frac{1.403}{x_{\mathrm{pk}}}\left(\frac{k_B T}{Q}\right)^{1/2}\left(\frac{\rho^3}{E}\right)^{1/4} w^{1/2} l^{3/2}(b)^{1/2}. \tag{1.8}$$

In contrast to F_{min} and μ_{min}, $\Gamma_{m,\mathrm{min}}$ does not depend on cantilever thickness. The Γ_m signal due to the magnetic cantilever in Fig.1.2 is close to the limit of detection. For this sample at ±6 T, the signal to noise ratio is $S_\mu/\mu_{\mathrm{min}}(1\,\mathrm{Hz}) \sim 120$ for the magnetic moment and $S_{\Gamma_m}/\Gamma_{m,\mathrm{min}}(1\,\mathrm{Hz}) \sim 3$ for the magnetic friction.

1.2 Alternating gradient force magnetometer

For samples with low anisotropy such as spherical particles or paramagnetic materials, the torque coupling might be undetectable with the frequency-shift technique. Instead, these samples can be measured by an alternating gradient force magnetometer, where an oscillating magnetic field gradient induces an alternating force at the tip of a cantilever via $\boldsymbol{F} = \boldsymbol{\mu}\nabla\boldsymbol{B}$. The force signal is amplified by the mechanical quality factor because the field gradient is oscillating at cantilever

---

[†]See Appendix C for the critical size and temperature at which superparamagnetic particles transition to stable magnets.
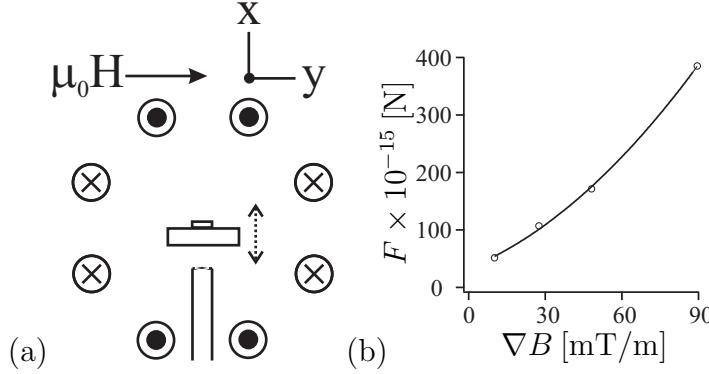
Figure 1.3: (a) Schematics of the alternating gradient force magnetometer. The eight wires are essentially a quadrupole with currents going into and out of the page, and the optical fiber is at the bottom slot between wires. (b) Spurious response from a bare Si cantilever ($500\ \mu\text{m} \times 10\ \mu\text{m} \times 0.34\ \mu\text{m}$, $f_0 = 1640$ Hz, $k_0 = 0.15$ mN m^{-1}, and $Q_0 = 300$).

resonance frequency. The cantilever displacement is detected to infer the sample's magnetization.

1.2.1 Instrumentation

Figure 1.3(a) shows our magnetic field gradient produced by parallel wires running opposite currents arranged essentially as a quadrupole coil [44] whose magnetic field components are

$$B_x = \frac{\mu_0 I}{2a^2}y,\ B_y = \frac{\mu_0 I}{2a^2}x,\ B_z \approx 0, \tag{1.9}$$

where I is the magnitude of the current delivered to the coil, and a is the coil radius. At each field point, the cantilever resonant frequency is obtained by a ringdown transient. Then the field gradient is turned on at the resonant frequency at a fixed current, and the cantilever amplitude is measured by a fiber optic interferometer.

The above steps are repeated for the next field point until a hysteresis curve is obtained.

In a control experiment at zero field, a bare cantilever is observed to be coherently driven; this spurious response increases quadratically with the current [Fig. 1.3(b)] and is much larger than the expected magnetic signal. It is suspected that the spurious response is due to heating, which is proportional to power ($P \propto I^2$). After the gradient coil diameter has been increased to alleviate heating, the spurious response still overwhelms the magnetic signal. When an external field of 20 mT is applied, the cantilever is displaced over an interferometer fringe of 390 nm. We decide to not pursue this gradient force method for the time being but return to frequency-shift magnetometry, for which we have made certain that our results are free from artifacts.

1.2.2   Scaling law in terms of magnetic gradient

For comparison to frequency-shift magnetometry, we will derive the magnetic moment sensitivity in terms of the parameters describing a gradient coil. The magnitude of the gradient G produced by a quadrupole coil is $G = \mu_0 I/2a^2$. Suppose the coil is wound out of wire of radius b. In terms of current density, $I = \pi b^2 \sigma$, where σ has units of A/m^2. Let the wire radius be written as a fraction β of the coil diameter: $b = \beta a$ so $\beta < 1$ is a unitless parameter, and we have

$$G = \frac{\mu_0}{2}\pi\beta^2\sigma \tag{1.10}$$

This is remarkable: for any quadrupole coil constructed with a given ratio of coil to wire radius, the magnetic field gradient produced is the same and independent of scale when operated at a given current density.

Since the force on a cantilever is $F = \mu G$, the magnetic moment spectral density is equivalent to the thermomechanical force spectral density divided by

the gradient,

$$S_\mu = \frac{1}{G} S_F = \frac{2}{\mu_0 \pi \beta^2 \sigma} \times F_{\min}(b)^{-1/2}. \tag{1.11}$$

Here the sensitivity is the same as Eq. 1.3 when

$$\frac{2}{\mu_0 \pi \beta^2 \sigma} = \left(\frac{l}{\alpha}\right)^2 \frac{\sqrt{2}}{B_s \Delta N x_{\text{pk}}}. \tag{1.12}$$

Between the two techniques, frequency-shift magnetometry has better sensitivity due to the high external field and short cantilevers in our experimental setup. To achieve the same $\mu_{\min}$ as the magnetic cantilever in Fig. 1.1, an alternating gradient force magnetometer needs $\beta^2 \sigma$ to be $4.6 \times 10^5 \text{A/m}^2$, a very demanding requirement to meet!

1.3   Summary

Two types of cantilever magnetometry have been examined. Analysis of frequency-shift detection shows that cantilevers should be thin, narrow, and short for maximum sensitivity, in contrary to alternating gradient force magnetometry in which cantilevers should be long for highest sensitivity. Unlike magnetization and force, the minimum detectable magnetic friction does not depend on cantilever thickness. The frequency-shift method is chosen to investigate the suitability of our custom magnetic cantilevers for use in MRFM experiments.

CHAPTER 1 REFERENCES

[1] D. Rugar, R. Budakian, H. J. Mamin, and B. W. Chui, Nature **430**, 329 (2004).

[2] S. R. Garner, S. Kuehn, J. M. Dawlaty, N. E. Jenkins, and J. A. Marohn, Appl. Phys. Lett. **84**, 5091 (2004).

[3] T. D. Stowe et al., Appl. Phys. Lett. **71**, 288 (1997).

[4] N. E. Jenkins et al., J. Vac. Sci. Tech. B **22**, 909 (2004).

[5] B. C. Stipe et al., Phys. Rev. Lett. **87**, 277602 (2001).

[6] J. D. Hannay, R. W. Chantrell, and D. Rugar, J. Appl. Phys. **87**, 6827 (2000).

[7] D. Mozyrsky, I. Martin, D. Pelekhov, and P. C. Hammel, Appl. Phys. Lett. **82**, 1278 (2003).

[8] G. A. Gibson and S. Schultz, J. Appl. Phys. **69**, 5880 (1991).

[9] G. P. Heydon, A. N. Farley, S. R. Hoon, and M. S. V. adn S. L. Tomlinson, IEEE Trans. Magn. **33**, 4059 (1997).

[10] Z. Zhang and P. C. Hammel, IEEE Trans. Magn. **33**, 4047 (1997).

[11] C. W. Miller, U. M. Mirsaidov, T. C. Messina, Y. J. Lee, and J. T. Markert, J. Appl. Phys. **93**, 6572 (2003).

[12] C. Rossel et al., J. Appl. Phys. **79**, 8166 (1996).

[13] J. A. Marohn, R. Fainchtein, and D. D. Smith, Appl. Phys. Lett. **73**, 3778 (1998).

[14] C. Lupien, B. Ellman, P. Grutter, and L. Taillefer, Appl. Phys. Lett. **74**, 451 (1999).

[15] B. C. Stipe, H. J. Mamin, T. D. Stowe, T. W. Kenny, and D. Rugar, Phys. Rev. Lett. **86**, 2874 (2001).

[16] J. Moreland, J. Phys. D: Appl. Phys. **36**, R39 (2003).

[17] D. D. Awschalom, D. P. DiVincenzo, and J. F. Smyth, Science **258**, 414 (1992).

[18] W. Wernsdorfer and R. Sessoli, Science **284**, 133 (1999).

[19] L. Gao et al., J. Appl. Phys. **95**, 7010 (2004).

[20] J. Morillo, Q. Su, B. Panchapakesan, M. Wuttig, and D. Novotny, Rev. Sci. Instrum. **69**, 3908 (1998).

[21] S. C. Masmanidis et al., Phys. Rev. Lett. **95**, 187206 (2005).

[22] K. R. Thurber, L. E. Harrell, and D. D. Smith, J. Appl. Phys. **93**, 4297 (2003).

[23] M. P. Schwartz, D. Grundler, I. Meinel, C. Heyn, and D. Heitmann, Appl. Phys. Lett. **76**, 3564 (2000).

[24] J. G. E. Harris et al., Phys. Rev. Lett. **86**, 4644 (2001).

[25] R. D. Biggar and J. M. Parpia, Rev. Sci. Instrum. **69**, 3558 (1998).

[26] C. A. Bolle et al., Nature **399**, 43 (1999).

[27] J. G. E. Harris et al., Appl. Phys. Lett. **82**, 3532 (2003).

[28] D. Rugar, C. S. Yannoni, and J. A. Sidles, Nature **360**, 563 (1992).

[29] D. Rugar et al., Science **264**, 1560 (1994).

[30] J. A. Sidles et al., Rev. Mod. Phys. **67**, 249 (1995).

[31] S. R. Garner, *Force and Force-gradient Detection of Nuclear Magnetic Resonance*, doctoral dissertation, Cornell University, 2005.

[32] P. J. Flanders, J. Appl. Phys. **63**, 3940 (1988).

[33] M. Todorovic and S. Schultz, Appl. Phys. Lett. **73**, 3595 (1998).

[34] M. D. Michelena, P. Sanchez, E. Lopez, M. C. Sanchez, and C. Aroca, J. Magn. Magn. Mater. **215-216**, 677 (2000).

[35] M. Lohndorf, J. Moreland, P. Kabos, and N. Rizzo, J. Appl. Phys. **87**, 5995 (2000).

[36] T. R. Albrecht, P. Grutter, D. Horne, and D. Rugar, J. Appl. Phys. **69**, 668 (1991).

[37] E. M. Muller, *Electric Force Microscopy of Charge Trapping in Thin-film Pentacene*, doctoral dissertation, Cornell University, 2005.

[38] D. Rugar, H. J. Mamin, and P. Guethner, Appl. Phys. Lett. **55**, 2588 (1989).

[39] J. L. Hutter and J. Bechhoefer, Rev. Sci. Instrum. **64**, 1868 (1993).

[40] P. Grutter, Y. Liu, P. LeBlanc, and U. Durig, Appl. Phys. Lett. **71**, 279 (1997).

[41] Y. Liu and P. Grutter, J. Appl. Phys. **83**, 7333 (1998).

[42] W. R. Silveria, *Microscopic View of Charge Injection in a Model Organic Semiconductor*, doctoral dissertation, Cornell University, 2005.

[43] A. Aharoni, J. Appl. Phys. **83**, 3432 (1998).

[44] G. Odberg and L. Odberg, J. Magn. Res. **16**, 342 (1974).

Chapter 2

Frequency-shift cantilever magnetometry

Individual sub-micron magnets were studied by cantilever magnetometry. The time-averaged magnetization and the low-frequency thermomagnetic fluctuations were measured as a function of particle shape and composition. The measured magnetization fluctuations were used to predict a particle's magnetic field fluctuations, which were in turn used to estimate the effect of a magnetic tip on the relaxation times of sample spins (protons or electrons) in a magnetic resonance force microscopy experiment. The magnetometry results for a gold-nickel wire have alerted us to correct for experimental artifacts, and the corrections are discussed here so that systematic errors can be avoided in the future.

2.1   Magnetization hysteresis

Ultrasensitive cantilevers with Ni magnets were fabricated using a modified version of the process developed by Stowe *et al.* [1, 2]. The Ni magnets were deposited by thermal evaporation and found to be polycrystalline with grain sizes of $100 - 200$ nm and a surface roughness of approximately 9 nm. A series of magnetic tipped cantilevers (C1−C5 in Table 2.1) were prepared to evaluate the effect of magnet size and shape on magnetic properties. To discern whether oxide formation during processing is a concern, the magnet on cantilever C5 was capped with 5 nm of Cr to prevent oxidation. Cantilever frequency and quality factor were measured as a function of magnetic field in high vacuum ($\leq 10^{-5}$ mbar) at 4.2 K as described in Section 1.1.1.

Table 2.1: Cantilever and magnet parameters. (A) Cantilever length, width, and thickness. (B) Cantilever properties at zero field. (C) Magnet dimensions: length and width were measured by SEM (± 30 nm), and thickness was measured by AFM (± 10 nm). (D) Summary of static magnetic properties.

		C1	C2	C3	C4	C5	
A.	l	200	125	200	300	300	μm
	w	10	4	7	4	4	μm
	t	340	340	340	340	340	nm
B.	f_0	10863	16920	14940	4180	4090	Hz
	k_0	5.8	4.9	8.6	0.43	0.30	mN m^{-1}
	Q_0	19000	8000	34000	45000	41000	–
C.	l_m	1310	11070	870	2440	1640	nm
	w_m	680	990	2020	4410	3730	nm
	t_m	200	125	200	125	125	nm
D.	Δf	3.50	131.3	6.65	79.5	55.9	Hz T^{-1}
	ΔB	0.43	0.53	0.33	0.47	0.40	T
	μ_s	79	627	162	776	389	fA m^2
	ΔN	0.76	0.92	0.57	0.65	0.66	–
	B_s	0.56	0.58	0.58	0.72	0.64	T

Tip magnetization is inferred from the frequency-shift data as follows. Using the tip-field interaction model of [3, 4],

$$f - f_0 \approx \Delta f \, \frac{B \, \Delta B}{B + \Delta B}, \tag{2.1}$$

where

$$\Delta f = \frac{f_0}{2k_0} \left(\frac{\alpha}{l}\right)^2 \mu, \tag{2.2}$$

$$\Delta B = \mu_0 \mu \frac{\Delta N}{V}. \tag{2.3}$$

The approximation holds when $f/f_0 \approx 1$, which is the case in our measurements. In Eqs. 2.1–2.3, $B = \mu_0 H$ is the applied magnetic field, $\alpha = 1.377$ for a beam cantilever [5] of length l, μ is the tip magnetization, $\Delta N = N_t - N_l$ is the difference in the tip's demagnetization factors along the direction of the cantilever's thickness and length [6], and V is the volume of the magnetic particle. By fitting $f - f_0$ to Eq. 2.1 with Δf and ΔB as free parameters, we can infer ΔN and the saturation magnetic moment μ_s. An example fit for C1 is shown in Fig. 2.1(a). The fit is excellent; it deviates at low magnetic fields because μ is not yet saturated as we assume in the approximation. Results of the fits are listed in Section D of Table 2.1.

We recover the full magnetization hysteresis curve by rearranging Eqs. 2.1-2.3 as a quadratic equation for magnetization $B_m = \mu_0 \mu / V$ in terms of the magnetic contribution to cantilever spring constant $k_m = 2k_0 (f - f_0)/f_0{}^*$; or equivalently, in units of field, $B_k = k_m \mu_0 l^2 / \alpha^2 V = B_m B(B_m \Delta N)/(B + B_m \Delta N)$. Solving for B_m gives

$$B_m = \frac{B_k}{2B} \pm \frac{1}{2B} \left(B_k^2 + \frac{4B_k B^2}{\Delta N}\right)^{1/2}. \tag{2.4}$$

---

*This relation is a series expansion of $f/f_0 = \sqrt{(k_0 + k_m)/k_0} = \sqrt{1 + k_m/k_0} = 1 + k_m/2k_0 + \ldots$
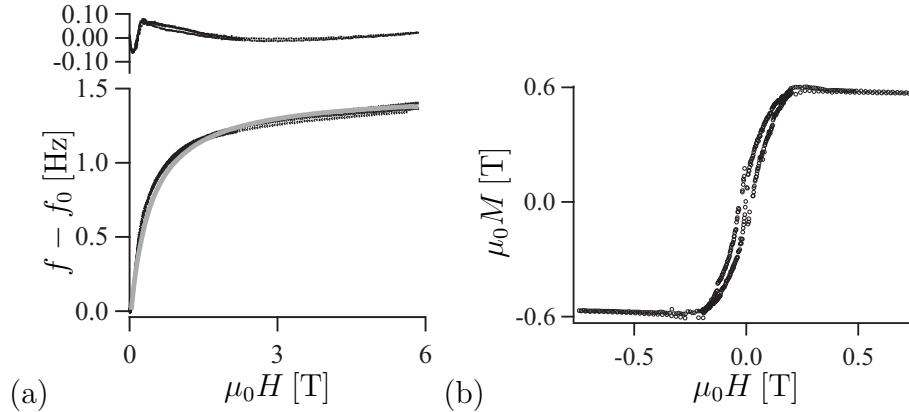
Figure 2.1: Analysis of cantilever C1 magnetization. (a) Fit of cantilever frequency shift to Eq. 2.1. The gray line is the fit to the data in black. The top inset shows the deviations between the fit and the data. (b) Hysteresis curve recovered with Eq. 2.4.

Fig. 2.1(b) shows the magnetization hysteresis curve recovered for C1 using Eq. 2.4. In applying Eq. 2.4, we use ΔN inferred from the saturation analysis, choose the sign in Eq. 2.4 to give a smooth magnetization curve, and discard points within a few mT of $B = 0$. The saturation fields $B_s = \mu_0\mu_s/V = \mu_0 M_s$ are close to the bulk value of 0.6 T for all nickel magnets studied. Given the $10 - 20\%$ uncertainty in cantilever spring constant, there is no discernible difference between the saturation magnetization of the uncapped (C1-C4) and capped (C5) magnets, indicating that oxidation is not a major problem during processing. In retrospect, another metal should probably be used since Cr is known to have interface-enhanced magnetic effects [7]. If we insist that the difference between measured B_s and the literature value is due to a layer of oxide, the maximum possible thickness of oxide is $28\,\mathrm{nm}$.
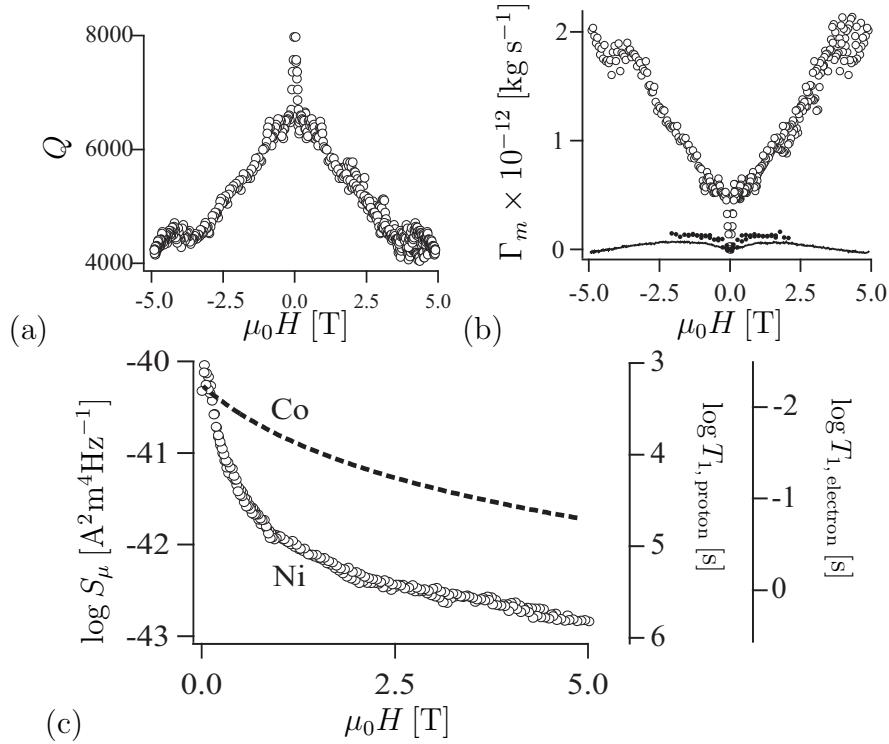
Figure 2.2: Magnetization fluctuation measurements. (a) Quality factor versus applied magnetic field for cantilever C2. (b) Magnetic friction versus applied magnetic field. Upper curve: cantilever C2. Middle curve: cantilever C1. Lower curve: the same bare silicon cantilever as in Fig. 1.1. (c) Spectral density of transverse magnetization versus applied magnetic field for the Ni tip of cantilever C2 (open circles) and the Co tip of nanowire 2 in Ref. [4] (dotted line). The T_1 axes are predictions for the Ni tip.

2.2   Magnetic dissipation

The Q of magnetic cantilevers decreases with increasing magnetic field [Fig. 2.2(a)]. Underlying this behavior is a magnetic-field dependent contribution to cantilever friction. In Fig. 2.2(b) we compute the magnetic friction $\Gamma_m = \Gamma(B) - \Gamma(0)$ from Q, using $\Gamma = 2\pi f m/Q$ where $m = k_0/(2\pi f_0)^2$ is the cantilever effective mass. With the smallest magnet, cantilever C1 is shown to have magnetic friction nearly the same as that of a bare silicon cantilever. The magnetic friction of cantilever C2, which is close in size to the magnetic tips proposed in [8], is much larger than the background. Despite that Q drops by half at 5 T for cantilever C2, the minimum detectable force increases by only 1.4 times; therefore magnetic dissipation is not detrimental to force sensitivity, but the related magnetic fluctuations might hasten sample spin relaxation and will be analyzed in the next section.

2.3   Magnetic fluctuations

By the fluctuation-dissipation theorem [9–12], magnetic friction is associated with a fluctuating force F_t in the direction of the cantilever thickness t, having spectral density $S_F = 4\Gamma_m k_B T$. There are two mechanisms for generating a magnetic-field dependent fluctuating force, both of which involve tip magnetic moment fluctuations: (1) a gradient coupling via $F_t = (\boldsymbol{\mu} \cdot \boldsymbol{\nabla}) B_t$ and (2) a torque coupling via $\boldsymbol{\tau} = \boldsymbol{\mu} \times \boldsymbol{B}$. A torque about the direction of the cantilever width is kinematically equivalent [5] to a force in the direction of the thickness, $F_t = \tau_w \alpha/l$, which gives $F_t = \mu_t B_l \alpha/l$. Because of the comparative homogeneity of the applied static field, $|\boldsymbol{\nabla} B_t| \ll B_l/l$, the torque coupling is the dominant mechanism. We can thus interpret Γ_m as arising from a fluctuation of the magnetic moments in

the direction of the cantilever thickness having spectral density

$$S_\mu(f_0) = \frac{4\Gamma_m k_B T l^2}{\alpha^2 B^2}. \tag{2.5}$$

The notation stresses that we are measuring fluctuations at the cantilever resonance frequency. Fig. 2.2(c) shows the transverse magnetization spectral density $S_\mu(f_0)$ as a function of magnetic field for cantilever C2. Qualitatively, S_μ behaves as expected, decreasing as the tip saturates with increasing field.

In an MRFM experiment, the tip's fluctuating magnetization will appear as a fluctuating magnetic field of spectral density $S_B = S_\mu B_{\rm tip}^2/4\mu^2$, where $B_{\rm tip}$ is the magnetic field from the tip at the location of the sample spin. This fluctuating magnetic field could affect the sample's spin-lattice relaxation rate via $T_1^{-1} = \gamma_s^2 S_B(f_L)$ and the spin-lattice relaxation time in the rotating frame via $T_{1\rho}^{-1} = \gamma_s^2(S_B(f_R)+S_B(f_L))$. Here γ_s is the gyromagnetic ratio, f_L is the Larmor frequency, and f_R is the Rabi frequency of the sample spins; f_L typically ranges between $50-300\,{\rm MHz}$ and f_R between $10-100\,{\rm kHz}$ for protons. Since $f_R \sim f_0$, we can use the measured S_B to directly calculate the tip contribution to the first term in $T_{1\rho}^{-1}$. We can estimate an upper bound for T_1 by taking the measured $S_\mu(f_0)$ as a lower bound for $S_\mu(f_L)$. The right-hand axes in Fig. 2.2(c) show our estimation of tip contribution to T_1 for protons experiencing a tip field of $B_{\rm tip} = 75\,{\rm mT}$ [13]. The long $T_{1,\,\rm proton}$ suggests that the Ni tip is well suited for proton nuclear magnetic resonance experiments at any field.

It is interesting to compare the Ni tip of our cantilever C2 to the Co tip of Ref. [4]. To account for the dependence of S_μ on magnetic moment and frequency, we have scaled up S_μ for the Co tip of Ref [4] by a factor of 5.4. We plot this adjusted S_μ for Co versus $\mu_0 H$ in Fig. 2.2(c). It can be seen that S_μ is higher for Ni at zero field but decreases more rapidly than for Co as the applied field is

increased. By 5 T, S_μ for Ni is actually *lower* than for Co by a factor of eight. This is presumably because Ni has lower anisotropy than Co.

Hannay *et al.* [10] have theoretically examined the spectral density of field fluctuations in Co and PrFeB and concluded that the more anisotropic PrFeB material is the preferable choice for MRFM on electron spins at low external fields. Our measurements indicate that for proton MRFM, the *less* anisotropic material is preferable because its low-frequency thermomagnetic fluctuations, relevant to $T_{1,\,\text{proton}}$, are more easily damped by high applied fields.

2.4   Conclusions

Our modified cantilevers are suitable for use in proton MRFM experiments since they are not oxidized and their magnetic fluctuations will not limit the relaxation rate of sample spins. The optimal magnetic material for MRFM probes depends on the range of applied fields. While high anisotropic alloys are necessary for low-field experiments, nickel is preferable at high magnetic fields. Currently magnetic dissipation is not a significant constraint to force sensitivity, and it can be minimized to the level of bare silicon cantilevers by making the magnet size smaller than $1310 \times 680 \times 200 \,\text{nm}^3$.

2.5   Potential experimental artifacts

Since state-of-the-art lithography equipments might not be readily available, alternative ideas have been proposed for making small magnetic tips. The Lieber group has utilized a commercial AFM to scan over vertical carbon nanotubes in order to pick up a nanotube with an AFM tip [14]. Ferromagnetic metal could be evaporated onto the nanotube to make a magnetic probe [15]. Another idea is to
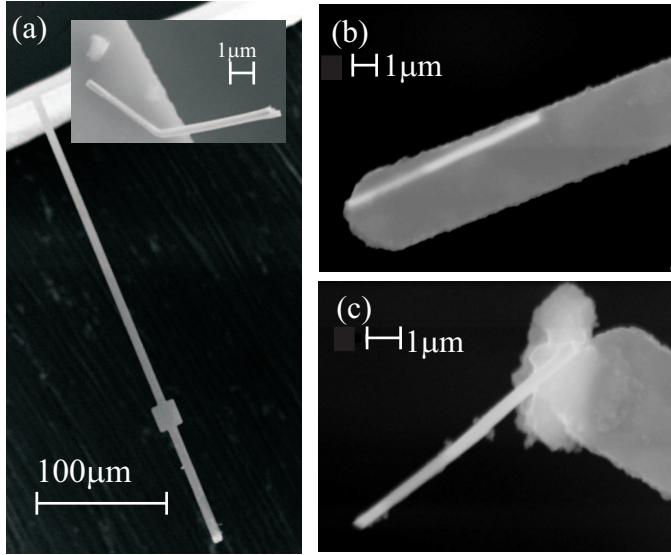
Figure 2.3: SEM of cantilevers with gold-nickel magnetic wires. Part (a) is a view of the entire cantilever with the inset zoomed in on the wire. Part (b) and (c) shows wires that are oriented parallel or perpendicular to the cantilever length, respectively.

use the gold-thiol affinity and/or electric field [16, 17] to place a magnetic wire at the cantilever tip.

Before attempting the gold-thiol assembly method, it would be desirable to first measure the properties of a magnetic wire. Gold-nickel wires, kindly given to us by the Mallouk group from Penn State University, were made by electrochemical deposition into commercially available alumina filter templates [18–21]. Nickel was sandwiched between two gold segments, and titanium was used as an adhesion layer between gold and nickel. The nickel section was 2310 nm long and 330 nm in diameter; the total wire length was 10 μm. The magnetic wires were released by dissolving the alumina template in 0.5M KOH and collected by placing a small magnet on the side of the flask. After the wires were rinsed in deionized water, they could be re-dispersed by brief sonication. A drop of the suspension was pipetted onto a transparency slide, and a small magnet (~ 0.3 T) was placed beside the slide
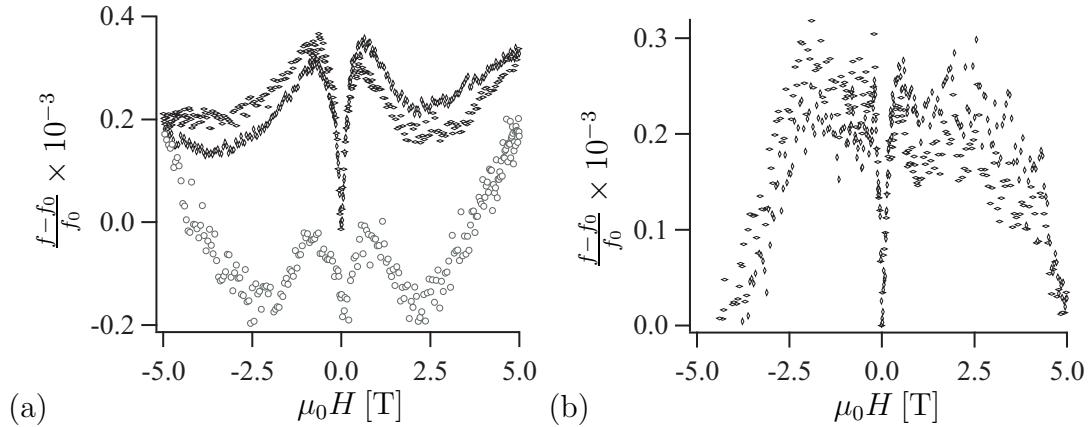
Figure 2.4: (a) Upper curve: frequency shift of the cantilever in Fig. 2.3(a) (350μm × 4μm × 0.34μm, $f_0 = 2557.5$ Hz, $k_0 = 0.20$ mN m^{-1}, and $Q_0 = 300$; nickel magnet length = 2310 nm, diameter= 330 nm). Lower curve: frequency shift of a bare cantilever (125μm × 4μm × 0.34μm, $f_0 = 5939.8$ Hz, $k_0 = 0.95$ mN m^{-1}, and $Q_0 = 3000$). The frequency shift of the bare cantilever has been scaled up to account for the length and spring constant differences between the cantilevers. (b) Frequency shift of the magnetic cantilever after subtracting the lower curve from the upper curve in part (a).

to align the magnetic wires with an external field before the solvent evaporated [22]. Holding the cantilever die like a paintbrush handle, the bare silicon tip was lightly dabbed into optical glue (Loctite 349) and then brushed up a single wire under a stereo optical microscope. Since the magnetic wires have been aligned with an external field, they could be glued approximately perpendicular or parallel to the length of the cantilevers (Fig. 2.3). We found it hard to overcome the Van der Waals attraction between a magnetic wire and a glass slide; however, after switching to plastic transparency slides, the silicon cantilevers were able to pick up the wires. The magnetic tips were intended to be used for MRFM in a vertical geometry similar to Refs. [1, 8, 23].
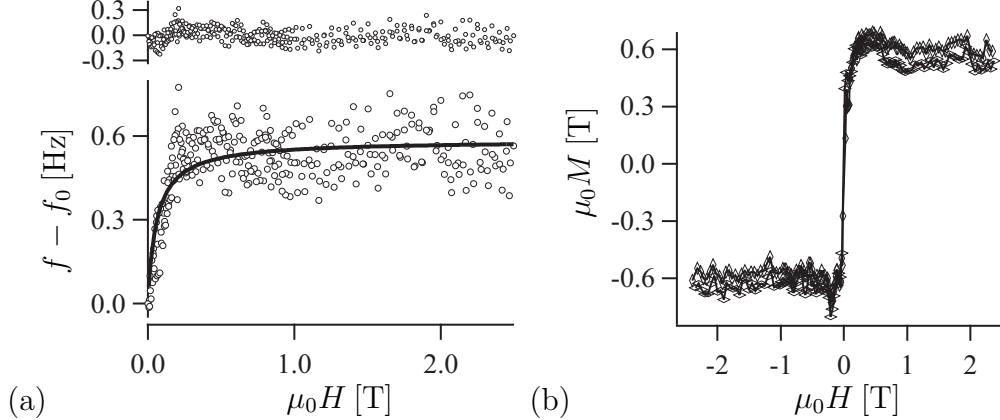
Figure 2.5: Analysis of the nickel wire's magnetization. (a) Fit of frequency shift to Eq. 2.1. The top inset shows the fit residual. (b) Hysteresis curve recovered with Eq. 2.4.

Figure 2.4(a) compares the frequency shift of a glued-on magnetic wire and that of a "bare" silicon cantilever with optical glue only. The bare cantilever does not show hysteresis. After background subtraction, the frequency shift due to the magnetic wire approaches zero at high fields, possibly because diamagnetic contribution from the gold segments have increased to counteract the constant frequency shift from ferromagnetic nickel [Fig. 2.4(b)]. Following the procedure in Section 2.1, the fit parameters are found to be $\Delta f = 9.68$ HzT^{-1}, $\Delta B = 0.06$ T, $\mu_s = 96.3$ fAm^2, $\Delta N = 0.100$, and $B_s = 0.64$ T. The value $\Delta N = 0.100$ corresponds to the magnetic wire tilting off the cantilever length axis by $40°$ [24, 25] and agrees with the SEM image in Fig. 2.3(a). The above measurement shows poor sensitivity, probably because the optical glue has drastically lowered the cantilever Q. Such low Q actually makes us aware of circuit drifts, which can be compensated for as described in the following sections.
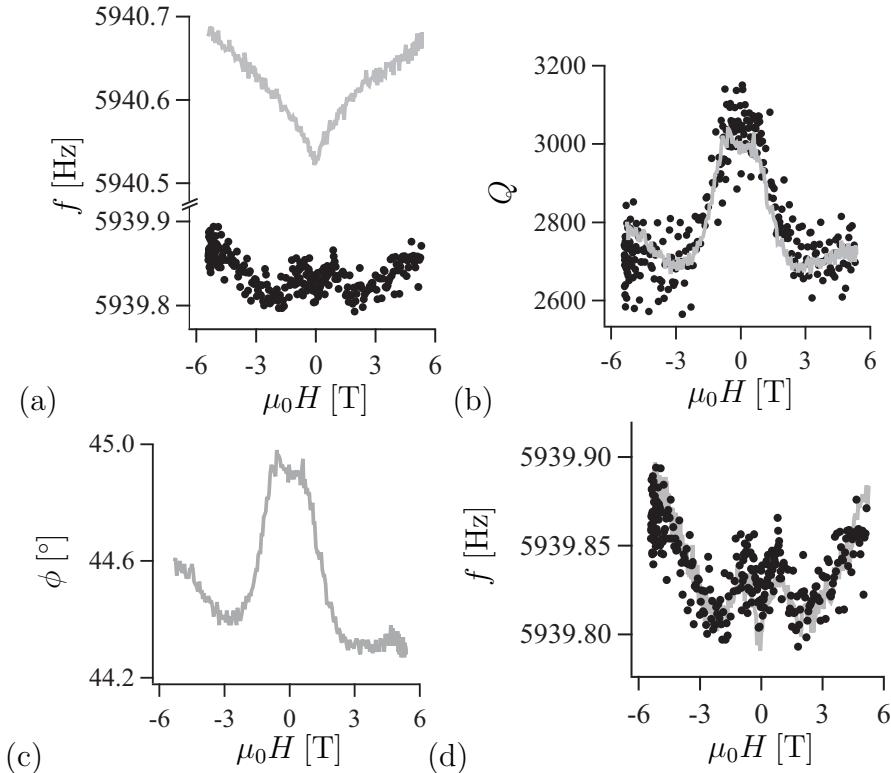
Figure 2.6: Artifact due to phase shift and low quality factor for the bare Si cantilever in Fig. 2.4. The gray curve is measured with positive feedback, and the dotted curve is obtained by ringdown transients. (a) Cantilever resonance frequency vs applied magnetic field before correction. (b) Quality factor vs applied magnetic field. (c) Phase angle between the driving force and the cantilever response vs applied magnetic field. (d) Cantilever resonance frequency vs applied magnetic field after correction.

2.5.1 Frequency adjustment at low Q

Compared to ringdown transients, measuring cantilever frequency by positive feedback loop amplifies signal without restricting bandwidth [26, 27]. However, systematic error may be introduced into the measurement if the phase of the feedback driving is not taken into account [28]. In Fig. 2.6(a), the frequency response obtained by positive feedback appears very different from the ringdown transients, while Q measured by feedback and by ringdown agree with each other [Fig. 2.6(b)]. The different frequency responses can be reconciliated by examining the feedback phase in Fig. 2.6(c). According to Ref. [27], the change in phase $\delta\phi$ induces a change in frequency by $\delta f = f\delta\phi/2Q$; note that δf is larger at lower Q, such as in the case of our cantilever with glue and in ambient environment. Since the phase and Q are known, δf was computed and subtracted from the frequency detected by positive feedback. Fig. 2.6(d) demonstrates that the feedback frequency matches well with ringdown measurements after adjusting for phase shift.

2.5.2 Amplitude adjustment due to detector drift

With the positive feedback loop, cantilever amplitude is obtained simultaneously along with resonance frequency; the fiber-optic interferometer detects amplitude changes at fixed driving voltage. Fig. 2.7(a) shows that, as the applied field is swept, the amplitudes at first harmonic $1f$ for forward and reverse scans do not overlap. The incongruity is likely caused by drift in interferometer signal. To test this hypothesis, the amplitude at second harmonic $2f$ is monitored, because the $2f$ signal will increase if the detector circuit drifts away from the setpoint of maximum detector sensitivity [Fig. 2.7(b)]. Figure 2.7(c) with an increasing $2f$ signal indicates that the interferometer has drifted indeed. The normalized drift corresponds to $\cos(4\pi\beta V_{2f}/\lambda)$, where $\beta = 711.5\,\text{nm/V}$ is the calibration factor [29]

from Fig. 2.7(b), V_{2f} is the amplitude at $2f$, and $\lambda = 1310$ nm is the wavelength of the interferometer. After compensating for detector drift, the $1f$ amplitude in Fig. 2.7(d) overlaps as expected.
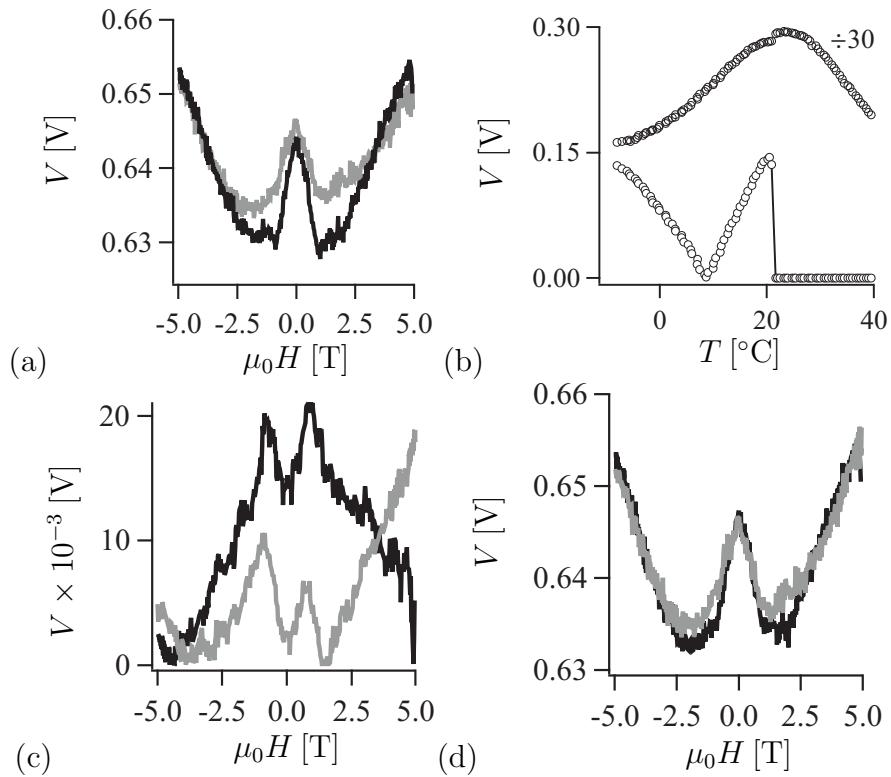
Figure 2.7: Adjustment for interferometer drift. Magnetic field is swept from +5T to -5T (black line) and then back (gray line). (a) $1f$ amplitude vs applied magnetic field, not adjusted for detector drift. (b) Calibration of interferometer signal vs temperature. The lower curve is measured at $2f$, and the upper curve is measured at dc and reduced by 30x. Above 20°C, the $2f$ signal disappeared due to unlocking of the positive feedback loop. (c) $2f$ amplitude vs applied magnetic field. (d) $1f$ amplitude vs applied magnetic field adjusted for detector drift.

CHAPTER 2 REFERENCES

[1] T. D. Stowe et al., Appl. Phys. Lett. **71**, 288 (1997).

[2] N. E. Jenkins et al., J. Vac. Sci. Tech. B **22**, 909 (2004).

[3] J. A. Marohn, R. Fainchtein, and D. D. Smith, Appl. Phys. Lett. **73**, 3778 (1998).

[4] B. C. Stipe, H. J. Mamin, T. D. Stowe, T. W. Kenny, and D. Rugar, Phys. Rev. Lett. **86**, 2874 (2001).

[5] J. A. Sidles et al., Rev. Mod. Phys. **67**, 249 (1995).

[6] A. Aharoni, J. Appl. Phys. **83**, 3432 (1998).

[7] P. Bodeker, A. Schreyer, and H. Zabel, Phys. Rev. B **59**, 9408 (1999).

[8] S. R. Garner, S. Kuehn, J. M. Dawlaty, N. E. Jenkins, and J. A. Marohn, Appl. Phys. Lett. **84**, 5091 (2004).

[9] D. A. McQuarrie, *Statistical Mechanics*, chapter 20, University Science Books, 2000.

[10] J. D. Hannay, R. W. Chantrell, and D. Rugar, J. Appl. Phys. **87**, 6827 (2000).

[11] N. Smith, J. Appl. Phys. **90**, 5768 (2001).

[12] O. Chubykalo et al., J. Magn. Magn. Mater. **266**, 28 (2003).

[13] B. C. Stipe et al., Phys. Rev. Lett. **87**, 277602 (2001).

[14] J. H. Hafner, C. Cheung, T. H. Oosterkamp, and C. M. Lieber, J. Phys. Chem. B **105**, 743 (2001).

[15] N. R. Wilson and J. V. Macpherson, Nano Lett. **3**, 1365 (2003).

[16] P. A. Smith et al., Appl. Phys. Lett. **77**, 1399 (2000).

[17] K. D. Hermanson, S. O. Lumsdon, J. P. Williams, E. W. Kaler, and O. D. Velev, Science **294**, 1082 (2001).

[18] C. R. Martin, Science **266**, 1961 (1994).

[19] J. C. Hulteen and C. R. Martin, J. Mater. Chem. **7**, 1075 (1997).

[20] B. R. Martin et al., Adv. Mater. **11**, 1021 (1999).

[21] M. Tian, J. Wang, J. Kurtz, T. E. Mallouk, and M. H. W. Chan, Nano Lett. **3**, 919 (2003).

[22] M. Tanase et al., Nano Lett. **1**, 155 (2001).

[23] A. DiCarlo, M. R. Scheinfein, and R. V. Chamberlin, Appl. Phys. Lett. **61**, 2108 (1992).

[24] D.-X. Chen and J. A. Brug, IEEE Trans. Magn. **27**, 3601 (1991).

[25] D.-X. Chen, J. Appl. Phys. **89**, 3413 (2001).

[26] T. R. Albrecht, P. Grutter, D. Horne, and D. Rugar, J. Appl. Phys. **69**, 668 (1991).

[27] U. Durig, O. Zuger, and A. Stalder, J. Appl. Phys. **72**, 1778 (1992).

[28] Y. Liu and P. Grutter, J. Appl. Phys. **83**, 7333 (1998).

[29] K. J. Bruland et al., Rev. Sci. Instrum. **70**, 3542 (1999).

Chapter 3

Introduction to electric force microscopy of organic semiconductors

The second part of this thesis focuses on the investigation of organic semiconductors by electric force microscopy (EFM). While new generations of organic electronics are being developed, progress is made largely by trial and error because a fundamental microscopic understanding of charge injection, charge transport, and materials degradation in many widely-used organic semiconductors is still lacking [1, 2]. Knowledge from the inorganic semiconductor community has been borrowed to describe organic electronics, but the inorganic models cannot fully explain many basic properties of organic semiconductors, such as the field-dependent mobility [3–6] and the reduced injection barrier compared to what would be predicted using Schottky theory, as shown in Ref. [7] for aluminum tris(8-hydroxyquinoline) and here for a triarylamine. To design better organic electronic materials and devices, it will be necessary to obtain theories and models tailored for organic semiconductors. This chapter will introduce the electronic properties of organic electronic materials and explain measurements of organic semiconductors by EFM, which provides microscopic insights not readily obtained from other techniques [8–15]. One of the significant differences between organic and inorganic semiconductors is the higher level of disorder in organic materials, and we show here that EFM can elucidate the disorder effects on charge injection and transport.

3.1 π-conjugated organic materials for electronics

Conducting polymers combine the electrical and optical properties of inorganic semiconductors and the mechanical flexibility and processing advantages of polymers [16]. Although the electronic performance of organic semiconductors probably will not overtake their inorganic counterparts, they offer low-cost, lightweight, flexible alternatives that are easy to process in ambient conditions and over large areas [17]. Various applications have been demonstrated, such as light-emitting diodes (LED) [18], photovoltaic cells [19], thin-film transistors (TFT) [2, 20], lasers [21], and chemical sensors [22]. Advances in synthesis of organic semiconductors will expand their capacities even further [23].

3.1.1 Classes of organic semiconductors

The delocalization of π-electrons allows charge conduction along the carbon backbone or between adjacent molecules. The π-bonding is present in all classes of organic electronic materials. Because the molecules or the polymer chains in organic electronic materials are held together by weak van der Waals bonds, films of these molecules are more mechanically flexible than inorganic compounds. Figure 3.1 illustrates examples of the three classes of organic electronic materials. Molecularly doped polymers have small π-conjugated dopant molecules acting as charge conductors in a nonconductive host polymer [Fig. 3.1(a)]. The host polymer is known to influence charge conduction by its polarization energy [24]. For example, TPD-PC has lower mobility than TPD-PS due to the higher dipole moment of PC which increases the hopping barrier. Molecularly doped polymers and semiconducting polymers such as polythiophene [Fig. 3.1(b)] are often solution cast or electrochemically deposited as films that have ordered domains separated by amorphous regions. Molecular solids like pentacene [Fig. 3.1(c)] are less soluble
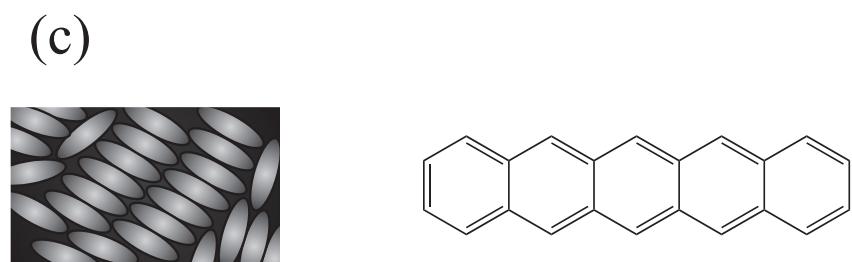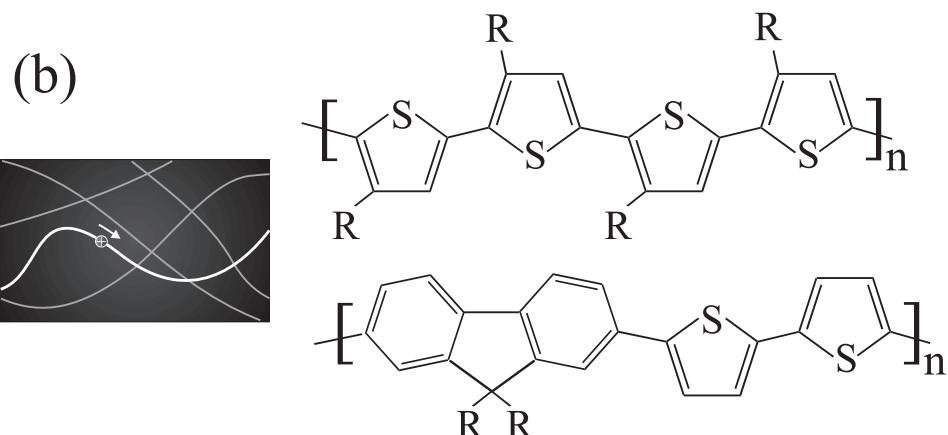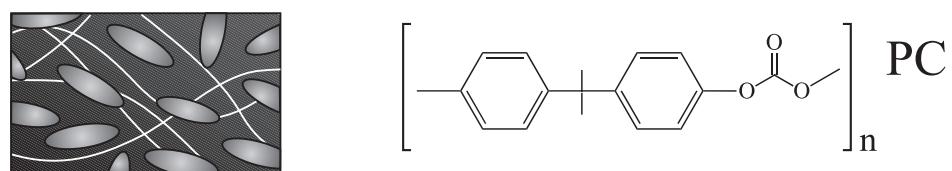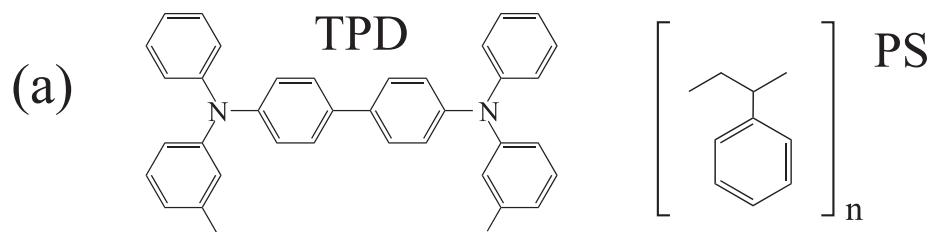
Figure 3.1: Classes of organic semiconductors: their cartoons and respective examples. (a) Molecularly doped polymer: triarylamine (TPD) dopants dispersed in host polymer polystyrene (PS) or polycarbonate (PC). (b) Semiconducting polymers: polythiophene and its derivative. (c) Molecular solids: pentacene.

and are usually deposited by thermal evaporation, which can control grain sizes by varying deposition rates, substrate surfaces, and substrate temperatures.

Despite their diverse structures, organic semiconductors all have localized density of states at room temperature, in contrast to the extended delocalized bands in inorganic semiconductors. The accepted description of charge transport in molecularly doped polymers is the correlated disorder model [4,5,25–29]. The transport of injected holes occurs by hopping between the highest occupied molecular orbital on adjacent molecules. Electrostatic interactions with the permanent dipole and quadruple moments of distant molecules allow for a large number of independent contributions to the energy of an ionized molecule. By the central limit theorem, this leads to an approximately Gaussian density of site energies, with a width σ between 50 and 100 mV in typical molecularly doped polymers [Figure 3.2(a)]. The energy of a state depends on the potential from surrounding dipoles, whose orientations are presumed to be randomly distributed.

Long-range interactions also give rise to spatial correlations in the energy landscape; distant multipoles will influence the energy of a charge on two adjacent dopant molecules in nearly the same manner [Fig. 3.2(b)]. This correlated disorder is the central feature that allows this model to correctly explain the Poole-Frenkel-like dependence of the mobility on electric field seen in molecularly doped polymers. Because their charge-transport properties are so well understood, molecularly doped polymers like TPD-PS now serve as a proving ground for theories of metal/organic charge injection [30–38] The electric force microscope data reported here provides a particularly stringent test of charge injection theories.

Recent experiments have explicitly shown the Gaussian distribution in a semiconducting polymer poly(p-phenylene vinylene) [39] and in a triarylamine α-NPD [40]. It has also been demonstrated that, for high-mobility polymers in the energy
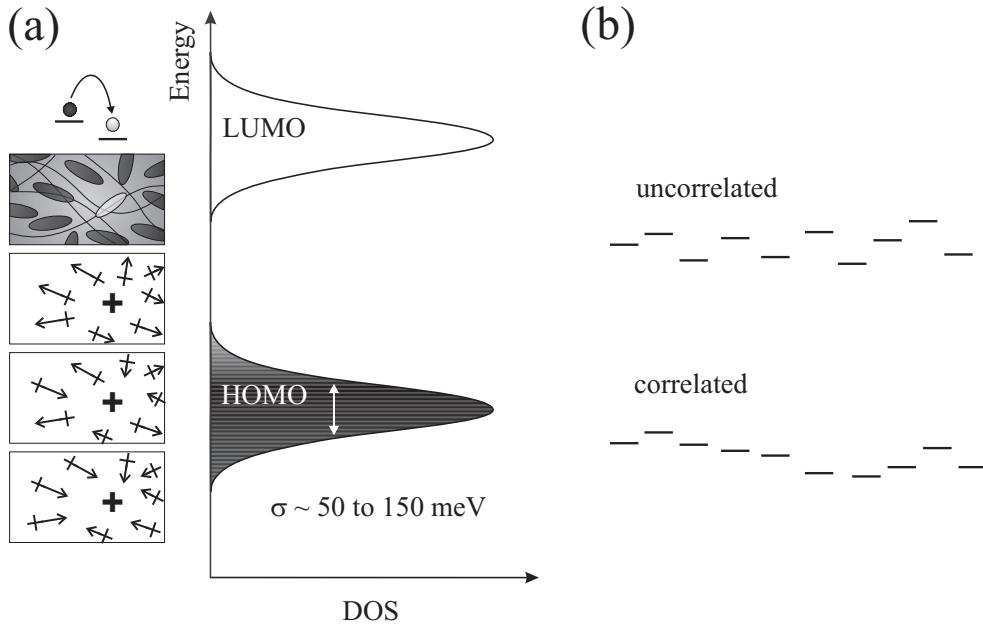
Figure 3.2: (a) Density of states with a Gaussian distribution of width σ due to fluctuations of polarization energies. The boxes on the left demonstrate the electrostatic interactions with neighboring molecules; energy rises when the interaction becomes more repulsive. (b) Uncorrelated and correlated energy levels.

range where the Fermi level is varied, the tail states of the Gaussian distribution can be approximated by an exponential [41].

3.1.2 Charge injection and transport

The process of charge injection is critical to the efficiency of organic semiconductor devices [38]. An ohmic contact provides sufficient charge carriers so the device efficiency is determined by the bulk, not by the contact interface. Roughly speaking, the injection barrier is tuned by minimizing the work function difference between the metal electrodes and the corresponding energy levels of the semiconducting polymer [42]. In addition to the work function difference, the image po-

tential, the applied electric field, and the energetic disorder also affect the injection barrier [37]. Energetic disorder can assist charge injection into organic semiconductors, because it broadens the number of available states for injection [31,35,43–46]. The disorder dependence of charge injection has so far not been thoroughly tested because of the difficulty in separating bulk effects from contact behaviors [37].

Charge transport in molecularly doped polymers occurs by hopping, and the ratio of the average velocity of a hopping charge to the applied electric field is defined as the mobility. Hole mobilities in organic electronics are observed to follow a Poole-Frenkel-like dependence in which $\ln \mu \propto \sqrt{E}$ [47], as explained in the correlated disorder model [4, 5, 29]. When charge density exceeds 10^{22} m^{-3}, as in the case of TFTs or space-charge-limited LEDs, it has been argued that mobility increases with density [48, 49]. A numerical solution accounting for the temperature, disorder, electric-field, and carrier-density dependence of mobility is presented in Ref. [6], though this description starts to break down down at high electric field.

In conducting polymers and van der Waals solids, charge transport is not well understood [2]. For these materials, many phenomenological observations have lead to techniques for improving mobility, but the limiting factor of mobility is still unknown. For example, mobility is observed to increase when a self-assembled monolayer of hydrophobic alkanes is inserted between the dielectric and the organic semiconductor in TFTs [50,51]. More ordered molecular arrangement in the semiconductor, or minimal disorder effect from the dielectric, can be the origin of the increased mobility.

Molecularly doped polymers are free of charge trapping effects in time-of-flight experiments at room temperature. However, charge trapping is a problem in conducting polymers and van der Waals solids. Charge traps impede conduction

and have been imaged [52]. Their locations are not confined to grain boundaries [15], but their molecular identities have not been determined. It is beneficial to obtain a microscopic view to illuminate the limits of charge transport in organic semiconductors.

3.2 Overview of electric force microscopy

Charge injection and transport have been studied by time-of-flight measurements [36,53] and by current-voltage (IV) measurements [7,35,54,55]. For devices with ohmic contacts in which the bulk resistance dominates over contact effects, bulk current-voltage measurements cannot detect the interfacial energetics. Photoemission spectroscopy [56] can determine the interfacial electronic structures but not on actual working devices and not easily on polymer films. Recently, charge injection and transport during device operation have been investigated by scanning probe microscopy [8–14,57], which provides a two-dimensional image of the sample and separates bulk and contact effects readily [Fig. 3.3(a)].

Electric force microscopy (EFM) measures local capacitance and potential, which are directly relevant to device operation. Trapped charges can also be probed, via the resulting shift in the surface potential. Because electrostatic forces are long range, EFM can be used to probe charge trapped below a surface. A potential disadvantage of EFM is that it requires a planar sample and precludes direct study of sandwich structures prevalent in LEDs. Nevertheless, what is learned from planar samples can certainly be used to improve LED operation. EFM's spatial resolution depends on tip shape and distance from the sample. Its typical resolution of 100nm is much worse than for scanning tunneling microscopy but adequate to disentangle bulk and contact resistances in a working TFT. If meaningful EFM data is to be collected, care must be taken with low mobility samples

(a)

(b)

(c) $(f - f_0)/f_0$
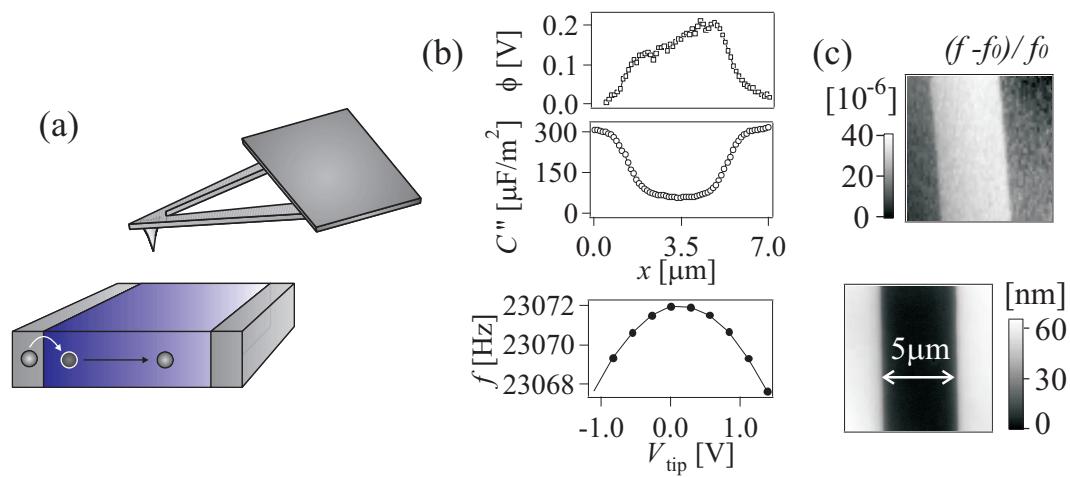
**Figure 3.3:** (a) Electric force microscopy provides a microscopic view, separating charge injection and transport processes. (b) Local potential (top) and capacitance derivative (middle) are inferred from a frequency parabola (bottom) at each location. Here the sample's electrodes are grounded. (c) Force gradient image (top) and topography (bottom) of a TPD-PS film on coplanar Au electrodes.

to prevent triboelectric charging during scanning. Achieving the highest possible sensitivity demands operation in vacuum. Descriptions on the instrumentation of the custom-built variable temperature high-sensitivity microscope can be found in Refs. [58] and [59].

The capacitive tip-sample force gradient leads to a resonance frequency f of

$$f(V_{\text{tip}}, x) = f_0 - \frac{f_0}{4k_0} \frac{\partial^2 C}{\partial z^2} \left[V_{\text{tip}} - \phi(x) \right]^2, \tag{3.1}$$

where f_0 is the intrinsic resonance frequency, k_0 is the intrinsic spring constant, C is the tip-sample capacitance, z is the tip-sample separation, and ϕ is the local potential. Varying V_{tip} within $\pm 2\,\text{V}$ of ϕ, f is quadratic in V_{tip} to within a percent. Fitting f to Eq. 7.3 allows us to infer $\partial^2 C / \partial z^2$ and ϕ at different positions in the sample [Fig. 3.3(b)]. This open loop technique is different from standard Kelvin probe techniques in that it does not require a voltage modulation and does not rely on a feedback circuit to continuously null the potential difference between the tip and surface. Although imaging speed is reduced, quantitative information on the local potential and capacitance derivative are obtained simultaneously in a single scan across the source-drain gap. A force gradient image is obtained by measuring the frequency shift at a fixed tip voltage V_{tip} [Fig. 3.3(c)].

EFM is a non-contact technique; this is important when studying fragile polymer films. It is well suited for variable-temperature experiments, which enable the elucidation of charge conduction mechanisms and rigorous testing of charge injection theories. Finally, EFM is extremely sensitive— single charge sensitivity has been reported in vacuum at room temperature [60–64].

3.3   Topics to be discussed

The following chapters will present:

- **Explanation of degradation mechanisms.** Electric force microscopy (EFM) reveals reversible and irreversible contact degradation mechanisms *in situ.* An initially ohmic contact (metal: Au; molecularly-doped polymer: TPD-PS) becomes injection-limited when temperature is elevated above 310 K; this effect is reversible upon cooling, but permanent damage is observed at 330K, and we hypothesize that it is due to redox reactions. Recrystallization of TPD-PS causes degradation in both the contacts and the film bulk, leading to higher contact resistance and lower mobility. EFM potential profiles suggest that the interface region become more depleted of holes as the contacts become less ohmic with increasing temperature.

- **Evidence for disorder dependence of charge injection.** The field-assisted barrier lowering is more efficient than expected from the Schottky theory, because energetic disorder reduces the injection barrier by broadening the number of available states for charge injection. The temperature-dependent disorder contribution is readily distinguished from the temperature-dependent mobility effects by comparing the current density at the injecting and extracting electrodes. Direct potential and electric-field measurements allow the intrinsic charge density to be inferred, and it does not follow simple Arrhenius behavior but can be explained by incorporating energetic disorder into an expression for the effective activation energy.

- **Charge traps and charge diffusion in TPD-PS.** Molecularly doped polymers are observed to be free of charge trapping effects in time-of-flight experiments at room temperature [53]. Nevertheless, at 250 K and 230 K, the presence of charge traps is detected by EFM in TPD-PS and TPD-PC. Since EFM has higher charge sensitivity than conventional current measurements, at sufficiently low temperatures EFM can resolve deep traps being released.

TPD-PS may appear to be trap-free at the short-time scale probed by time-of-flight studies, but we show that deep traps do exist and their release kinetics and diffusion is observable with EFM.

- **Comparison of trap formation and release kinetics on various dielectrics.** Degradation due to charge trapping is a competing process between the capture and the release of mobile charges. We have investigated the kinetics of trap formation and dissociation in organic field-effect transistors with different processing parameters for the semiconductor/dielectric interfaces, to understand how annealing conditions and dielectric surface treatments change device stability. Trap formation and dissociation is faster for devices with octadecyl-trichlorosilane interfaces than for devices with oxide interfaces. There is no direct correlation between mobility and trap formation. Compared to pentacene, the trap distribution is more spatially homogeneous in F8T2, regardless of the dielectric surface treatments.

CHAPTER 3 REFERENCES

[1] H. E. Katz and Z. Bao, J. Phys. Chem. B **104**, 671 (2000).

[2] H. Sirringhaus, Adv. Mater. **17**, 2411 (2005), and references therein.

[3] H. Bässler, Phys. Status Solidi B **175**, 15 (1993).

[4] D. H. Dunlap, P. E. Parris, and V. M. Kenkre, Phys. Rev. Lett. **77**, 542 (1996).

[5] S. V. Novikov, D. H. Dunlap, V. M. Kenkre, P. E. Parris, and A. V. Vannikov, Phys. Rev. Lett. **81**, 4472 (1998).

[6] W. F. Pasveer et al., Phys. Rev. Lett. **94**, 206601 (2005).

[7] S. Barth et al., Phys. Rev. B **60**, 8791 (1999).

[8] T. Hassenkam, D. R. Greve, and T. Bjornholm, Adv. Mater. **13**, 631 (2001).

[9] X. Cui, M. Freitag, R. Martel, L. Brus, and P. Avouris, Nano Lett. **3**, 783 (2003).

[10] J. A. Nichols, D. J. Gundlach, and T. N. Jackson, Appl. Phys. Lett. **83**, 2366 (2003).

[11] L. Bürgi, T. J. Richards, R. H. Friend, and H. Sirringhaus, J. Appl. Phys. **94**, 6129 (2003).

[12] K. P. Puntambekar, P. V. Pesavento, and C. D. Frisbie, Appl. Phys. Lett. **83**, 5539 (2003).

[13] W. R. Silveira and J. A. Marohn, Phys. Rev. Lett. **93**, 116104 (2004).

[14] O. Tal, W. Gao, C. K. Chan, A. Khan, and Y. Rosenwaks, Appl. Phys. Lett. **85**, 4148 (2004).

[15] E. M. Muller and J. A. Marohn, Adv. Mater. **17**, 1410 (2005).

[16] A. J. Heeger, Rev. Mod. Phys. **73**, 681 (2001).

[17] S. R. Forrest, Nature **428**, 911 (2004).

[18] R. H. Friend et al., Nature **397**, 121 (1999).

[19] P. Peumans, A. Yakimov, and S. R. Forrest, J. Appl. Phys. **93**, 3693 (2003), and references therein.

[20] C. D. Dimitrakopoulos and P. R. L. Malenfant, Adv. Mater. **14**, 99 (2002).

[21] N. Tessler, Adv. Mater. **11**, 363 (1999).

[22] D. T. McQuade, A. E. Pullen, and T. M. Swager, Chem. Rev. **100**, 2537 (2000).

[23] U. Mitschke and P. Bauerle, J. Mater. Chem. **10**, 1471 (2000).

[24] H. J. Yuh and D. M. Pai, Mol. Cryst. Liq. Cryst. **183**, 217 (1990).

[25] S. V. Novikov and A. V. Vannikov, J. Phys. Chem. **99**, 14573 (1995).

[26] Y. N. Gartstein and E. M. Conwell, Chem. Phys. Lett. **245**, 351 (1995).

[27] P. E. Parris, D. H. Dunlap, and V. M. Kenkre, Phys. Status Solidi B-Basic Res. **218**, 47 (2000).

[28] S. V. Novikov and A. V. Vannikov, Mol. Cryst. Liquid Cryst. **361**, 89 (2001).

[29] R. E. Parris, V. M. Kenkre, and D. H. Dunlap, Phys. Rev. Lett. **87**, 126601 (2001).

[30] M. A. Abkowitz and H. A. Mizes, Appl. Phys. Lett. **66**, 1288 (1995).

[31] Y. N. Gartstein and E. M. Conwell, Chem. Phys. Lett. **255**, 93 (1996).

[32] A. Ioannidis, J. S. Facci, and M. A. Abkowitz, J. Appl. Phys. **84**, 1439 (1998).

[33] U. Wolf, V. I. Arkhipov, and H. Bässler, Phys. Rev. B **59**, 7507 (1999).

[34] J. C. Scott and G. G. Malliaras, Chem. Phys. Lett. **299**, 115 (1999).

[35] M. A. Baldo and S. R. Forrest, Phys. Rev. B **64**, 085201 (2001).

[36] Y. Shen, M. W. Klein, D. B. Jacobs, J. C. Scott, and G. G. Malliaras, Phys. Rev. Lett. **86**, 3867 (2001).

[37] J. C. Scott, J. Vac. Sci. Technol. A **21**, 521 (2003).

[38] Y. L. Shen, A. R. Hosseini, M. H. Wong, and G. G. Malliaras, ChemPhysChem **5**, 16 (2004), and references therein.

[39] I. N. Hulea et al., Phys. Rev. Lett. **93**, 166601 (2004).

[40] O. Tal et al., Phys. Rev. Lett. **95**, 256405 (2005).

[41] C. Tanase, E. J. Meijer, P. W. M. Blom, and D. M. de Leeuw, Phys. Rev. Lett. **91**, 216601 (2003).

[42] M. Abkowitz, J. S. Facci, and J. Rehm, J. Appl. Phys. **83**, 2670 (1998).

[43] V. I. Arkhipov, E. V. Emelianova, Y. H. Tak, and H. Bässler, J. Appl. Phys. **84**, 848 (1998).

[44] Y. Preezant and N. Tessler, J. Appl. Phys. **93**, 2059 (2003).

[45] A. L. Burin and M. A. Ratner, J. Polym. Sci.: Pt. B: Polym. Phys. **41**, 2601 (2003).

[46] J. A. Freire and G. Voss, J. Chem. Phys. **122**, 124705 (2005).

[47] P. N. Murgatroyd, J. Phys. D-Appl. Phys. **3**, 151 (1970).

[48] C. Tanase, P. W. M. Blom, and D. M. de Leeuw, Phys. Rev. B **70**, 193202 (2004).

[49] P. W. M. Blom, C. Tanase, D. M. de Leeuw, and R. Coehoorn, Appl. Phys. Lett. **86**, 092105 (2005).

[50] A. Salleo, M. L. Chabinyc, M. S. Yang, and R. A. Street, Appl. Phys. Lett. **81**, 4383 (2002).

[51] J. Veres, S. D. Ogier, S. W. Leeming, D. C. Cupertino, and S. M. Khaffaf, Adv. Funct. Mater. **13**, 199 (2003).

[52] L. Bürgi, T. Richards, M. Chiesa, R. H. Friend, and H. Sirringhaus, Synth. Met. **146**, 297 (2004).

[53] P. M. Borsenberger and D. S. Weiss, *Organic Photoreceptors for Xerography*, Optical Engineering, Marcel Dekker, Inc., New York, 1998.

[54] T. van Woudenbergh, P. W. M. Blom, M. C. J. M. Vissenberg, and J. N. Huiberts, Appl. Phys. Lett. **79**, 1697 (2001).

[55] B. H. Hamadani and D. Natelson, J. Appl. Phys. **97**, 064508 (2005).

[56] H. Ishii, K. Sugiyama, E. Ito, and K. Seki, Adv. Mater. **11**, 605 (1999).

[57] A. B. Chwang and C. D. Frisbie, J. Phys. Chem. B **104**, 12202 (2000).

[58] S. V. Kalinin and A. Gruverman, editors, *Scanning Probe Microscopy: Electrical and Electromechanical Phenomena at the Nanoscale*, volume III, chapter High-sensitivity Electric Force Microscopy of Organic Electronic Devices and Materials, Springer Verlag, New York, 2006.

[59] W. R. Silveira, *Microscopic View of Charge Injection in a Model Organic Semiconductor*, doctoral dissertation, Cornell University, 2005.

[60] C. Schönenberg and S. F. Alvarado, Phys. Rev. Lett. **65**, 3162 (1990).

[61] T. D. Krauss and L. E. Brus, Phys. Rev. Lett. **83**, 4840 (1999).

[62] T. D. Krauss, S. O'Brien, and L. E. Brus, J. Phys. Chem. B **105**, 1725 (2001).

[63] R. Ludeke and E. Cartier, Appl. Phys. Lett. **78**, 3998 (2001).

[64] R. Stomp et al., Phys. Rev. Lett. **94**, 056802 (2005).

Chapter 4

Degradation mechanisms of a molecularly doped polymer

An ohmic contact is critical to the efficiency of organic semiconductor devices [1]. It provides sufficient charge carriers so the device efficiency is determined by the bulk, not by the contact interface. Contact resistance can affect the performance of organic field-effect transistors [2–5] and solar cells [6], and the lifetime of organic light-emitting diodes (OLED) is limited by contact degradation as reviewed by Ref. [7]. Scanning microscopies can disentangle bulk and contact effects and monitor device degradation *in situ* [8, 9]. Electric force microscopy (EFM) has directly measured the contact resistance in an individual device [10–14], in comparison to current-voltage (IV) measurements which extrapolate the average contact resistance from a series of devices with different channel lengths.

In this chapter EFM reveals reversible and irreversible degradation mechanisms in an operating device. An initially ohmic contact becomes injection-limited when temperature is elevated above 310 K. This reversible effect is important as it happens within the normal operating temperatures in practical applications. Irreversible degradation is observed only if polymer recrystallization or chemical reaction has occurred. EFM determines the local work function and therefore can detect chemical changes in the organic semiconductor [15, 16]. EFM allows us to understand degradation mechanisms that would be hard to interpret with IV measurements alone.
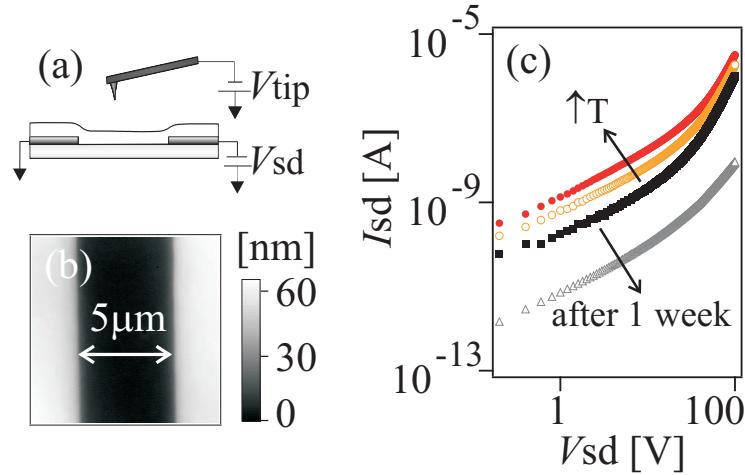
Figure 4.1: (a) Experimental setup. (b) AFM of the device. (c) IV measurements of a TPD-PS film at $296\,\mathrm{K}$ (black squares), $310\,\mathrm{K}$ (orange open circles), $330\,\mathrm{K}$ (red solid circles) taken immediately after spin-casting and after 1 week (gray triangles at $296\,\mathrm{K}$).

4.1 Reversible degradation due to elevated temperatures

Sample preparations and measurements followed the procedure found in Ref. [13]. Both IV and EFM measurements were done in high vacuum (10^{-6} mbar) and in the dark. The organic semiconductor was a triarylamine, N,N'-diphenyl-N-N'-bis(3-methylphenyl)-(1,1'-biphenyl)-4,4'-diamine (TPD), dispersed in a host polymer, polystyrene (PS), and the substrates were coplanar, interdigitated electrodes (50 nm Au with 5 nm Cr as adhesion layer) patterned on quartz [Fig. 4.1(a)]. The spin-casted film was amorphous with thickness of 100 nm [Fig. 4.1(b)].

In Fig. 4.1(c), IV measurements show increasing current with higher temperature and a loss of current after the device has been left in vacuum for one week. Apparently the contacts have degraded with time, but the effect of temperature on contact efficiency is less obvious. While higher temperature leads to higher current, it also shifts the crossover voltage, where current transitions from linear
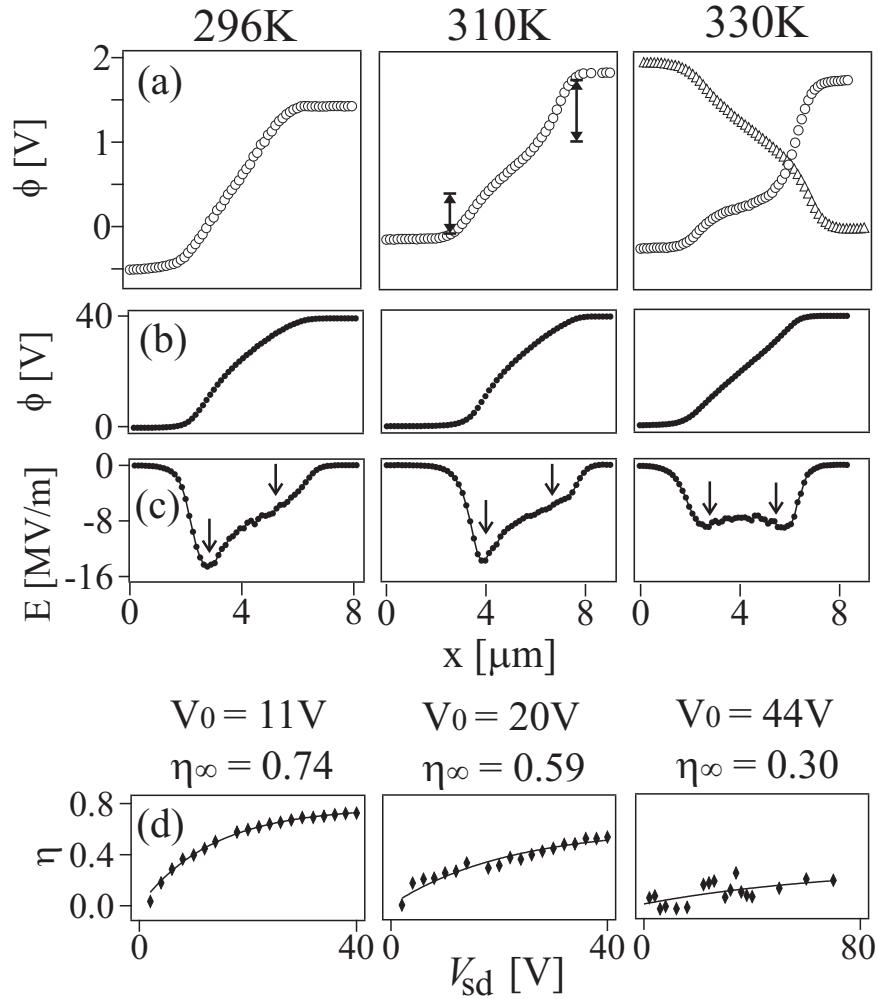
Figure 4.2: Device operation at different temperatures. (a) Potential profiles at $V_{sd} = 2\,$V. At 330K, the potential drop is asymmetric. (b) Potential profiles at $V_{sd} = 40\,$V. (c) Electric fields at $V_{sd} = 40\,$V. (d) Contact ohmicity vs bias voltage taken at the locations indicated by the arrows in (c). See text for explanation of the fit values listed on top of the graphs in row (d).

to quadratic voltage dependence, to a larger value. This indicates that higher bias voltage is required to achieve space-charge limited (SCL) conduction [17, 18]. Explanation for the these observations are elucidated by EFM.

Temperature effects are easily discernable with EFM potential profiles. In EFM, the tip-sample force gradient changes the cantilever resonance frequency f, which allows us to infer the local potential ϕ at each bias voltage V_{sd} and position x. Figure 4.2(a) shows the local potential at a bias voltage ($V_{\mathrm{sd}} = 2\,\mathrm{V}$) in the linear $I \propto V_{\mathrm{sd}}$ regime, while part (b) is taken at $V_{\mathrm{sd}} = 40$ V in the SCL $I \propto V_{\mathrm{sd}}^2$ regime. Device resistance at 296 K is set by the bulk and not by the contacts, because all of the applied voltage is dropped in the bulk of the film. EFM unambiguously confirms SCL conduction at room temperature, because the electric field, obtained by taking the derivative of the potential $-d\phi/dx = E(x)$, is not constant inside the bulk [13] [Fig. 4.2(c)]. Readers should be aware that, in IV measurements, $I \propto V^2$ does not fully confirm SCL conduction, as explained in Ref. [19]. Figure 4.2(d) illustrates the extent of SCL conduction, which is also a measure of the ohmicity of a contact. It is calculated from the electric fields at the interfaces by $\eta = (E_e - E_i)/E_e$, where E_i and E_e are the electric field at the injecting and extracting electrodes, respectively [1, 13, 20]. As defined, $\eta = 0$ for purely ohmic current and $\eta = 1$ when the current is purely space-charge limited. Larger η indicates more efficient contacts.

At $310\,\mathrm{K}$, a potential drop at the interfaces is evident for low V_{sd}. The contacts become more injection-limited with increasing temperature. With high V_{sd} the potential drop disappears, because the contacts are assisted by the barrier-lowering effect of the interfacial electric field. Compared to operation at room temperature, the heated device carries a smaller extent of SCL current at all applied bias. In agreement with IV measurements, higher crossover voltages are needed at elevated

temperatures. Here the crossover voltage V_0 is found from fitting to $\eta = \eta_\infty[1 - \exp(-V_{\text{sd}}/V_0)]$, where η_∞ is the maximum extent to which SCL current dominates transport; the fit values are found above Fig. 4.2(d). When the heated device is cooled back to room temperature, the potential drop disappears at all V_{sd} and the contacts are restored back to the same level of ohmicity as before.

If it seems contradictory that the current is increasing while the contact is worsening, one must remember that contact resistance is not related to mobility in the bulk of a film [1]. At elevated temperatures, the bulk has higher capacity to conduct charges. More current can pass through the device, but the contacts are not able to keep up with the increased demand for charge carriers and become the bottleneck of the device. Prior experiments have shown contact resistance decreases with temperature in injection-limited devices [5, 11], in agreement with our contacts being more ohmic at lower temperature. We emphasize that this temperature effect on contact efficiency is reversible unless some other degradation mechanisms are also involved.

4.2   Irreversible degradation mechanisms

Device operation at 330 K results in irreversible damage to the injecting electrode. When the injecting electrode is switched, the potential drop is still larger at the right electrode, indicating permanent damage there. After the device is turned off, a region of shifted potential (45 ± 5 mV) remains near the right injecting electrode, shown in the force gradient image in Fig. 4.3. Since the damage is asymmetric, it is not due to a glass-transition phase change ($T_g = 336$ K in Ref. [21]), which would affect the whole film and should change both electrodes equally, similar to the case of recrystallization discussed below. Dark spots in OLED have been caused by chemical reaction of the contact metal, indium tin
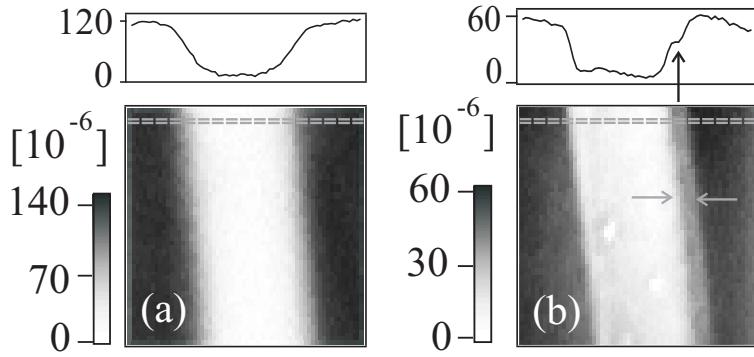
Figure 4.3: Force gradient profiles and images at $296\,\mathrm{K}$ (a) and at $330\,\mathrm{K}$ (b), obtained by recording the frequency shift $(f - f_0)/f_0$, where f_0 is the intrinsic cantilever resonance frequency, at $V_{\mathrm{sd}} = 0\,\mathrm{V}$ and a tip voltage of $1\,\mathrm{V}$. Line profiles are taken at the location indicated by the gray lines. The image scales are not the same due to different distances between tip and polymer surface.

oxide [7]. Since our contact metal is nonreactive gold, rearrangement of interface dipoles or redox reaction of the polymer are more likely causes of the irreversible damage described here. Running current through the device initiates the redox reaction, because no damage is seen when the device is heated to $330\,\mathrm{K}$ but not turned on.

Another device that has been left inside the probe for one week shows drastic decrease in current [Fig. 4.1(c)]. The cause of this degradation is revealed when sample topography is obtained by intermittent-contact atomic force microscopy (AFM). Recrystallization of TPD-PS has occurred because the TPD concentration (50% by weight) is very high. The film roughness is measured to be 10 nm after recrystallization [Fig. 4.4(a)], compared to 0.7 nm before [Fig. 4.1(b)]. The mobilities extracted from IV measurements, adjusted for contact resistance, have decreased from $3.2 \times 10^{-11}\,\mathrm{m^2/Vs}$ to $1.4 \times 10^{-12}\,\mathrm{m^2/Vs}$ upon recrystallization.
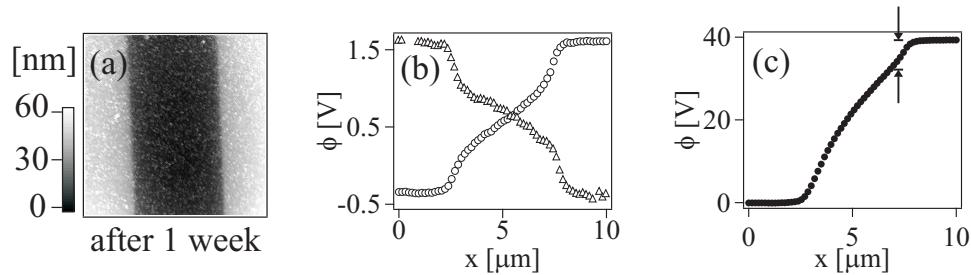
Figure 4.4: (a) AFM image of the same TPD-PS film in Fig. 4.1 after 1 week. (b) Potential profiles at 296 K of the crystallized film with $V_{sd} = 2$ V. The potential drop remains symmetric when the injecting electrode is switched. (c) Potential drop persists at $V_{sd} = 40$ V in the crystallized film.

The concentration of bulk intrinsic charge, $N_0 = 1 \times 10^{21}$ m^{-3}, is not changed by crystallization. *

Although the bulk has become worse with lower mobility, the contacts have degraded even faster as demonstrated by EFM potential profiles. The potential drop at the contacts indicates increased Au/TPD-PS contact resistance [Fig. 4.4(b)]. The potential profiles stay symmetric when the applied bias is reversed, in contrast to the asymmetric potential obtained at 330 K. The potential drop persists despite high V_{sd}, which implies the electric field barrier-lowering effect is not sufficient to overcome the poor contacts [Fig. 4.4(c)]. Recrystallization of TPD could cause poor physical contact and/or decrease the density of states available for injection by reducing the energetic disorder present in the film [22]. Variable temperature EFM measurements should allow us to evaluate these two possibilies.

---

*The procedure for obtaining mobility and intrinsic charge density is found in Refs. [13] and [18].

4.3   Conclusions

EFM shows that operation at elevated temperature and crystallization both lead to higher contact resistance, despite that the bulk mobility is improved by the former and decreased by the later. Recrystallization has worsened both bulk mobility and contact efficiency and can be avoided by choosing high-T_g materials or adjusting dopant concentration. Degradation due to heat happens within the normal operating temperatures in practical applications. Above room temperature, the emerging potential drop suggests that the interface region becomes more depleted of holes, because less space charge is injected and the lack of charge carriers is compensated by a drastic potential change. A potential drop should not be automatically assumed to indicate depletion region, since poor physical contact, possible in the case of recrystallization, can also increase contact resistance; nevertheless, a depletion region is likely for operation at elevated temperature and may be alleviated by a doped interface to improve device performance [23]. The above intrinsic degradation is similar to the luminance loss in AlQ_3 OLED caused by the decrease in charge-transporting species at the interface, as described in the review by Aziz and Popovic [7]. The change in contact ohmicity is reversible, possibly due to the Fermi level of TPD-PS shifting with temperature; this temperature effect is currently being investigated with more quantitative EFM measurements. It would also be interesting to study the mechanisms and kinetics of irreversible degradation due to redox reaction at elevated temperatures.

CHAPTER 4 REFERENCES

[1] Y. L. Shen, A. R. Hosseini, M. H. Wong, and G. G. Malliaras, ChemPhysChem **5**, 16 (2004), and references therein.

[2] G. Horowitz, R. Hajlaoui, D. Fichou, and A. E. Kassmi, J. Appl. Phys. **85**, 3202 (1999).

[3] R. A. Street and A. Salleo, Appl. Phys. Lett. **81**, 2887 (2002).

[4] E. J. Meijer, G. H. Gelinck, E. van Veenendaal, B. H. Huisman, and D. M. de Leeuw, Appl. Phys. Lett. **82**, 4576 (2003).

[5] B. H. Hamadani and D. Natelson, Appl. Phys. Lett. **84**, 443 (2004).

[6] P. Peumans, A. Yakimov, and S. R. Forrest, J. Appl. Phys. **93**, 3693 (2003), and references therein.

[7] H. Aziz and D. Popovic, Chem. Mater. **16**, 4522 (2004), and references therein.

[8] L. S. C. Pingree, M. C. Hersam, M. M. Kern, B. J. Scott, and T. J. Marks, Appl. Phys. Lett. **85**, 344 (2004).

[9] P. Melpignano et al., Appl. Phys. Lett. **86**, 041105 (2005).

[10] J. A. Nichols, D. J. Gundlach, and T. N. Jackson, Appl. Phys. Lett. **83**, 2366 (2003).

[11] L. Bürgi, T. J. Richards, R. H. Friend, and H. Sirringhaus, J. Appl. Phys. **94**, 6129 (2003).

[12] K. P. Puntambekar, P. V. Pesavento, and C. D. Frisbie, Appl. Phys. Lett. **83**, 5539 (2003).

[13] W. R. Silveira and J. A. Marohn, Phys. Rev. Lett. **93**, 116104 (2004).

[14] O. Tal, W. Gao, C. K. Chan, A. Khan, and Y. Rosenwaks, Appl. Phys. Lett. **85**, 4148 (2004).

[15] H. Takano and M. D. Porter, J. Am. Chem. Soc. **123**, 8412 (2001).

[16] X. Cui, M. Freitag, R. Martel, L. Brus, and P. Avouris, Nano Lett. **3**, 783 (2003).

[17] P. N. Murgatroyd, J. Phys. D-Appl. Phys. **3**, 151 (1970).

[18] A. A. Grinberg, S. Luryi, M. R. Pinto, and N. L. Schryer, IEEE Trans. Elec. Dev. **36**, 1162 (1989).

[19] V. I. Arkhipov, P. Heremans, E. V. Emelianova, and G. J. Adriaenssens, Appl. Phys. Lett. **79**, 4154 (2001).

[20] M. Abkowitz, J. S. Facci, and J. Rehm, J. Appl. Phys. **83**, 2670 (1998).

[21] D. M. Pai, J. F. Yannus, and M. Stolka, J. Phys. Chem. **88**, 4714 (1984).

[22] A. R. Hosseini, M. H. Wong, Y. Shen, and G. G. Malliaras, J. Appl. Phys. **97**, 023705 (2005).

[23] P. K. H. Ho et al., Nature **404**, 481 (2000).

Chapter 5

Effect of temperature and energetic

disorder on charge injection

A better understanding of charge injection into organic semiconductors is essential for improving the design and operation of organic electronic devices [1, 2]. The density of states in organic semiconductors is described by a Gaussian distribution of energies [3, 4]. Site-to-site variations in energy levels are thought to assist charge injection into organic semiconductors [5–10]. Engineering the metal-organic interfaces by dopants has led to more efficient contacts [11]. The effect of energetic disorder is very well studied for charge transport [12–14]; but the disorder dependence of charge injection is not thoroughly tested due to the difficulty of separating bulk effects from contact behaviors [1], when both the mobility and the barrier-lowering effect has the same electric-field dependence.

Charge injection has been studied mainly by time-of-flight charge measurements [15, 16] and by current-voltage (IV) measurements [7, 17–19] in injection-limited devices. For devices with ohmic contacts in which the bulk resistance dominates over contact effects, bulk measurements cannot detect the interfacial energetics. Photoemission spectroscopy [20] can determine the interfacial electronic structures, but so far not on actual working devices. In comparison, scanned probe microscopy [21–29] can disentangle bulk and contact effects and determine the local electrostatic potential during operation.

In this chapter we use electric force microscopy (EFM) to study charge injection as a function of temperatures. The results are interpreted in terms of energetic disorder. The electric-field dependence of mobility and charge injection can be distinguished from each other because the local electric field is directly measured.

Analysis of EFM measurements does not assume an average electric field as done with injection-limited devices. It allows us to test injection theories on an "ideal" bulk-limited device with ohmic contacts. For clarification of terminology, an *ohmic contact* is a "good" contact and supports space-charge-limited current, while *ohmic current* is due to injection-limited "bad" contacts.

5.1 Effect of temperature on charge injection

Both IV and EFM measurements were done in high vacuum (10^{-6} mbar) and in the dark. The organic semiconductor was a triarylamine, N,N'-diphenyl-N-N'-bis(3-methylphenyl)-(1,1'-biphenyl)-4,4'-diamine (TPD), dispersed in a host polymer, polystyrene (PS), and the substrates were coplanar, interdigitated electrodes (50 nm Au with 5 nm Cr as adhesion layer) patterned on quartz [Fig. 5.1(a)]. The spin-casted film was amorphous with thickness of 100 nm [Fig. 5.1(b)]. In Fig. 5.1(c), IV measurements show increasing current and crossover voltage, where current transitions from linear to quadratic voltage dependence, with higher temperature.

Figure 5.2(a) displays the local potential $\phi(x)$ inferred from EFM with an applied source-drain bias $V_{\mathrm{sd}} = 2\,\mathrm{V}$. The corresponding electric field, obtained by taking the derivative of the potential $-d\phi/dx = E(x)$, is constant throughout the device [Fig. 5.2(b)]. With $V_{\mathrm{sd}} = 40\,\mathrm{V}$, the potential profiles become non-linear [Fig. 5.2(c)]. Potentiometry illustrates the transition from ohmic to space-charge limited (SCL) [27, 30, 31] conduction as the source-drain bias is increased. (The bump near the injecting electrode at $250\,\mathrm{K}$ could be due to space charges, but it is observable only with a sharp brand-new cantilever.) The electric field emphasizes the SCL mechanism in which the electric field at the injecting electrode approaches zero due to injected space charges [Fig. 5.2(d)]. We hypothesize that the electric
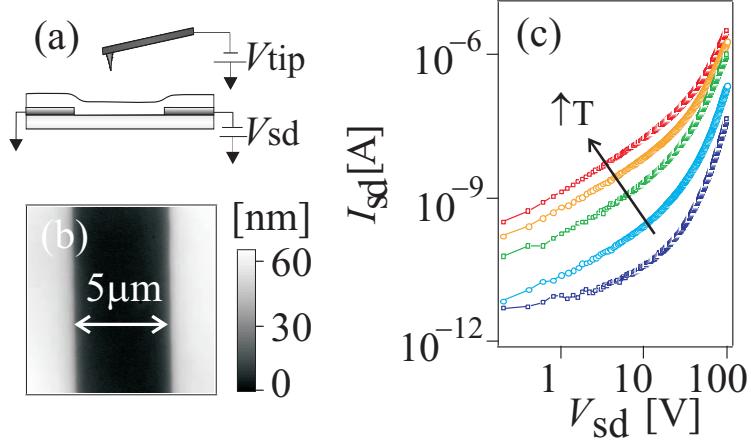
Figure 5.1: (a) Experimental setup. (b) AFM of the device. (c) IV measurements of a TPD-PS film at 250 K, 273 K, 296 K, 310 K, and 330 K.

field does not follow the exact form of the one-dimensional Child's law [32] due to trapped charges, evidence of which is included in Chapter 6, and possibly due to geometric effects. The ability to directly determine electric field is crucial to the following study, and it also helps to elucidate other processes, such as the position-dependent recombination probability in organic light-emitting diode [33].

The potentials and electric fields in Fig. 5.2 illustrate the effect of temperature on contact efficiency. That all of the applied voltage is dropped in the bulk of the film suggests that device resistance at 296 K and below is set by the bulk and not by the contacts. However, as temperature is elevated, a drop in potential emerges at the metal-organic interface [Fig. 5.3(a)]. The contact resistance can be estimated from a voltage drop by $R = W \Delta V / I_{sd}$, where W is the channel width [25]. Although EFM measures the local potential and not the local voltage, we assume the difference between the two is negligible. While this assumption deserves further attention, the local potential drop is used to extract the contact resistance at 330 K. Figure 5.3(b) shows that contact resistance levels off with increasing applied bias. The potential drop actually disappears, or becomes indistinguishable,
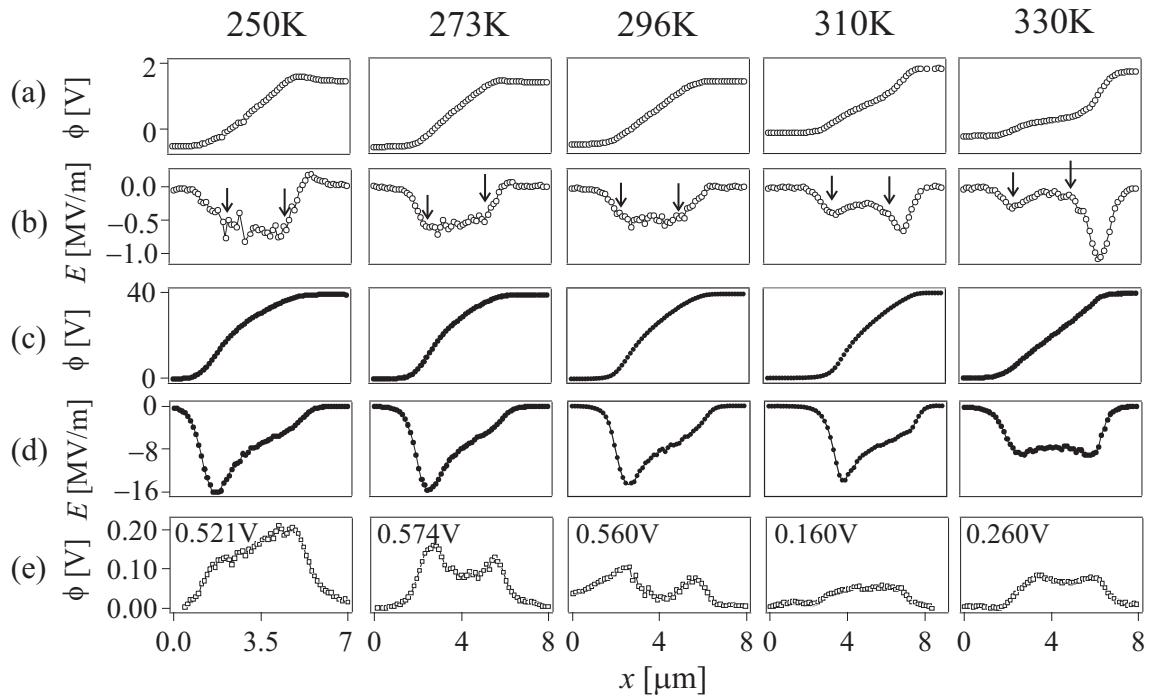
Figure 5.2: Device operation at different temperatures and applied bias. Potential profiles (a,c,e) and electric fields (b,d) with $V_{sd} = 2$ V for open circles (a,b), $V_{sd} = 40$ V for solid circles (c,d), and $V_{sd} = 0$ V for open squares (e). In (e), the potentials have been shifted up by the number indicated at the left upper corner. The arrows in (b) indicate the positions at which E is compared at different temperatures.
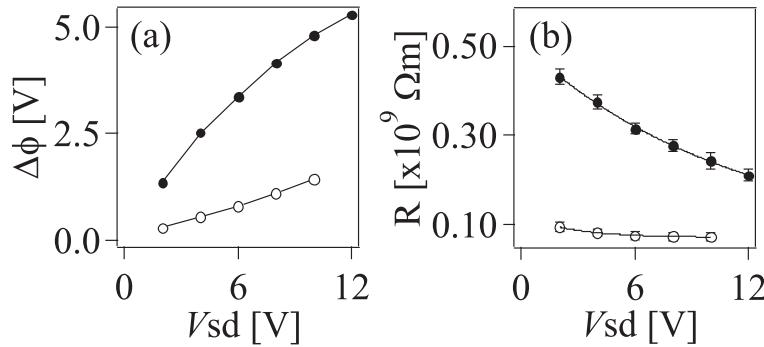
Figure 5.3: Potential drop (a) and contact resistance (b) at the injection electrode (solid circles) and at the extracting electrode (open circles) at $330\,\mathrm{K}$ as a function of applied bias.

by $V_{\mathrm{sd}} = 14\,\mathrm{V}$, because the contacts are assisted by the barrier-lowering effect of the interfacial electric field.

With increasing temperature the contacts become less ohmic and support a smaller extent of SCL current. Figure 5.4(a) shows the evolution of electric field with temperature. At a fixed bias the extent of SCL conduction decreases with higher temperature; figure 5.4(b) quantifies the extent of SCL conduction. It is calculated from the electric fields at the interfaces by $\eta = (E_e - E_i)/E_e$, where E_i and E_e are the electric field at the injecting and extracting electrodes, respectively [2,27,34]. The electric fields across the temperature range are chosen at the same locations in the device, indicated by the arrows in Fig. 5.2(b); the locations are immediately outside of the regions with drastic potential drops. As defined, $\eta = 0$ for purely ohmic current and $\eta = 1$ when the current is purely space-charge limited. That the device here is never fully space-charge-limited may be due to intrinsic background carriers.

In agreement with IV measurements, higher crossover voltages are needed at elevated temperatures [Fig. 5.1(c)]. The crossover voltage V_0 is found from fitting to $\eta = \eta_\infty[1 - \exp(-V_{\mathrm{sd}}/V_0)]$, where η_∞ is the maximum extent to which SCL
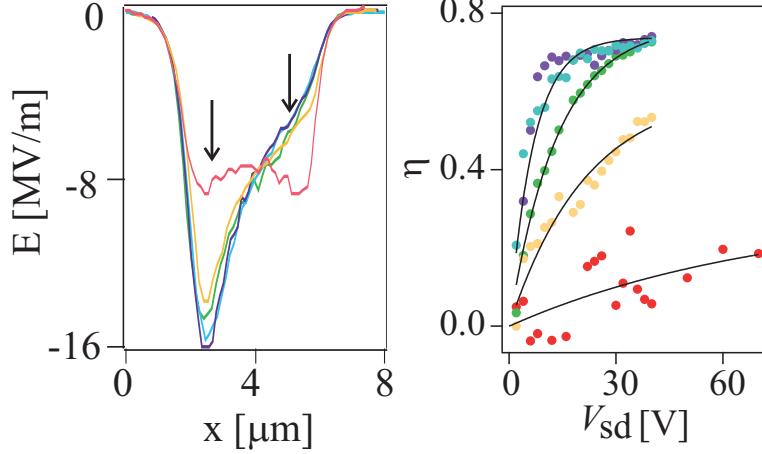
Figure 5.4: (a) Local electric field with $V_{sd} = 40$V as temperature is increased from 250 K (purple), 273 K (blue), 296 K (green), 310 K (orange), and 330 K (red). (c) Extent of SCL conduction vs bias voltage taken at the locations indicated by the arrows in (a).

current dominates transport. The fit values are listed in Table 5.1 and indicate that the device eventually achieves the same level of SCL conduction for temperatures where no potential drop is observed at $V_{sd} = 2$ V. However, η_∞ is lower for 310 K and 330 K, despite the same $I \propto V^2$ dependence found in IV curves. If we extract mobilities from IV measurements by SCL equations [30, 31] without adjusting for the change in η with temperature, the mobility values will be overestimated at high temperatures because the SCL equations assume constant $\eta = 1$.

The potential offset $\Delta\phi_0$ between the metal and the semiconductor with $V_{sd} = 0$ V [Fig. 5.2(e)] is due to the energy difference ψ between the Fermi level of the semiconductor and the metal work function, plus an interface dipole Δ [20] [Fig. 5.5(a)]. Below 296 K the shape of the potential profiles may be influenced by trapped charges in the channel as we will show in Chapter 6. However, the potential difference at the interfaces should not be affected because trapped charges are quickly removed when they are close to the electrode metal. Figure 5.5(b)

Table 5.1: Best-fit values for η vs V_{sd}.

| T [K]	η_∞	V_0 [V]
250, 273	0.74	6.8
296	0.74	11
310	0.59	20
330	0.30	44
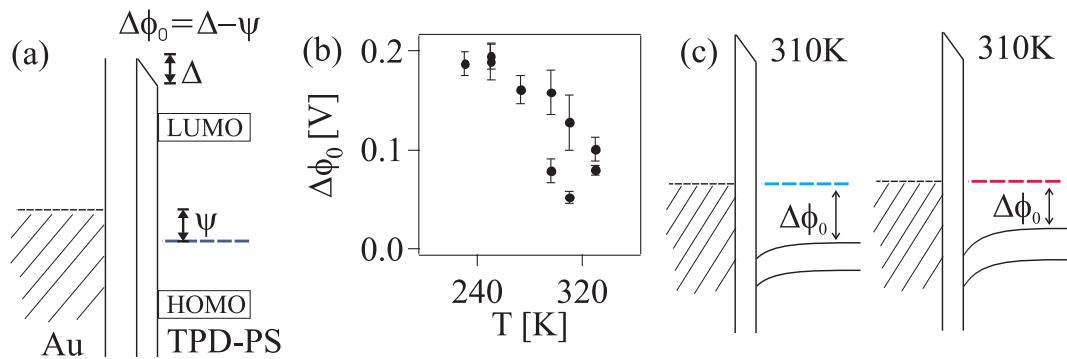
Figure 5.5: (a) Potential offset between the metal and the semiconductor with $V_{\text{sd}} = 0$ V due to the energy difference between the Fermi level of the semiconductor and the metal work function and the interface dipole. (b) Potential offset with $V_{\text{sd}} = 0$ V as a function of temperature. (c) Less hole depletion with lower temperature.

shows that $\Delta\phi_0$ slightly decreases with increasing temperature, indicating holes are more depleted as temperature rises. This trend is in agreement with the above observation that fewer space charges are injected at higher temperatures. Large potential drops, seen in Fig. 5.2(a), are required to compensate for the lack of charge carriers at the Au/TPD-PS interface at 310 K and 330 K, suggesting that the interface region is depleted of holes at these temperatures [Fig. 5.5(c)].

5.2   Injection barrier lowering from energetic disorder

The following analysis elucidates the field and temperature dependence of the injection current. The current density is plotted against local electric field at different temperatures in Fig. 5.6, in which the current and electric field at the extracting electrode are assigned negative values. Although current is constant throughout the device, the contributing parameters are different depending on the location. We model the current density at the injecting and extracting electrodes as, respectively,

$$J_{\text{inj}} \quad = \quad \frac{\mu_0}{\beta_\mu\sqrt{E}K_1(\beta_\mu\sqrt{E})}\frac{\rho_0}{\beta_b\sqrt{E}K_1(\beta_b\sqrt{E})}wE, \text{ and} \tag{5.1}$$

$$J_{\text{ext}} \quad = \quad \frac{\mu_0}{\beta_\mu\sqrt{E}K_1(\beta_\mu\sqrt{E})}[\rho_0wE + \varepsilon'E^2], \tag{5.2}$$

where μ_0 is the mobility, β_μ accounts for the field dependence of the mobility along with a modified Bessel function of the second kind K_1 [12,13], w is the total width of the electrodes, ρ_0 is the injected charge density, and β_b describes the field dependence of injection barrier lowering by image charges and energetic disorder. The parameters μ_0, β_μ, ρ_0, and β_b are all temperature and disorder dependent. The second term in J_{ext} is a first-order approximation for space charges with ε' accounting for the geometric factor and the dielectric constant. Our sensitivity is not sufficient to quantify β_μ, because it is very difficult to distinguish the functional
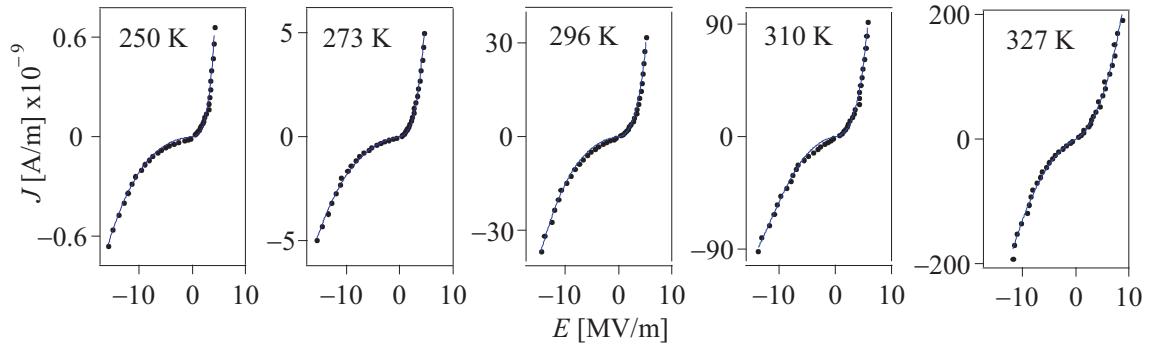
Figure 5.6: Current density vs local electric field as temperature is varied.

form of E^2 from the Bessel function in Eq. 5.2. Overall, it is very complicated to fit and distinguish so many variables in Eq. 5.1 and 5.2, especially since the mobility and injected charge density have identical $\sqrt{E}$ dependence and both are thermally activated process. Fortunately an alternative method is applicable and will be described below.

At the injecting electrode the rise of current with electric field depends on $\beta_b + \beta_\mu$, but at the extracting electrode the field dependence relies on β_μ only. Because β_b applies only at the injecting electrode, its temperature dependence can be separated from β_μ by scaling. In Fig. 5.7, the current densities at the extracting electrode have been scaled to the same magnitude for all temperatures. The scaling factors (listed inside the figure as $C(T)$) compensate for the difference in mobility across the temperature range and equalize the mobility dependence on temperature and electric field. Since the electric-field measurement noise dominates over the current noise, the error bars in the inset of Fig. 5.7 are calculated from $(dJ/dE)dE$. After scaling, the temperature dependence of β_b is very apparent [Fig. 5.8(a)]. As temperature lowers, field-assisted injection is more prominent, which explains the increasing extent of SCL conduction when temperature is decreased. The top inset
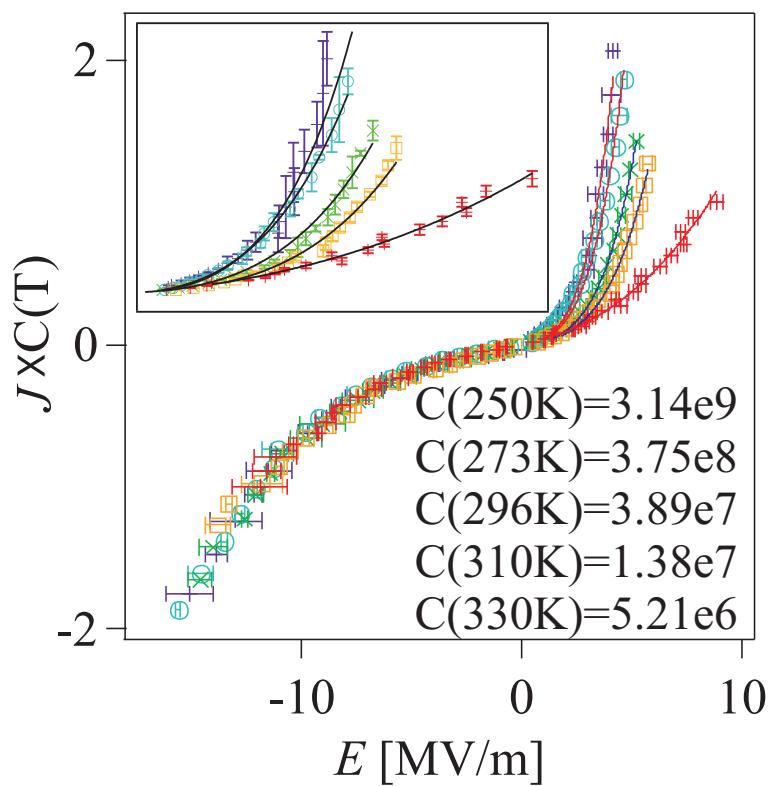
Figure 5.7: Current density scaled to the same magnitude at the extracting electrode. The inset shows fits to Eq. 5.3.

of Fig. 5.7 shows the fit to

$$J_{\text{inj}} \times C(T) = \frac{J_0 E}{\beta_b \sqrt{E} K_1(\beta_b \sqrt{E})}, \tag{5.3}$$

where $J_0/C(T) = \mu_0 \rho_0 w$.

5.2.1 Enhancement of electric-field barrier lowering

According to the Schottky model, the injection barrier is lowered due to the image force and β_b has a theoretical value of $[q^3/4\pi\varepsilon(kT)^2]^{1/2}$, where q is charge and $\varepsilon = 3\varepsilon_0$ is the dielectric constant for the films studied here. Our β_b values are two times larger than predicted by the Schottky theory. The disagreement is due to the neglect of energetic disorder in the Schottky model; the discrepancy has been observed by Monte Carlo simulations [5] that have accounted for energetic disorder. This has been reported by Barth *et al.* [17] for an injection-limited device. Recently, Burin and Ratner [9] have proposed an analytical expression that incorporates energetic disorder into the electric-field barrier-lowering effect:

$$\beta_b = \frac{1}{k_B T}\sqrt{\frac{q^3}{4\pi\varepsilon}} + \frac{2\sqrt{2}}{3}\frac{q\sigma}{k_B T}\sqrt{\frac{qa}{k_B T}}, \tag{5.4}$$

where a is the hopping distance and σ is the width of the Gaussian distribution of localized states. Fit to Eq. 5.4 yields $a = 1.1$ nm assuming $\sigma = 100$ mV, or $a = 0.6$ nm with $\sigma = 140$ mV. The calculated average distance between TPD molecules is reported to be no less than 0.6 nm [6]. The temperature dependence of the theories (T^{-1} vs $T^{-3/2}$) are indistinguishable with the presented data. The β_b at 330 K does not follow the general trend, possibly due to a damaged injecting electrode [Fig. 5.2(a)]. Since β_b at 330 K has dropped to the value predicted by Schottky theory, further experiment is needed to determine if the disorder contribution to barrier lowering is indeed eliminated at high temperature [35, 36].
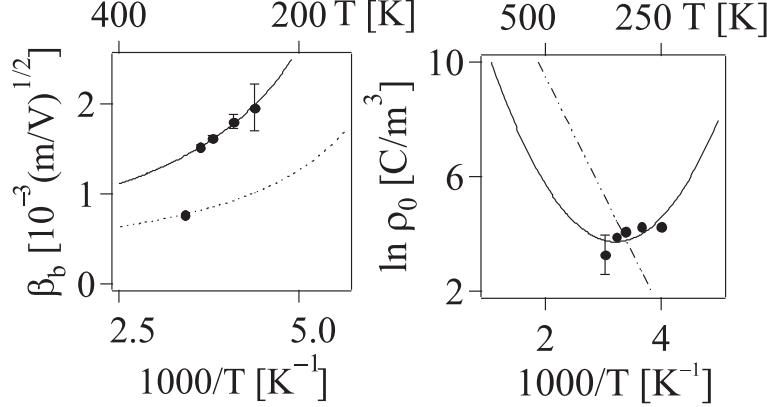
Figure 5.8: (a) Field dependence of barrier lowering vs temperature. The solid line is fit to Eq. 5.4. (b) Natural logarithm of injected charge density vs temperature, fitted to Eq. 5.5. The dashed line shows simple thermally activated charge density, with activation energy of 350 mV.

5.2.2 Injected charge density modified by energetic disorder

The injected charge density is extracted from the electric field according to Poisson's equation $dE/dx = \rho_0/\varepsilon$. In Fig. 5.8(b), the charge density is obtained from the slopes of linear fits to the electric-field profiles in the 2 µm region next to the injecting electrode, with $V_{sd} = 40$ V. The injected charge density cannot be explained by Arrhenius activation. Since the energy distribution of initially populated sites in organic semiconductors is displaced by $\sigma^2/k_B T$, the effective barrier is likewise reduced by energetic disorder [5, 37, 38]

$$\rho_0(T) = \rho_{\text{TPD}} \exp\left[-\frac{\Delta E}{k_B T} + \frac{1}{2}\left(\frac{\sigma}{k_B T}\right)^2\right], \qquad (5.5)$$

where $\rho_{\text{TPD}} = 2.66 \times 10^{26} m^{-3}$ is the concentration of TPD molecules calculated for our sample and ΔE is difference in energy between the work function of the contact metal and the ionization potential of the organic semiconductor. Fitting

to Eq. 5.5 gives the best fit values of $\Delta E = 0.74 \pm 0.04$ V and $\sigma = 140 \pm 14$ mV. Compared to the interfacial electronics structure obtained from UV photoemission spectroscopy ($\Delta E = 0.8 - 1.3$ V) in Ref. [20], the fit value here is slightly lower but is still reasonable since our sample preparation and thickness is quite different from Ref. [20]. The value of σ from the above fit is also within the usual reported range of $50 - 150$ mV.

5.3 Conclusions

An ohmic contact is observed to become injection-limited upon increasing temperature; fewer space charges are injected and the interface region becomes more depleted of holes. However, the potential drop becomes indistinguishable when the applied bias is large. The field-assisted barrier lowering is more efficient than expected from the Schottky theory, because energetic disorder reduces the injection barrier by broadening the number of available states for charge injection. The temperature-dependent disorder contribution is readily distinguished from the mobility effect in the injected current by comparing the current density at the injecting and extracting electrodes. Direct potential and electric-field measurements allow the injected charge density to be inferred, and it does not follow simple Arrhenius behavior. This can be explained by incorporating energetic disorder into the activation energy.

CHAPTER 5 REFERENCES

[1] J. C. Scott, J. Vac. Sci. Technol. A **21**, 521 (2003).

[2] Y. L. Shen, A. R. Hosseini, M. H. Wong, and G. G. Malliaras, ChemPhysChem **5**, 16 (2004), and references therein.

[3] H. Bässler, Phys. Status Solidi B **175**, 15 (1993).

[4] I. N. Hulea et al., Phys. Rev. Lett. **93**, 166601 (2004).

[5] Y. N. Gartstein and E. M. Conwell, Chem. Phys. Lett. **255**, 93 (1996).

[6] V. I. Arkhipov, E. V. Emelianova, Y. H. Tak, and H. Bässler, J. Appl. Phys. **84**, 848 (1998).

[7] M. A. Baldo and S. R. Forrest, Phys. Rev. B **64**, 085201 (2001).

[8] Y. Preezant and N. Tessler, J. Appl. Phys. **93**, 2059 (2003).

[9] A. L. Burin and M. A. Ratner, J. Polym. Sci.: Pt. B: Polym. Phys. **41**, 2601 (2003).

[10] J. A. Freire and G. Voss, J. Chem. Phys. **122**, 124705 (2005).

[11] P. K. H. Ho et al., Nature **404**, 481 (2000).

[12] S. V. Novikov, D. H. Dunlap, V. M. Kenkre, P. E. Parris, and A. V. Vannikov, Phys. Rev. Lett. **81**, 4472 (1998).

[13] D. H. Dunlap, P. E. Parris, and V. M. Kenkre, Phys. Rev. Lett. **77**, 542 (1996).

[14] W. F. Pasveer et al., Phys. Rev. Lett. **94**, 206601 (2005).

[15] P. M. Borsenberger and D. S. Weiss, *Organic Photoreceptors for Xerography*, Optical Engineering, Marcel Dekker, Inc., New York, 1998.

[16] Y. Shen, M. W. Klein, D. B. Jacobs, J. C. Scott, and G. G. Malliaras, Phys. Rev. Lett. **86**, 3867 (2001).

[17] S. Barth et al., Phys. Rev. B **60**, 8791 (1999).

[18] T. van Woudenbergh, P. W. M. Blom, M. C. J. M. Vissenberg, and J. N. Huiberts, Appl. Phys. Lett. **79**, 1697 (2001).

[19] B. H. Hamadani and D. Natelson, J. Appl. Phys. **97**, 064508 (2005).

[20] H. Ishii, K. Sugiyama, E. Ito, and K. Seki, Adv. Mater. **11**, 605 (1999).

[21] A. B. Chwang and C. D. Frisbie, J. Phys. Chem. B **104**, 12202 (2000).

[22] T. Hassenkam, D. R. Greve, and T. Bjornholm, Adv. Mater. **13**, 631 (2001).

[23] X. Cui, M. Freitag, R. Martel, L. Brus, and P. Avouris, Nano Lett. **3**, 783 (2003).

[24] J. A. Nichols, D. J. Gundlach, and T. N. Jackson, Appl. Phys. Lett. **83**, 2366 (2003).

[25] L. Bürgi, T. J. Richards, R. H. Friend, and H. Sirringhaus, J. Appl. Phys. **94**, 6129 (2003).

[26] K. P. Puntambekar, P. V. Pesavento, and C. D. Frisbie, Appl. Phys. Lett. **83**, 5539 (2003).

[27] W. R. Silveira and J. A. Marohn, Phys. Rev. Lett. **93**, 116104 (2004).

[28] O. Tal, W. Gao, C. K. Chan, A. Khan, and Y. Rosenwaks, Appl. Phys. Lett. **85**, 4148 (2004).

[29] E. M. Muller and J. A. Marohn, Adv. Mater. **17**, 1410 (2005).

[30] P. N. Murgatroyd, J. Phys. D-Appl. Phys. **3**, 151 (1970).

[31] A. A. Grinberg, S. Luryi, M. R. Pinto, and N. L. Schryer, IEEE Trans. Elec. Dev. **36**, 1162 (1989).

[32] M. A. Lampert and P. Mark, *Current Injection in Solids*, Academic Press, 1970.

[33] P. W. M. Blom, C. Tanase, D. M. de Leeuw, and R. Coehoorn, Appl. Phys. Lett. **86**, 092105 (2005).

[34] M. Abkowitz, J. S. Facci, and J. Rehm, J. Appl. Phys. **83**, 2670 (1998).

[35] U. Wolf, S. Barth, and H. Bässler, Appl. Phys. Lett. **75**, 2035 (1999).

[36] V. I. Arkhipov, H. von Seggern, and E. V. Emelianova, Appl. Phys. Lett. **83**, 5074 (2003).

[37] G. Akuetey and J. Hirsch, Phil. Mag. B **63**, 389 (1991).

[38] G. Sasvari and C. Juhasz, J. Phys.: Condens. Matter **9**, 6493 (1997).

Chapter 6

Charge traps and charge diffusion in molecularly doped polymers

6.1 Release kinetics of trapped charges

Besides their application in xerography [1], molecularly doped polymers have been the model system for testing charge injection and transport theories for disordered organic semiconductors, because they are free of charge traps, as measured by time-of-flight experiments at room temperature [2,3]. Nevertheless, at 250K and 230 K, the presence of charge traps is detected by EFM in TPD-PS and TPD-PC (see Fig. 3.1 for chemical structures). After operation with $V_{sd} = 10$ V, potential profiles do not immediately settle back to the initial values found in Fig. 5.2(e) when the device is turned off. Figure 6.1(a) shows the gradual decrease of potential, which is largest in the middle of the device channel because trapped charges located in the middle are farthest away from the electrodes and will take the longest time to diffuse back into the grounded electrodes. The rate of potential decay measures the release kinetics of trapped charges. In Fig. 6.1(b), the declining potentials are fitted to an exponential with respect to time, $\phi(t) = \phi_0 \exp(-kt) + \phi_\infty$, where ϕ_0 is the initial potential due to trapped charges immediately after the electrodes are grounded, k is the rate of decay of the electrostatic potential, and ϕ_∞ is the potential offset between the metal electrodes and the semiconductor when all the trapped charges have been released. The fit values are listed in Table 6.1.
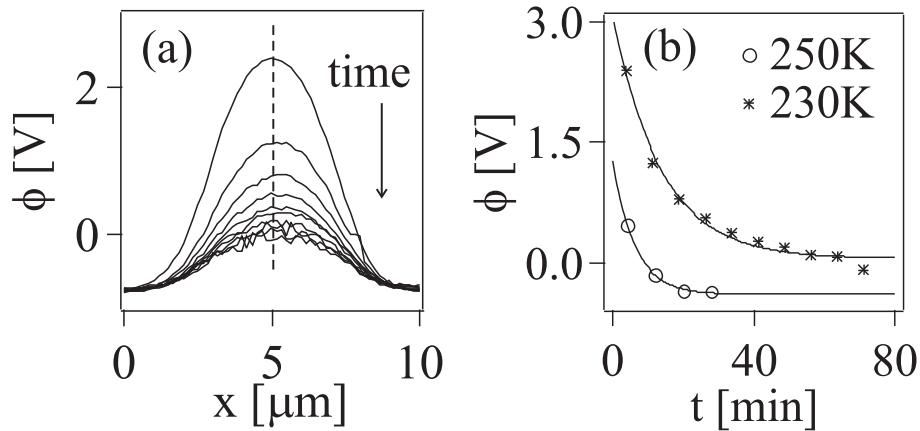
Figure 6.1: (a) Potential profiles at 230 K after the device is turned off. (b) Potentials decay with time at 250 K (open circles) and at 230 K (asterisks). The potential is taken at the position indicated by the dashed line in (a).

A rough estimate of the activation energy for the rate of potential decay is obtained using first-order rate equations

$$k = k_0 \exp\left(\frac{-qV_{\text{act}}}{k_B T}\right), \tag{6.1}$$

$$\ln k_1 - \ln k_2 = \frac{-qV_{\text{act}}}{k_B}\left(\frac{1}{T_1} - \frac{1}{T_2}\right); \tag{6.2}$$

V_{act} is found to be 190 mV, and $k_0 = 1.47 \times 10^3 \, \text{min}^{-1}$. Substituting V_{act} and k_0 into Eq. 6.1, the rates of potential decay can be extrapolated at other temperatures. For example, at 296 K and 330 K the rates are $0.74 \, \text{min}^{-1}$ and $1.47 \, \text{min}^{-1}$, respectively; the corresponding trap release time is 1.4 min at 296 K and 0.7 min at 330 K. Since EFM has much higher charge sensitivity than conventional current measurements, at sufficiently low temperatures EFM can resolve deep traps being released. TPD-PS may appear to be trap-free at the short-time scale probed by time-of-flight studies, but deep traps do exist and their slow release is observable with EFM.

Table 6.1: Best-fit values for the potential decay in Fig. 6.1.

| T [K]	ϕ_0 [V]	ϕ_∞ [V]	k [min^{-1}]
230	3.0 ±0.2	0.05 ±0.06	0.073 ±0.008
250	1.7 ±0.1	-0.40 ±0.03	0.162 ±0.021
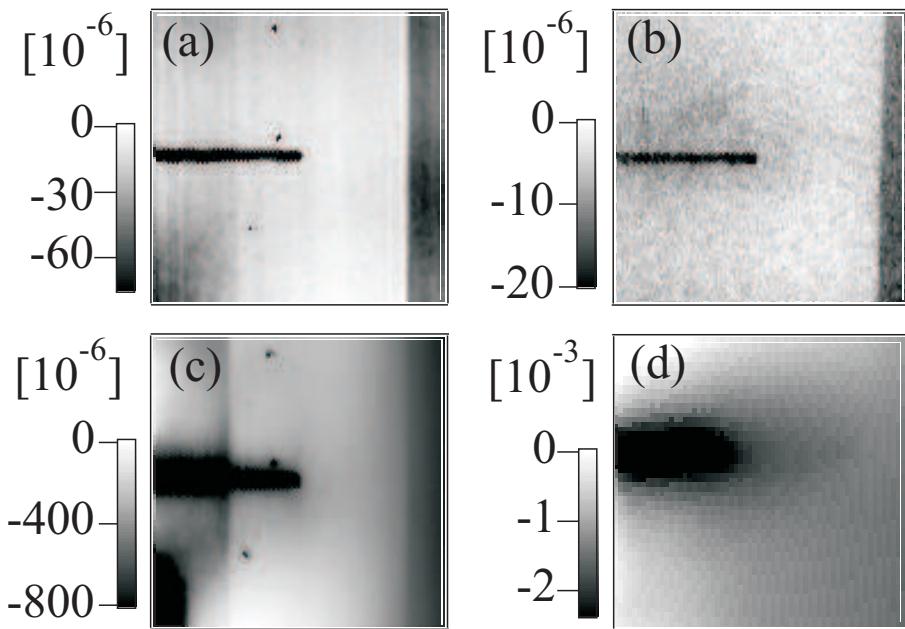
Figure 6.2: Force-gradient images of perpendicular (versus parallel plates) coplanar Au electrodes with 100 nm of spin-casted TPD-PS. The image scale is $(f - f_0)/f_0$ (unitless). $V_{sd} = 0$ V in (a,b) and $V_{sd} = 20$ V in (c,d), where the plate electrode is grounded. The left electrode is partially covered by a layer of oxide 50 nm thick in (a,c) but left bare in (b,d).

6.2   Diffusion of trapped charges

The ability to visualize charge locations by EFM [4–8] may be applied to study charge diffusion in organic semiconductors, which is of interest because significant deviations from the classical Einstein mobility-diffusion relation $D = \mu k_B T/q$ have been predicted for disordered materials [9, 10]. Enhanced diffusion leads to dispersive transport, broadens the rise time in LEDs, and has other implications for organic electronics. The following images are an initial attempt to look at trapped charge diffusion with a perpendicular (versus the usual parallel plates) electrode geometry. This configuration is designed to inject charges from a point source. At first a 50 nm layer of oxide is deposited on top of the horizontal electrode, keeping only 3 μm of exposed metal at the end for charge injection [Fig. 6.2(a)]. Due to lithography alignment issues, the exposed metal section is rather large and not really a point source; moreover, the oxide is charged up during operation [Fig. 6.2(b)]. Before spending more efforts to make proper point-source devices, perpendicular substrates without an oxide layer [Fig. 6.2(c,d)] are used below to image charge diffusion. To allow more time for EFM imaging, the temperature is lowered to 230 K, and the polymer host for TPD is switched from polystyrene (PS) to polycarbonate (PC) to lower the charge mobility [3].

Figure 6.3 illustrates the spatial progression of trapped charges with time. Each image takes 6 min to acquire, scanning from left to right. Generally, red areas with large frequency shifts are regions with high potential and therefore trapped charges. While both metal electrodes are grounded in Fig. 6.3(a) and (c-f), they show large frequency shifts not due to potential but because of high local capacitance. The electrodes are on top of the quartz substrate and closer to the

tip than the rest of the device area.* The trapped charges initially concentrate on the equipotential almost midway between the two electrodes. The charges diffuse away from the middle to both sides as time passed.

6.3 Conclusions

EFM has measured trap release kinetics and imaged charge diffusion in molecularly doped polymers. Although it is not possible to infer the diffusion constant here, a corral device geometry, as shown in Ref. [11], may provide quantitative results. It would be interesting to see if the diffusion constants of TPD vary with different polymer hosts.

*The height of the cantilever tip is fixed. Tip scanning is not at constant height with respect to surface topography.
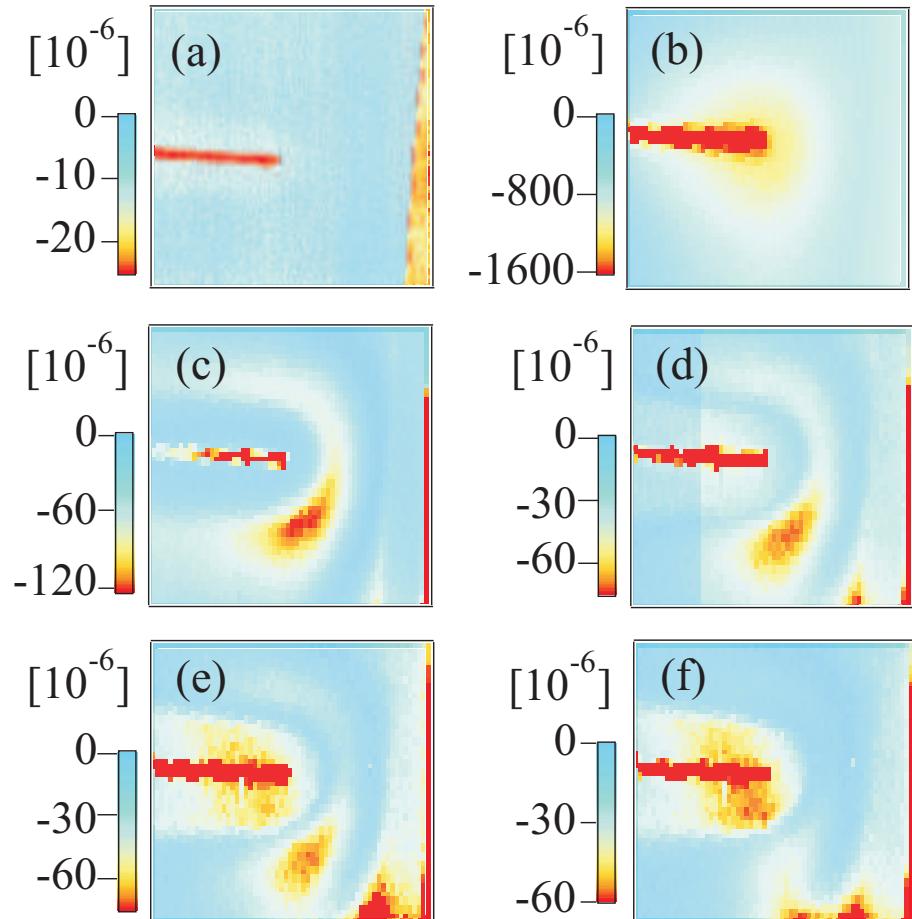
Figure 6.3: Force gradient images of trap diffusion in TPD-PC. The image scale is $(f - f_0)/f_0$ (unitless). (a) Initial image with $V_{sd} = 0\,\text{V}$. (b) $V_{sd} = 20\,\text{V}$ with plate electrode grounded. (c) 0-6 min, (d) 6-12 min, (e) 12-18 min, and (f) 18-24 min after both electrodes are grounded.

CHAPTER 6 REFERENCES

[1] P. M. Borsenberger and D. S. Weiss, *Organic Photoreceptors for Xerography*, Optical Engineering, Marcel Dekker, Inc., New York, 1998.

[2] Y. Shen, M. W. Klein, D. B. Jacobs, J. C. Scott, and G. G. Malliaras, Phys. Rev. Lett. **86**, 3867 (2001).

[3] H. J. Yuh and D. M. Pai, Mol. Cryst. Liq. Cryst. **183**, 217 (1990).

[4] T. D. Krauss and L. E. Brus, Phys. Rev. Lett. **83**, 4840 (1999).

[5] L. Bürgi, H. Sirringhaus, and R. H. Friend, Appl. Phys. Lett. **80**, 2913 (2002).

[6] J. A. Nichols, D. J. Gundlach, and T. N. Jackson, Appl. Phys. Lett. **83**, 2366 (2003).

[7] K. P. Puntambekar, P. V. Pesavento, and C. D. Frisbie, Appl. Phys. Lett. **83**, 5539 (2003).

[8] E. M. Muller and J. A. Marohn, Adv. Mater. **17**, 1410 (2005).

[9] R. Richert, L. Pautmeier, and H. Bässler, Phys. Rev. Lett. **63**, 547 (1989).

[10] Y. Roichman and N. Tessler, Appl. Phys. Lett. **80**, 1948 (2002).

[11] L. Bürgi, R. H. Friend, and H. Sirringhaus, Appl. Phys. Lett. **82**, 1482 (2003).

Chapter 7

Kinetics of trap formation and dissociation

Device stability is critical for practical applications of organic field-effect transistors (OFETs) [1]. Degradation in OFETs occurs under continuous applied bias; bias stress is said to be observed when the current decreases with operation time [2–4] or when the threshold voltage shifts after consecutive transfer measurements [5–9]. For polymeric semiconductors, the decrease in current is due to mobile charges being trapped in the polymer [10] with at least two kinds of trap states [4]. Even though charge traps are not located inside the dielectric, the dielectric significantly affects device stability because it influences the molecular ordering [11] at the semiconductor/dielectric interface, where charge is transported at the first two molecular layers next to the dielectric in OFETs [12].

Degradation due to charge trapping is a competing process between the capture and the release of mobile charges. We have investigated the kinetics of trap formation and dissociation in OFETs with different processing parameters for the semiconductor/dielectric interfaces, to understand how annealing conditions and dielectric surface treatments change device stability. The kinetics of trap formation is obtained by current-voltage (IV) measurements to deduce the reaction mechanism. The stability of trap states is inferred from the release kinetics measured by electric force microscopy (EFM), which also images the spatial distribution of trapped charges.

Trap formation was observed in a regioregular poly(thiophene), PQT [13], while trap release was measured for two different polymers, PQT and poly(9-9'-dioctyl-fluorene-co-bithiophene) (F8T2), and amorphous silicon (a-Si). The OFETs were
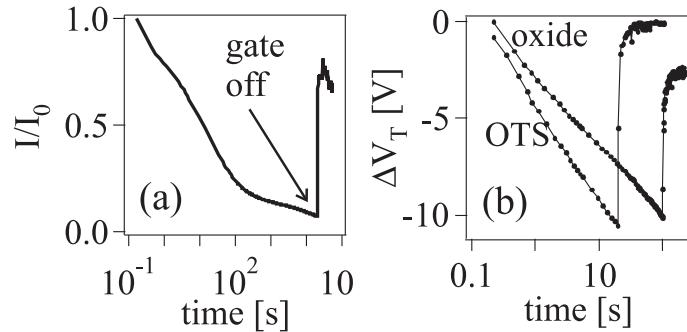
Figure 7.1: Normalized current (a) and threshold voltage shift due to $V_g = -20\,\text{V}$ (b) as a function of operation time for PQT OFETs.

fabricated in the bottom gate configuration and were fabricated on 100 nm of silicon thermal oxide (capacitance $30\,\text{nF/cm}^2$) with 30 nm gold source-drain contacts. After oxygen plasma cleaning, the dielectric surface either underwent no further treatment or was modified with a cross-linked monolayer of octadecyltrichlorosilane (OTS) [14, 15]. The organic semiconductors (0.5 wt% F8T2 in xylene or 0.1% PQT in dichlorobenzene) was spin-coated onto the substrate at 1000 rpm and had thickness of 40 nm. In vacuum and in the dark, the as-spun films were first measured and then annealed at 130 °C. Amorphous silicon devices were fabricated by William Wong at 130 °C on 250 nm silicon nitride dielectric (capacitance $20\,\text{nF/cm}^2$) in bottom gate configuration. This work was carried out at Cornell and at Palo Alto Research Center.

7.1 Kinetics of trap formation

The gradual reduction in current with operation time shows a fast initial decrease and a slow drop at extended time without establishing equilibrium in a PQT OFET [Fig. 7.1(a)]. Similarly, after the dc gate bias is turned off, bias stress is rapidly reversed in the first few seconds but slows down subsequently.
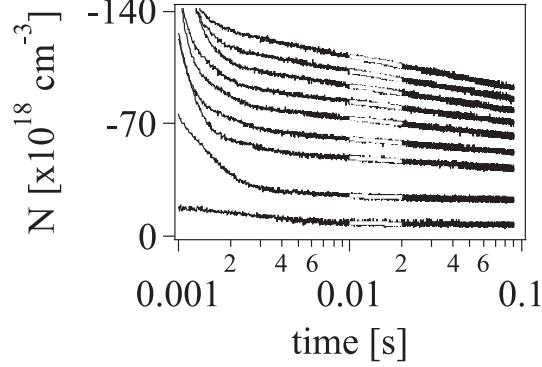
Figure 7.2: (a) Free carrier decay as a function of gate voltage (from -10 V to -70 V), showing faster decay at higher gate voltage. White lines are fits to obtain dN/dt.

Figure 7.1(b) illustrates the stress-recovery behavior in terms of threshold voltage shift [4] ΔV_T found from

$$\Delta V_T(t) = \left(1 - \frac{I(t)}{I_0}\right)\left(V_g - V_T^0\right), \tag{7.1}$$

where $I(t)$ is the output current at time t, V_g is the applied gate bias, and I_0 and V_T^0 are the current and threshold voltage at $t = 0$, respectively. Comparing devices of the same dimensions but subjected to different dielectric treatments, we find that ΔV_T decreases faster with an OTS interface than for untreated oxide, indicating higher rate of trap formation with OTS at this time scale. Since ΔV_T was shifted by the same magnitude (-10 V), the same number of charges have been captured in both devices when the gate bias is turned off. The device with OTS has completely recovered in 80 s, while the untreated device has long-lived trap states that last longer than 120 s, despite similar trap concentrations at the beginning of recovery. The OTS interface has lead to fast charge capture as well as rapid trap release; a more quantitative analysis of this observation is given below.

Because the applied gate bias (-10 V to -70 V) is always larger than the source-drain bias (-3 V), the concentration of mobile carriers N can be inferred from the linear current using the gradual channel approximation

$$I_{sd}/V_{sd} = (W/L)C_g\mu(V_g - V_T) = (W/L)\mu N d, \qquad (7.2)$$

where W/L is the geometry factor, C_g is the gate capacitance per unit area, μ is the mobility, and d is the effective width of the accumulation layer, estimated as $1\,\text{nm}$ here. Figure 7.2 demonstrates that mobile holes decay faster with more negative gate voltage, indicating that trap formation depends on charge concentration ($N = C_g V_g$) and ruling out zero-order kinetics.

The decay of free holes dN/dt is obtained by linear fits to Fig. 7.2 at short times, 10–15 ms after V_g is turned on; for this time range we can avoid capacitance charging effects but can still assume that trap release is negligible. The kinetics of trap formation is investigated by plotting dN/dt against N (first-order kinetics) or N^2 (second order kinetics). It has been suggested that hole pairs bind together to become bipolarons during bias stress (second-order) [2, 3], but optical spectroscopy [16, 17] suggests that well-ordered polymers form isolated polarons instead (first-order). Previous bias stress studies have also reported that processing conditions [18–20] and water in the environment [5, 8] affect device stability. Because the residuals are similar in the fits to N or N^2, it is not possible to distinguish whether the bipolaron or the polaron model is a more appropriate trap formation mechanism for our OFETs studied in vacuum (Fig. 7.3).

Although the reaction mechanism is not conclusively determined, the rate constants for trap formation k, regardless of the order of kinetics, is larger for interfaces with OTS than for oxide, although only by $\sim 3\times$ at most. Table 7.1 lists all linear fit values for k, and the rate constant in Fig. 7.4(a) is from fitting to N^2. The higher k for OTS is consistent with Fig. 7.1(b), in which the device
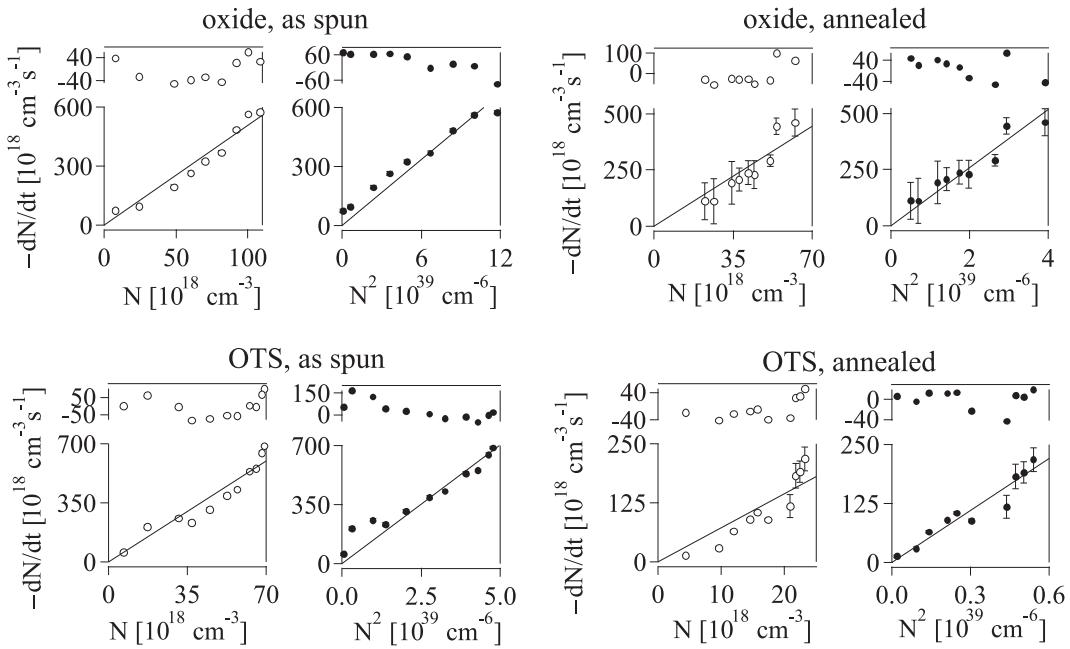
Figure 7.3: Charge removal rate as a function of N or N^2 for different processing conditions. The fit residuals are shown in the offset at the top.

with OTS shows faster current decay. The effect of annealing on trap formation is unclear, considering the incongruity seen in the various values of the first-order rate constant k_P.

Mobility μ increases after annealing for OTS but decreases for oxide [Fig. 7.4(b)]. While both mobility and charge trapping are affected by disordered regions in a polymer [21], Fig. 7.4(b) shows that higher μ does not leads to larger k for the device with oxide interface. To extract the mobility, the output and transfer curves were all fitted simultaneously (Fig. 7.5), to avoid an overestimated μ from fitting only to the saturation current [22].

7.2   Kinetics of trap dissociation

In IV measurements, the recovery of ΔV_T is probed by short ($\sim$ 25 ms) gate pulses to measure the current recovery. The wait time between gate pulses must be
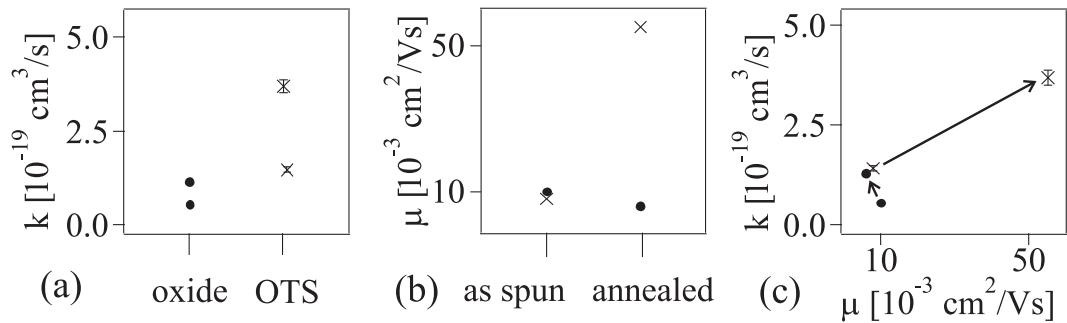
Figure 7.4: Rate of trap formation from the fit of $-dN/dt$ from 10 to 20 ms vs N^2 at 15 ms (a) and mobility (b) versus annealing conditions and dielectric interfaces. Cross: OTS; circle: oxide. (c) Rate of trap formation vs mobility. The arrows indicate how mobility changes upon annealing.
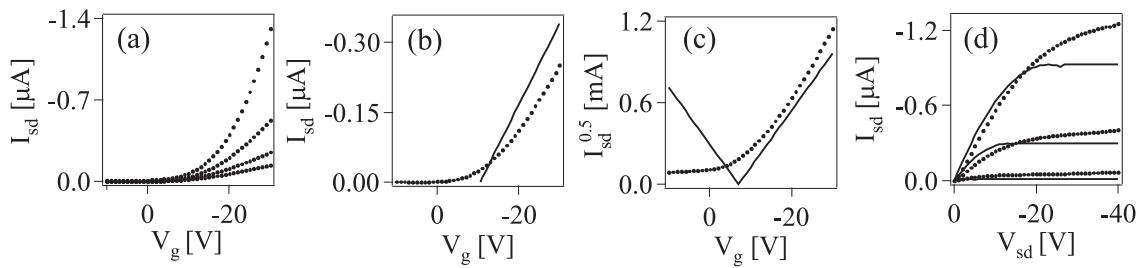

Figure 7.5: (a) Transfer characteristics at $V_{sd} = -3$ V, -5 V, -10 V, and -40V. Fits to transfer curves of $V_{sd} = -5$V (b) and square root of $V_{sd} = -40$V (c). (d) Fits to output characteristics at $V_g = -10$ V, -20 V, and -30 V.

Table 7.1: Best-fit values for the rate of trap formation. k_P corresponds to first-order reaction N, and k_{BP} to second-order reaction N^2.

	k_P [s^{-1}]	k_{BP} [10^{-19} cm^{3}s^{-1}]
oxide, as spun	5.06 $\pm$0.19	0.56 $\pm$0.03
oxide, annealed	6.36 $\pm$0.43	1.29 $\pm$0.07
OTS, as spun	8.53 $\pm$0.34	1.41 $\pm$0.07
OTS, annealed	7.24 $\pm$0.58	3.69 $\pm$0.18

sufficiently long; otherwise, too-frequent gate pulses cause additional bias stress and do not allow the current to recover as in Fig. 7.1(a). EFM does not induce bias stress, because it directly measures potential changes to monitor trap release [23, 24], during which the source, drain, and gate electrodes are always grounded. Moreover, the scanning capability of EFM provides a spatial map of trapped charges. Presently, EFM cannot measure traps shielded by mobile charge [24], and currently the EFM temporal resolution is much slower than IV measurements.

In EFM, the capacitive tip-sample force gradient leads to a resonance frequency f of

$$f(V_{\text{tip}}, x) = f_0 - \frac{f_0}{4k_0} \frac{\partial^2 C}{\partial z^2} [V_{\text{tip}} - \phi(x)]^2, \tag{7.3}$$

where f_0 is the intrinsic cantilever resonance frequency, k_0 is the intrinsic cantilever spring constant, C is the tip-sample capacitance, z is the tip-sample separation, V_{tip} is the applied tip voltage, and ϕ is the potential difference between the cantilever tip and the sample. Varying V_{tip} within $\pm 2\,\text{V}$ of ϕ, f is quadratic in V_{tip} to within a percent. Fitting f to Eq. 7.3 allows us to infer $\partial^2 C/\partial z^2$ and ϕ at different location x in the sample. Force gradient images, with scales of $(f - f_0)/f_0$, are taken with a constant tip voltage.

7.2.1 PQT

For PQT-oxide and PQT-OTS (Fig. 7.6), the force gradient images display no difference before and after bias stress, but the IV transfer measurements taken after the images reveal that V_T is shifted and therefore charges are still trapped inside the polymers. To understand why EFM cannot detect the trapped charges in PQT, we need to examine the tip response at positive gate biases. In a purely hole conductor under positive V_g [Fig. 7.7(a)], the semiconductor does not accumulate
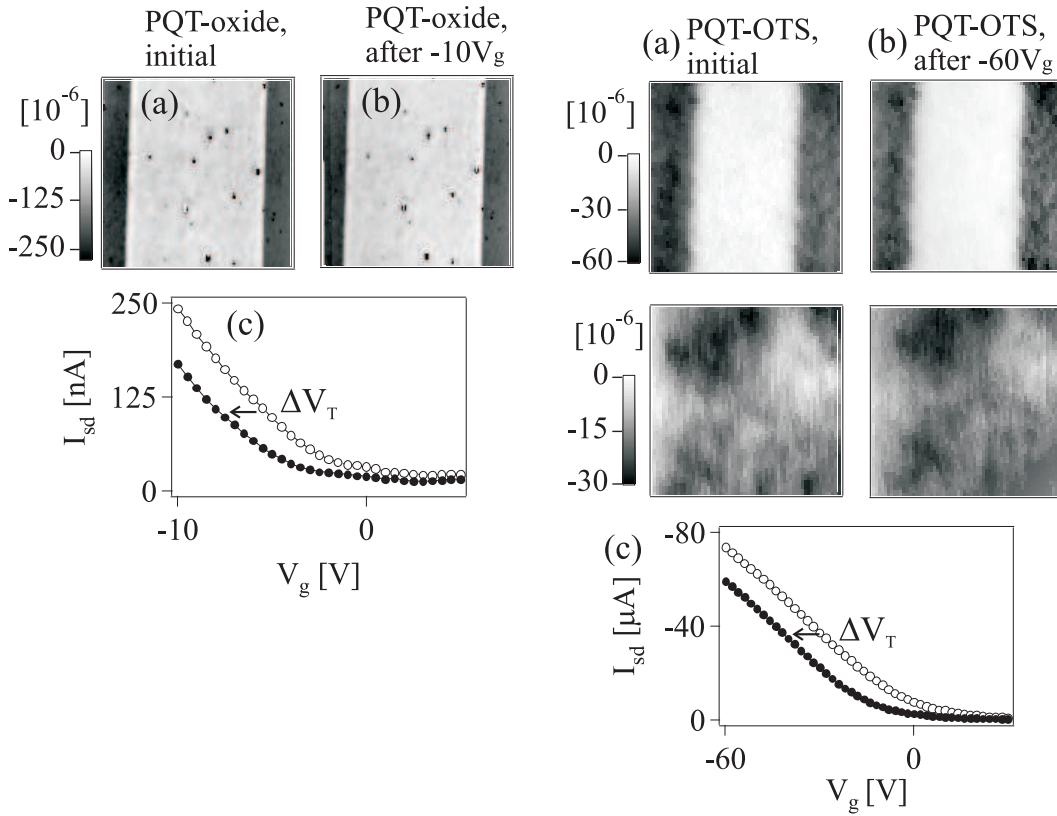
Figure 7.6: Force gradient images of PQT-oxide (left) and PQT-OTS (right) before (a) and after (b) bias stress. (c) Threshold voltage shift obtained by IV measurements. Zoom-in views of the channel on the right show no difference before and after stress.

negative charges and the EFM tip will measure a potential equivalent to the applied gate bias. However, if the semiconductor is ambipolar or has negatively charged impurities, the gate bias will be shielded from the tip. Figure 7.7(b) shows that, for PQT, the potential is only $\sim 50\,\mathrm{mV}$ even at the high gate bias of 50 V, in contrast with another polymer F8T2, over which the tip follows the positive gate biases almost exactly [Figure 7.7(c, d)]. The potential due to a negative V_g is fixed at 0 V, because holes have accumulated into a conducting sheet that connects the grounded source and drain electrodes. Negative gate biases are completely shielded from the EFM tip.
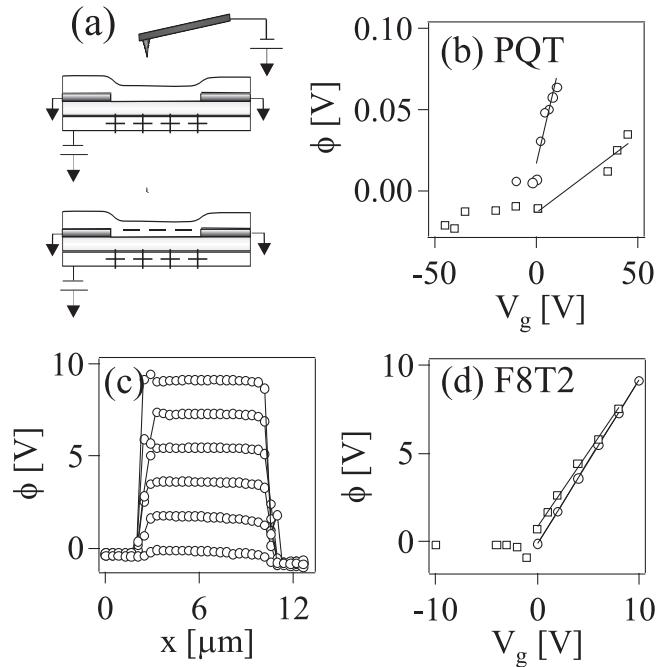
Figure 7.7: (a) Top: without charge shielding the EFM tip will detect a potential that matches the gate bias. Bottom: the EFM tip is shielded from the gate bias by induced charges or ionic impurities. Potential as a function of gate bias for PQT (b) and for F8T2 (c, d). Square markers: OTS; circle markers: oxide. In (c) the potential across the device channel is shown as a function of gate voltage, from $0 - 10\,\text{V}$ in increments of $2\,\text{V}$.

Table 7.2: Slope of the potential under positive gate biases.

	$d\phi/dV_g$ [unitless]
PQT oxide	0.00525
PQT OTS	0.00094
F8T2 oxide	0.929
F8T2 OTS	0.898
a-Si	0.269

The PQT device with an oxide interface appears to be less shielded than the device with OTS. There is virtually no difference in the potential responses for F8T2 on different dielectric interfaces. Table 7.2 compares the slope of the potential under positive gate biases for different semiconductors. Depletion instability attributed to an electronic process of negative charge trapping has been observed in another poly(thiophene), poly(3-hexylthiophene) (P3HT) [25]. Recently Chua *et al.* [26] has demonstrated n-type field effect in both P3HT and F8T2. While electron accumulation is possible for both PQT and F8T2 films, the extent of charge shielding is much larger in PQT. Two possibilities to explain the observed difference are that the PQT films have more negatively charged impurities than F8T2, or PQT is a better ambipolar semiconductor, which would be very interesting indeed for n-type OFET applications.

7.2.2   F8T2

Because of charge shielding in PQT, its trap-release kinetics cannot be detected by EFM. To continue the study of trap dissociation, other semiconductors, namely F8T2 and a-Si, are investigated by EFM. Force-gradient images in Fig. 7.8, taken at the same area with all the electrodes grounded, illustrates the release of trapped
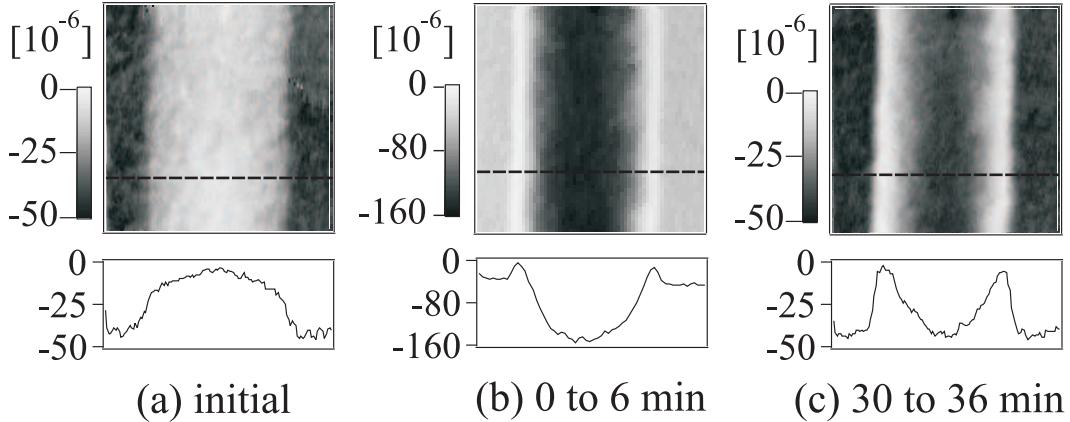
Figure 7.8: (a) Force-gradient images (10×10 µm^2) of a F8T2-OTS device, taken with $V_{\text{tip}} = 1$ V. (a) Before stress. (b, c) After bias stress with $V_g = -10$ V. The line profiles are taken at the location indicated by the dashed line.

charges with time. Compared to the initial image taken before stress bias is induced, the channel region in the stressed device exhibits a large frequency shift due to trapped charges. As time passes, the charges leak out and the image gradually reverts back to its initial state.

One should be aware that changes in both the capacitance second derivative $\partial^2 C / \partial z^2$ and the potential ϕ contribute to the frequency shift in EFM images (see Eq. 7.3). To separate the two quantities, tip voltage is varied at each location, and the resulting frequency parabola can be fitted to obtain $\partial^2 C / \partial z^2$ from the parabola curvature and ϕ from the parabola maximum. Figure 7.9 shows the local potential and capacitance second derivative in a F8T2 device with a 2 µm channel. Before bias stress, the potential difference between the polymer and the electrodes is only 60 mV at most. The capacitance second derivative follows device topography, because the tip is scanned at a fixed height and does not feedback to the sample surface. When a negative gate bias is applied, holes accumulate and increase the capacitance in the channel. The potential change is still very small due to the sheet of charges being grounded with source-drain electrodes. After
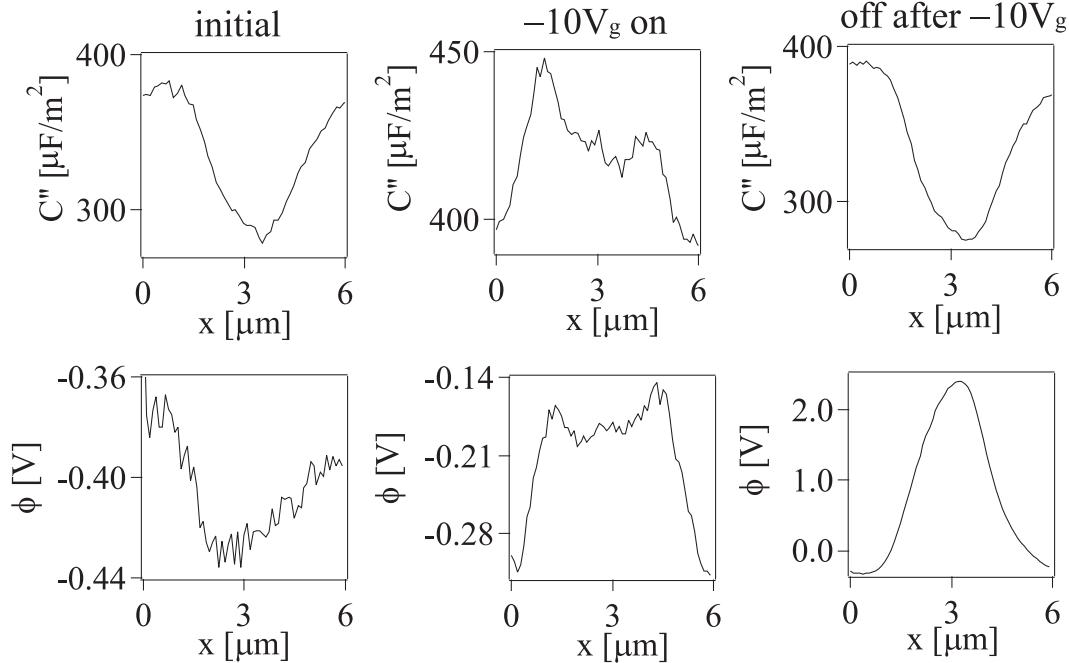
Figure 7.9: Second derivative of tip-sample capacitance (top row) and potential (bottom row) as a function of tip location over a F8T2-OTS device.

the gate bias is turned off, some trapped charges remain which lead to a large potential inside the channel. The capacitance reverts back to the initial state, since the remaining charges are not detectable with the tip height set at 100 nm. The observations provided by Fig. 7.9 help us to better understand the bumps near the electrodes seen in the line profiles of Fig. 7.8(b, c). The bumps are results of adding together the contributions from $\partial^2 C/\partial z^2$ and ϕ, which have opposite signs after bias stress.

The trap distribution in F8T2 is spatially homogeneous, in contrast to Fig. 4 in Ref. [24] which provides a spatial distribution of traps in pentacene on oxide. The difference in trap distribution is mainly due to the semiconductors (polymeric vs polycrystalline) and is not related to the dielectric interfaces, since F8T2-OTS and F8T2-oxide show similar variations in their force-gradient images (lateral resolution $\sim$ 100 nm). The force-gradient image roughly correlates with sample to-
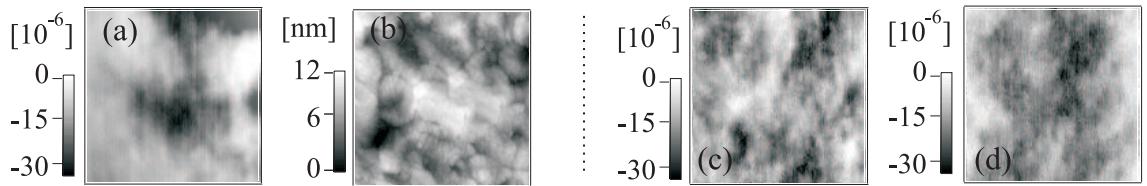
Figure 7.10: $2 \times 2\,\mu m^2$ images of F8T2, annealed at $130\,°C$. Force-gradient image (a) and topography (b) of the same area. (c) Another area inside the channel before stress. (d) Same area as (c) but after bias stress with $V_g = -3V$. EFM images are taken with $V_{\text{tip}} = 1\,V$.

pography; the dark areas with high frequency shift in Fig. 7.10 (a) corresponds to raised regions in the sample [Fig. 7.10 (b)]. Comparison of the same area before [Fig. 7.10(c)] and after bias stress [Fig. 7.10(d)] reveals different potential variations. Certain areas in the polymer are more stable for charge trapping. Disordered molecular arrangements and electronic disorder [27] are possible causes.

In Fig. 7.11, EFM potentials are correlated to IV measurements. For a device where V_T has shifted by 6V according to transfer curves, the EFM potential profiles demonstrate the same amount of potential change. Similarly, the tip response to gate bias indicates hole shielding at negative V_g until -6 V. The slope of the potential is not affected because electrons are not accumulated in our F8T2 devices.

The trap release rate for F8T2-OTS is faster than for F8T2-oxide, as seen in Fig. 7.12. In 70 min the potential of OTS has decayed by 1 V, while for oxide the potential has dropped by only 0.4 V in 160 min. The potential decay indicates that traps are being released with time in an exponential manner

$$\phi(t) = \phi_0 \exp(-t/t_r) + \phi_\infty, \tag{7.4}$$
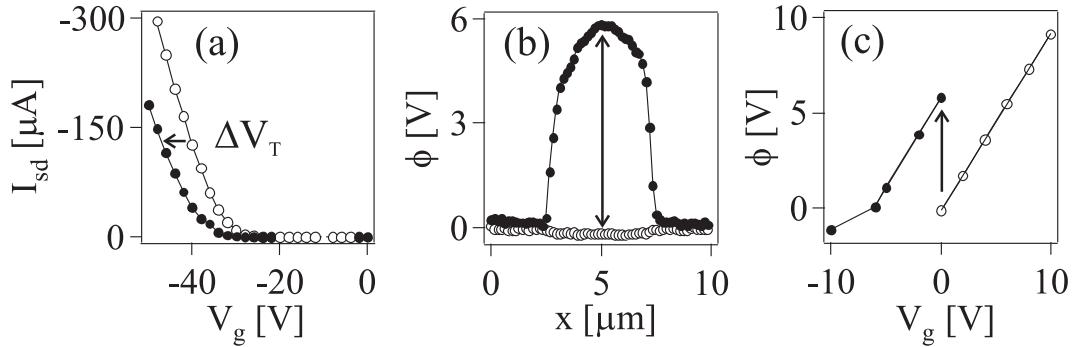
Figure 7.11: Threshold voltage shift seen in IV measurements (a) and EFM potential profiles (b, c) for F8T2-oxide.

Table 7.3: Rate of potential decay measured by EFM.

	ϕ_∞ [V]	ϕ_0 [V]	t_r^{-1} [min^{-1}]	t_r [min]
F8T2, oxide	9.29 ±0.05	0.39 ±0.05	0.016 ±0.006	63 ±23
F8T2, OTS	1.26 ±0.11	1.36 ±0.09	0.030 ±0.006	33 ±6
a-Si	-0.11 ±0.07	-13.86±0.78	0.442 ±0.026	2 ±0.1

where ϕ_0 is the potential immediately after gate bias is removed, ϕ_∞ is the potential at long time, and t_r^{-1} is the rate of potential decay. The fit values are listed in Table 7.3. Here all the traps have not been dissociated, and the fit is to allowed to level off at a nonzero value to find the short term decay time immediately after bias is removed. Since the previous stress histories of the devices are different, the initial amount of trapped charges are not the same. Even though the oxide device has more charges initially, it still releases trapped charges at a slower rate. Traps in the oxide device are more stable. Relating back to the trap formation studies (albeit on a different polymer PQT), both trap formation and dissociation are faster in devices with OTS dielectric interfaces than in devices with untreated oxide interfaces. Slower charge trapping is due to a higher energy barrier, but once a charge is trapped, it takes longer to be released due to the same barrier.
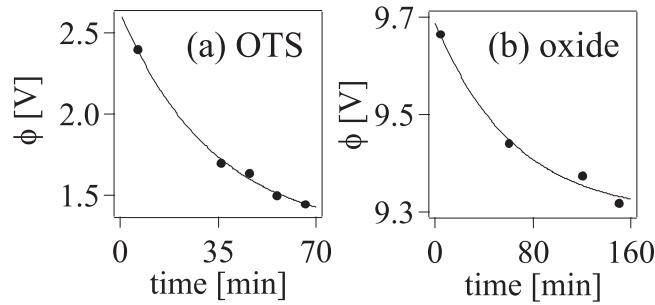
**Figure 7.12:** Potential decay of F8T2 on OTS (a) and on oxide (b).
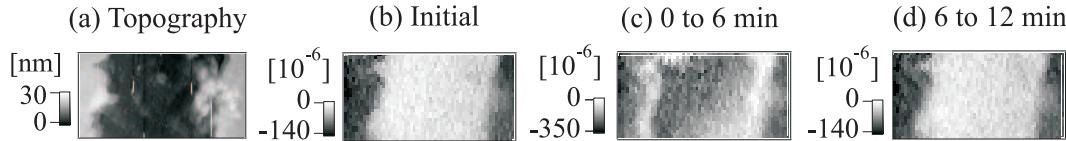
Figure 7.13: (a) Topography of a-Si. Force gradient images taken with $V_{\text{tip}} = 1\,\text{V}$ before stress (b) and after stress (c, d) with $V_g = 40\,\text{V}$. All images are $16 \times 8\,\mu\text{m}^2$.

7.2.3 a-Si

Trap release in a-Si deposited at low temperature $(130\,^{\circ}\text{C})$ is also examined with EFM. The cause of trapped charges in a-Si is attributed to two mechanisms [28–31]: defect-states creation (silicon dangling bonds) and charge trapping in the silicon nitride dielectric, which is more relevant at high gate voltage as is the case here $(V_g = 40\,\text{V})$. The release time for traps in a-Si is much faster than F8T2; Fig. 7.13(c) shows that charges are being released as the image is being taken. Since a line scan across the device takes less time, it is used to observe the potential change with time in Fig. 7.14(a) and (b). Notice the profiles are rounded due to charges being removed from near the electrodes by diffusion. The time needed for potential to decay is only 6 min.

In Fig. 7.14(c), the negative gate bias is completely shielded by positive charges to $-5\,\text{V}$, possibly due to donor dopants. After the EFM potential has decayed
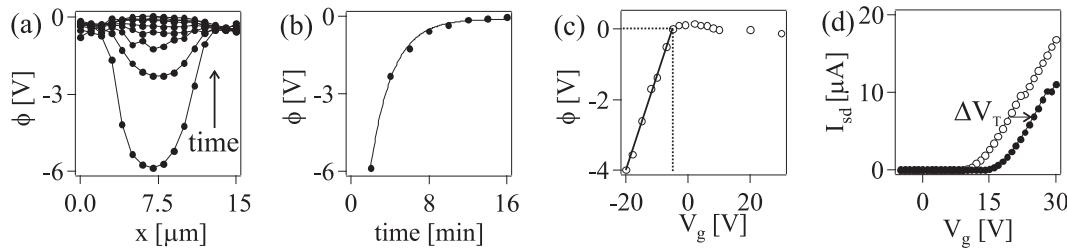
Figure 7.14: Potential decay in a-Si as a function of channel location (a) and time (b). (c) Potential versus gate bias measured before bias stress. (d) Threshold voltage shift persisted in IV transfer curves even after the EFM potential has returned to 0 V in (b).

to 0 V, the transfer characteristics are measured again. Undetectable by EFM but apparent with the IV curves, a threshold voltage shift still exists, also corresponding to 5 V. The presence of positive charges hinted in Fig. 7.14(c) might be shielding an equivalent amount of trapped electrons; therefore the EFM potential appears at 0 V despite not all the trapped electrons having been released.

7.3 Conclusions

Trap formation and dissociation is faster for devices with OTS interfaces than for devices with oxide interface. Annealing improves mobility for OTS but decreases it for oxide; there is no direct correlation between mobility and trap formation. Compared to pentacene, the trap distribution is more homogeneous in F8T2, regardless of dielectric treatment. EFM measurements on PQT are impeded by shielding charges; however, when EFM is applicable, such as for F8T2 and a-Si, it provides images of local charge distribution unavailable to other bulk measurement techniques.

CHAPTER 7 REFERENCES

[1] H. Sirringhaus, Adv. Mater. **17**, 2411 (2005), and references therein.

[2] R. A. Street, A. Salleo, and M. L. Chabinyc, Phys. Rev. B **68**, 085316 (2003).

[3] A. Salleo and R. A. Street, Phys. Rev. B **70**, 235324 (2004).

[4] A. Salleo, F. Endicott, and R. A. Street, Appl. Phys. Lett. **86**, 263505 (2005).

[5] M. Matters, D. M. de Leeuw, and P. T. H. adn A. R. Brown, Synth. Metals **102**, 998 (1999).

[6] W. A. Schoonveld, J. B. Oostinga, J. Vrijmoeth, and T. M. Klapwijk, Synth. Metals **101**, 608 (1999).

[7] G. Horowitz, R. Hajlaoui, D. Fichou, and A. E. Kassmi, J. Appl. Phys. **85**, 3202 (1999).

[8] S. J. Zilker, C. Detcheverry, E. Cantatore, and D. M. de Leeuw, Appl. Phys. Lett. **79**, 1124 (2001).

[9] H. E. Katz, X. M. Hong, A. Dodabalapur, and R. Sarpeshkar, J. Appl. Phys. **91**, 1572 (2002).

[10] A. Salleo and R. A. Street, J. Appl. Phys. **94**, 471 (2003).

[11] J. Veres, S. Ogier, G. Lloyd, and D. de Leeuw, Chem. Mater. **16**, 4543 (2004), and references therein.

[12] F. Dinelli et al., Phys. Rev. Lett. **92**, 116802 (2004).

[13] B. S. Ong, Y. Wu, P. Liu, and S. Gardner, J. Am. Chem. Soc. **126**, 3378 (2004).

[14] J. D. L. Grange and J. L. Markham, Langmuir **9**, 1749 (1993).

[15] A. Salleo, M. L. Chabinyc, M. S. Yang, and R. A. Street, Appl. Phys. Lett. **81**, 4383 (2002).

[16] X. Jiang et al., Adv. Funct. Mater. **12**, 587 (2002).

[17] Y. Y. Deng and H. Sirringhaus, Phys. Rev. B **72**, 045207 (2005).

[18] M. J. Nowak, D. Spiegel, S. Hotta, and A. J. H. adn P. A. Pincus, Macromolecules **22**, 2917 (1989).

[19] D. B. A. Rep, A. F. Morpurgo, W. G. Sloof, and T. M. Klapwijk, J. Appl. Phys. **93**, 2082 (2003).

[20] H. L. Gomes et al., Appl. Phys. Lett. **84**, 3184 (2004).

[21] R. A. Street, J. E. Northrup, and A. Salleo, Phys. Rev. B **71**, 165202 (2005).

[22] M. L. Chabinyc et al., J. Appl. Phys **96**, 2063 (2004).

[23] L. Bürgi, T. Richards, M. Chiesa, R. H. Friend, and H. Sirringhaus, Synth. Met. **146**, 297 (2004).

[24] E. M. Muller and J. A. Marohn, Adv. Mater. **17**, 1410 (2005).

[25] I. Torres, D. M. Taylor, and E. Itoh, Appl. Phys. Lett. **85**, 314 (2004).

[26] L. L. Chua et al., Nature **434**, 194 (2005).

[27] J. Veres, S. D. Ogier, S. W. Leeming, D. C. Cupertino, and S. M. Khaffaf, Adv. Funct. Mater. **13**, 199 (2003).

[28] R. A. Street, J. Zesch, and M. J. Thompson, Appl. Phys. Lett. **43**, 672 (1983).

[29] M. J. Powell, C. van Berkel, and J. R. Hughes, Appl. Phys. Lett. **54**, 1323 (1989).

[30] J. B. Choi, D. C. Yun, Y. I. Park, and J. H. Kim, J. Non-Crystall. Solids **266-269**, 1315 (2000).

[31] K. S. Karim, A. Nathan, M. Hack, and W. I. Milne, IEEE Electron Dev. Lett. **25**, 188 (2004).

Appendix A

Demagnetizing factor

In a single domain particle, it is possible to have the applied field, the demagnetizing field, and the magnetization all uniform, if the particle is in the shape of an ellipsoid. As the magnetization of the particle is rotated, the demagnetizing field changes in magnitude; thus the demagnetizing energy changes because the demagnetizing factors varies along different axes of the particle. In this appendix the equations for demagnetizing factors will be derived, and the effect of the demagnetizing factors on magnetic hysteresis will be discussed. For more detailed explanations, the original derivations can be found in Refs [1–4].

A.1   For a Sphere

The demagnetizing field H_d of a body is proportional to the magnetization which creates it:

$$H_d = -N_d M, \tag{A.1}$$

where M is the magnetization, or magnetic moment per unit volume, and N_d is the demagnetizing factor which depends mainly on the shape of the body and can be calculated exactly only for an ellipsoid. This section calculates N_d for the special case of a sphere [2].

Uniform magnetization of a sphere by an applied field H will cause north and south poles to appear on the surface, and these free poles produce the demagnetizing field H_d. Let ρ_s be the pole density on the surface of the sphere and a be the radius. To find ρ_s, note that the magnetization M of the sphere is the pole strength per unit area on the equatorial cross-section (Fig. A.1). The number of poles on an annular strip of radius r and width dr is $2\pi r M dr$. Since M is uniform
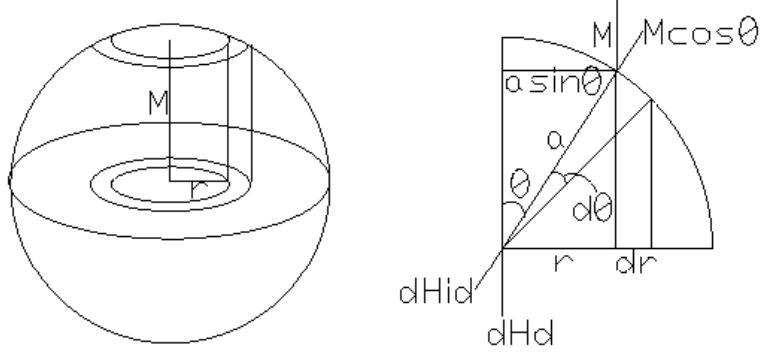
Figure A.1: Demagnetizing field at the center of a sphere.

throughout the sphere, there will be the same number of poles on an annular strip on the surface, formed by projecting the equatorial strip up to the surface. The area of this surface strip is $(2\pi a \sin\theta)(ad\theta)$. Thus the surface pole density is

$$\rho_s = \frac{2\pi r M dr}{2\pi a^2 \sin\theta d\theta}. \tag{A.2}$$

But $r = a\sin\theta$, and $dr = a\cos\theta d\theta$. Therefore,

$$\rho_s = \frac{M(a\sin\theta)(a\cos\theta)d\theta}{a^2 \sin\theta d\theta} = M\cos\theta. \tag{A.3}$$

This shows, as might be expected, that the surface density of poles is not uniform: it decreases from a maximum of M at the top and bottom to zero at the equator.

According to Coulomb's law, the force between poles is $F = p_1 p_2/4\pi d^2$, where d is the distance between them. Experiment also shows that this force is directly proportional to the product of the pole strength and field, $F = pH$, and so the field of a pole is $H = p/4\pi d^2$. The inclined demagnetizing field dH_{id} at the center of the sphere, due to poles on annular strips at the top *and* bottom of the sphere, is given by the force on a unit pole placed at the sphere center:

$$dH_{id} = -\frac{(2\rho_s)(2\pi a^2 \sin\theta d\theta)(1)}{4\pi a^2}. \tag{A.4}$$

The demagnetizing field antiparallel to M is

$$dH_d = dH_{id}\cos\theta. \tag{A.5}$$

By substituting Eq. A.3 into Eq. A.4 and integrating Eq. A.5,

$$H_d = \int dH_d = -M \int_0^{\frac{\pi}{2}} \cos^2 \theta \sin \theta d\theta = -\frac{M}{3}. \tag{A.6}$$

Therefore, the demagnetizing factor for a sphere is $N_d = 1/3$.

A.2 For Prolate and Oblate Spheroids

The general ellipsoid has three unequal axes $(2a, 2b, 2c)$ and a section perpendicular to any axis is an ellipse. A prolate spheroid is formed by rotating an ellipse about its major axis $2c$, and the resulting solid is rod-shaped with $a = b$. Rotation about the minor axis $2a$ results in the disk-shaped oblate spheroid with $b = c$. The following equations are taken out from Ref. [2]. Maxwell has also shown that $N_a + N_b + N_c = 1$ for any ellipsoid, where the subscripts a, b, and c indicate the three axes in an ellipsoid [1].

Let $c/a = r$. For a prolate spheroid, or rod, where $a = b \neq c$,

$$N_c = \frac{1}{r^2 - 1}[\frac{r}{\sqrt{r^2 - 1}} \ln (r + \sqrt{r^2 - 1}) - 1], \tag{A.7a}$$

$$N_a = N_b = \frac{1 - N_c}{2}. \tag{A.7b}$$

When r is very large (a very long rod),

$$N_a = N_b \approx \frac{1}{2}, \tag{A.8a}$$

$$N_c \approx \frac{1}{r^2}(\ln 2r - 1). \tag{A.8b}$$

N_c approaches zero as r approaches infinity.

For an oblate spheroid, or disk, where $a \neq b = c$,

$$N_a = \frac{r^2}{r^2 - 1}(1 - \sqrt{\frac{1}{r^2 - 1}} \arcsin \frac{\sqrt{r^2 - 1}}{r}), \tag{A.9a}$$

$$N_b = N_c = \frac{1 - N_a}{2}. \tag{A.9b}$$
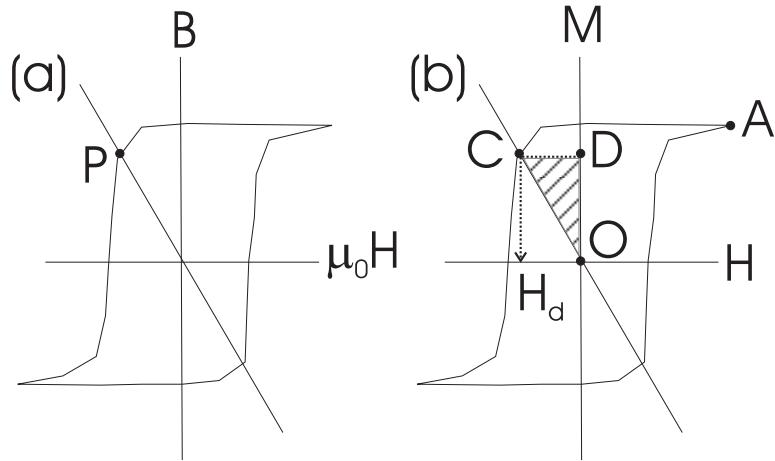
Figure A.2: (a) Internal magnetic induction in a sphere. (b) Demagnetizing energy of a magnetized body in zero applied field.

When r is very large (very thin disk),

$$N_a \approx 1, \tag{A.10a}$$

$$N_b = N_c \approx 0. \tag{A.10b}$$

N_b and N_c approach zero as r approaches infinity.

A.3 Effect of the demagnetizing factor on magnetic hysteresis

The following section will first examine how the demagnetizing factor modifies remnant magnetization [3]. Then the magnetic hysteresis of a spheroid will be calculated based on the principle of minimum energy, with the demagnetizing factor taken into account [4].

A.3.1 Remnant magnetization

For a sphere

Let us return to the specific case of a magnetized sphere in an external field. From Section A.1, the magnetic field and magnetic induction inside the sphere are

$$H_d = \frac{-1}{3}M, \tag{A.11}$$

$$B_{in} = \frac{2\mu_o}{3}M, \tag{A.12}$$

$$\tag{A.13}$$

where $B_{in} = \mu_o(M + H_d)$. Notice that B_{in} is parallel to M, while H_d is antiparallel. With a uniform external field $B_0 = \mu_0 H_0$, the magnetic induction and field are now

$$B_{in} = B_0 + \frac{2\mu_0}{3}M, \tag{A.14}$$

$$H_{in} = \frac{1}{\mu_0}B_0 - \frac{1}{3}M. \tag{A.15}$$

The above equations are solved for one relation between H_{in} and B_{in} by eliminating M,

$$B_{in} = 3B_0 - 2\mu_0 H_{in}. \tag{A.16}$$

This equation corresponds to a line with slope -2 on the hysteresis diagram with y-intercept $3B_o$ [Fig. A.2(a)]. This line shows the extra field that is required to obtain the same magnetization level compared to when the particle has zero demagnetizing field.

Another way to understand this slope is by examining the remnant magnetization. When the external field is increased until the sphere becomes saturated and then the field is turned off, the internal B_{in} and H_{in} will be given by the point marked P. The magnetization M can be found from Eq. A.14 and Eq. A.15 with $B_0 = 0$. Equation A.16 between B_{in} and H_{in} is specific to the sphere. For other

ellipsoids, the slope of the lines range from zero for a flat disk to $-\infty$ for a long needle-like object. Thus a larger internal magnetic induction can be obtained with a rod geometry than with spherical or oblate spheroidal shapes.

For a general ellipsoid

The case of a general ellipsoid has demagnetizing factor N, where

$$H_{in} = H_0 - NM. \tag{A.17}$$

The magnetic induction in an external field is

$$B_{in} = \mu_0(H_{in} + M) = \mu_0[H_0 + (1 - N)M]. \tag{A.18}$$

By eliminating M in Eqs. A.17 and A.18,

$$B_{in} = -\frac{1 - N}{N}\mu_0 H_{in} + \frac{1}{N}\mu_0 H_0. \tag{A.19}$$

This general form allows any demagnetizing factor to be added onto a given hysteresis graph to account for the demagnetizing field.

A.3.2   Magnetic hysteresis for uniaxial spheroids

A magnetic particle not parallel to the applied field must have a certain potential energy E_H relative to the parallel position. The work done in turning it through an angle $d\theta$ against the field is in the form of a torque equation

$$dE_H = \mu_0 MH \sin\theta d\theta. \tag{A.20}$$

The convention is to take the $\theta = \pi/2$ position as the zero of energy. Therefore,

$$E_H = \mu_0 \int_{\frac{\pi}{2}}^{\theta} MH \sin\theta d\theta = -\mu_0 MH \cos\theta. \tag{A.21}$$

In vector notation, $E_H = -\mu_0 \mathbf{M} \cdot \mathbf{H}$.
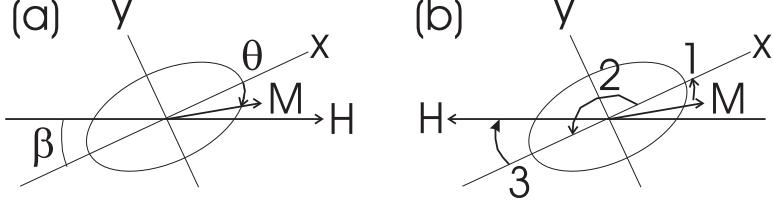
Figure A.3: Rotation of the magnetization in a spheroid. In part (a), θ indicates the direction M is heading in positive field. Part (b) shows the steps to bring M to saturation in negative field: 1) M increases until it reaches the easy axis, 2) M flips its direction to the negative field, and 3) M continues to align itself with the applied negative field.

If a body is magnetized by an applied field to some level A and the applied field is removed, the magnetization will decrease to C under the action of the demagnetizing field $\mu_0 H_d$ [Fig. A.2(b)]. Here OC is the demagnetizing field line, with a slope of $-1/N_d$. The specimen then contains stored energy E_D equal to the area of the shaded triangle OCD:

$$E_D = \frac{1}{2}\mu_0 M H_d. \tag{A.22}$$

This energy can be written in vector form as $E_D = (\mu_0/2)\mathbf{M} \cdot \mathbf{H_d}$ with H_d being antiparallel to M. Note that the above energy expressions all have units of energy per unit volume, since M is the magnetic moment per unit volume.

Since Section A.1 has shown that $N_a + N_b + N_c = 1$, if y and z are the two equal axes, then $N_b = N_c = (1 - N_a)/2$ using the variables illustrated in Fig. A.3. The expression for demagnetizing energy is given by

$$E_D = \frac{\mu_0}{2}\mathbf{M} \cdot \mathbf{H_d}V = \frac{\mu_0 M_S^2 V}{2}\left(N_a \cos^2 \theta + \frac{1 - N_a}{2}\sin^2 \theta\right), \tag{A.23}$$

where M_S is the saturation magnetization. If the applied field is nonzero, we have to add an applied field energy, E_H, to get the total energy E:

$$E_H = -\mu_0 \mathbf{M} \cdot \mathbf{H}V = -\mu_0 M_S V H \cos(\beta - \theta), \tag{A.24}$$
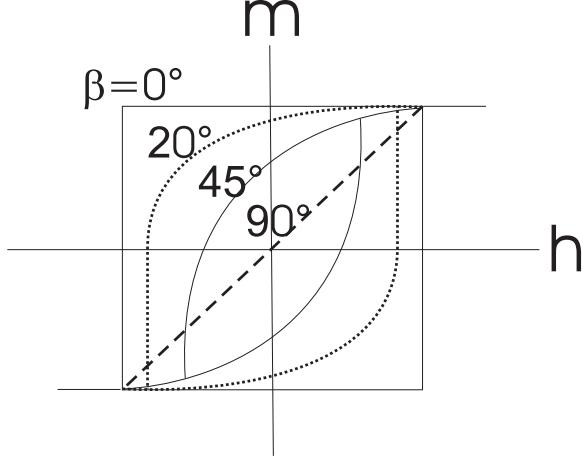
Figure A.4: Hysteresis loops for different β's in degree units.

$$E = \frac{\mu_0 M_S^2 V}{2}(N_a \cos^2\theta + \frac{1 - N_a}{2}\sin^2\theta) - \mu_0 M_S V H \cos(\beta - \theta) \qquad (A.25)$$

Eq. A.25 is an expression relating energy to applied field and magnetization angle. Since the system seeks an energy minimum, the equilibrium angle is given by

$$\frac{dE}{d\theta} = \mu_0 M_S V[C \sin\theta\cos\theta - H\sin(\beta - \theta)] = 0, \qquad (A.26)$$
$$\text{where } C = M_S \frac{1 - 3N_a}{2}.$$

To find the critical angle θ_c at which the particle switches magnetization, it must be noted that the solution to Eq. A.25 does not necessarily correspond to a minimum. It could correspond to an energy maximum, depending on the sign of the second derivative,

$$\frac{d^2E}{d\theta^2} = \mu_0 M_S V[C(\cos^2\theta - \sin^2\theta) + H\cos(\beta - \theta)] = 0. \qquad (A.27)$$

If $d^2E/d\theta^2$ is positive, the equilibrium is stable; if it is negative, the equilibrium is unstable; if it is zero, a condition of stability is just changing to one of instability (namely, magnetization switching). Solving Eqs. A.26 and A.27 simultaneously,

$$\tan^3\theta_c = -\tan\beta. \qquad (A.28)$$

For positive fields, θ approaches β monotonically as the magnetization tries to align itself with the applied field [Fig. A.3(a)]. For negative fields, θ increases until it reaches its maximum, then it switches [Fig. A.3(b)].

Figure A.4 shows the reduced hysteresis loops for different β angles. While m decreases with increasing β at a given field, the hysteresis loop is squashed from a square loop to a slanted line. When β increases from zero, the critical field decreases until $\beta = \pi/4$, and then increases back to the value it had at $\beta = 0$ at $\beta = \pi/2$.

APPENDIX A REFERENCES

[1] J. C. Maxwell, *A Treatise on Electricity and Magnetism*, volume 2, chapter 437 and 438, Dover Publications, 3rd edition, 1954.

[2] B. D. Cullity, *Introduction to Magnetic Materials*, Addison–Wesley Co., Reading, MA, 1972.

[3] J. D. Jackson, *Classical Electrodynamics*, John Wiley & Sons, 3rd edition, 1998.

[4] E. D. Torre, *Magnetic Hysteresis*, IEEE Press, 1999.

Appendix B

Experimental setup in frequency-shift cantilever magnetometry

The frequency-shift cantilever magnetometer is housed in a high vacuum chamber which is essentially a long, narrow tube for direct insertion into a cryogenic dewar [1]; Appendix C of William Silveira's Ph.D. thesis [2] has an excellent description of a vacuum probe design connected with electrical and fiber-optic feedthroughs [3]. The probe shown in Fig. B.1 allows two cantilevers to be mounted inside the chamber. During experiment, the cantilever under study is positioned inside the magnet center by adjusting the height of the anchoring clamp along the vacuum tube. This arrangement let two samples to be cooled simultaneously and saves time in switching between samples. The magnetometer's positive feedback circuit and fiber-optic interferometer are constructed using the design presented in Chapter 3 of Erik Muller's doctoral thesis [4].

For external magnetic field a 6 T superconducting magnet, kindly loaned to us by Professor Jeevak Parpia, is used; its specifications are detailed in Fig. B.2 and Table B. A four-quadrant power supply (Model 4Q-05100, American Magnetics, Inc., Oak Ridge, Tennessee) provides current to the magnet, with connections [Table B] between the equipments as illustrated in Fig. B.3. The magnet operates in a cryogenic dewar purchased from Cryomagnetics, Inc. (Oak Ridge, Tennessee); Figs. B.4 and B.5 are diagrams showing the dewar's dimensions.
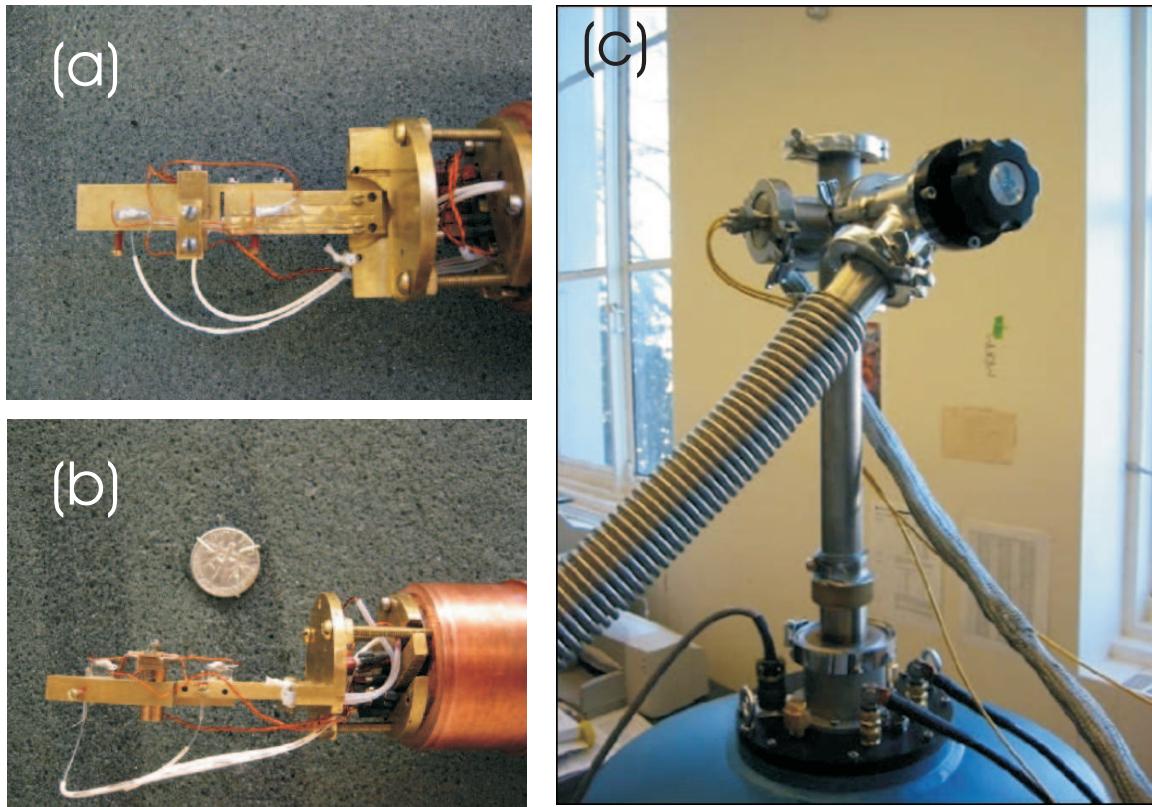
Figure B.1: Magnetometry setup. Topview (a) and sideview (b) of the probe head. (c) Vacuum probe placed inside dewar.

Table B.1: Magnet specifications

Rated central field	6.0 T at 4.2 K
Maximum test field	6.6 T at 4.2 K
Rated current (6 T)	43.1 A
Inductance	5.3 H
Homogeneity	±0.5 % over 1 cm DSV
Field to current ratio	0.1392 T/A
Charging voltage	1.0 V
Persistent switch heater	55 mA
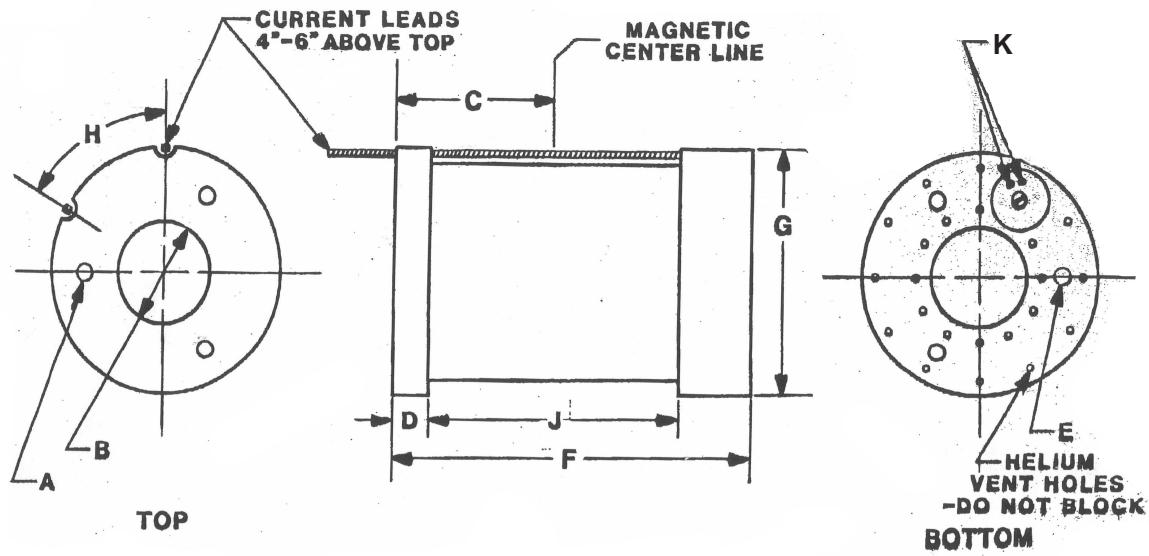
Figure B.2: Specifications of the 6 T superconducting magnet. A: 3 holes each 10-32 tapped 120° apart on a 3.312" circle. B: 2" clearance. C: 2.312" distance. D: 0.375" thickness. E: same as A. F: 5.5" total length. G: 3.90" diameter. H: 60° between current leads. J: 3.875" length. K: persistant switch heater terminal.

Table B.2: Control cable between magnet and equipments

Dewar pin #	Electrical connection
A	persistent switch heater
B	persistent switch heater
C	magnet voltage tap(+)
D	magnet voltage tap(-)
E	I(+) He level sensor
F	I(-) He level sensor
G	V(+) He level sensor
H	V(-) He level sensor
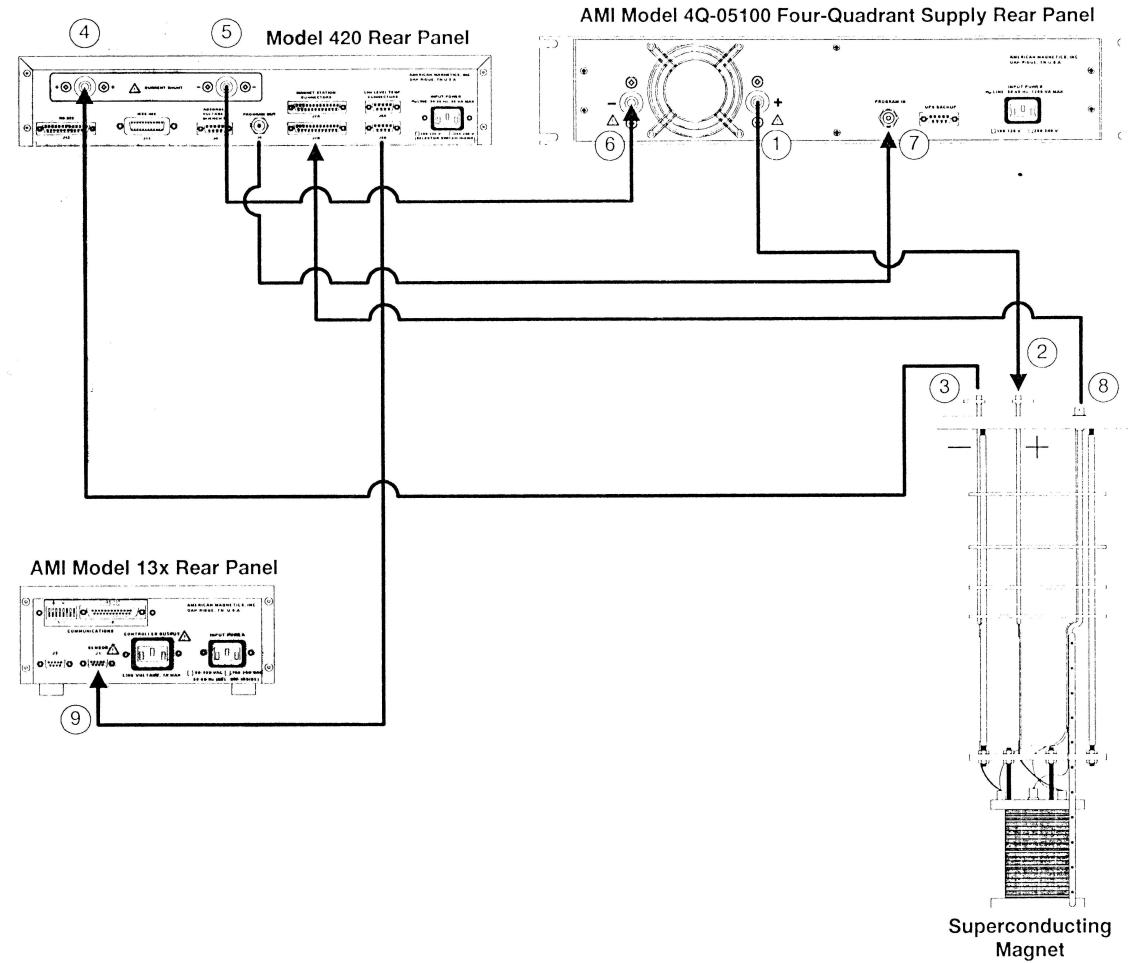
Figure B.3: Connections between the magnet and its power supply.
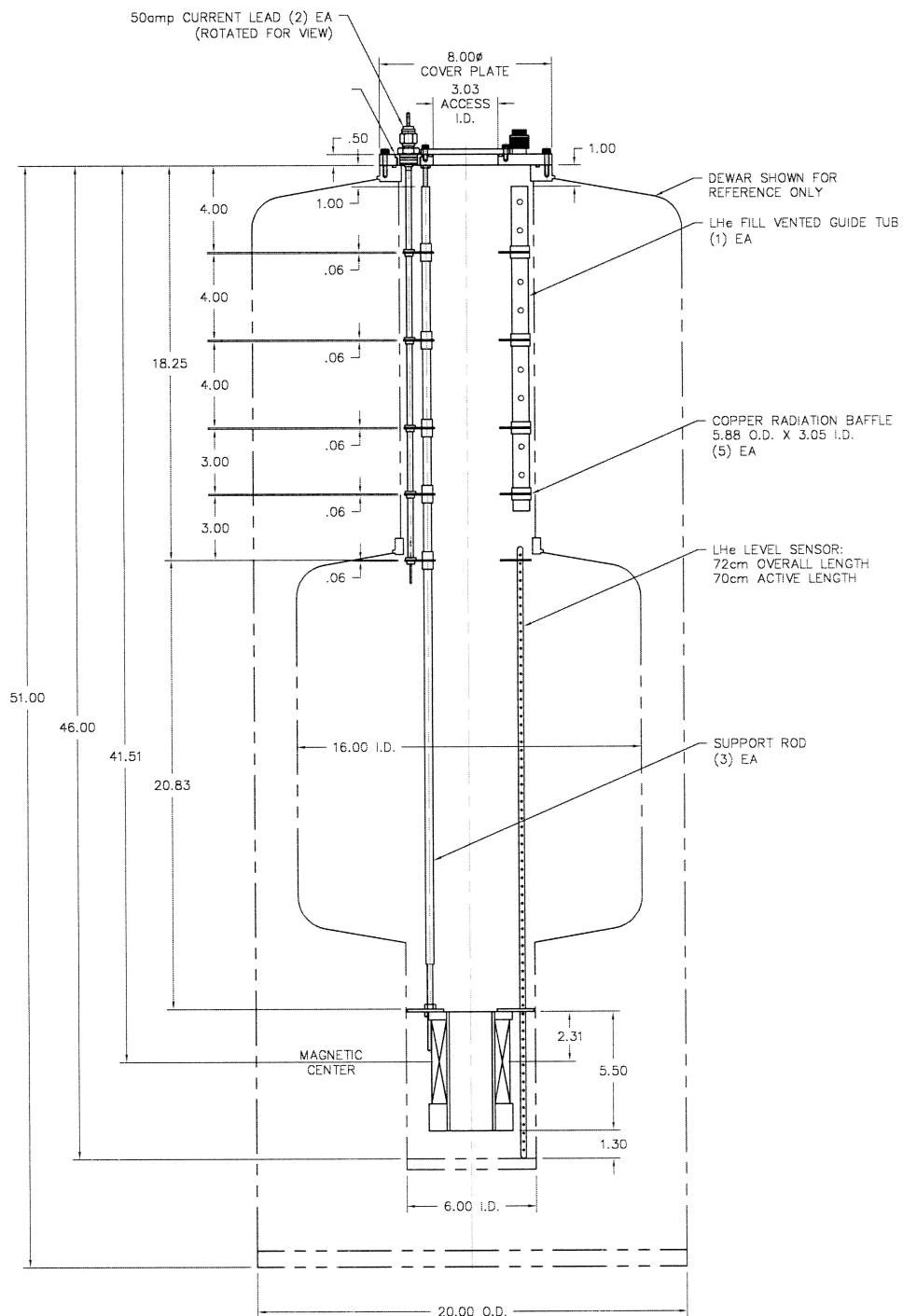
**Figure B.4:** Dimensions of the cryogenic dewar. Units are in inches.
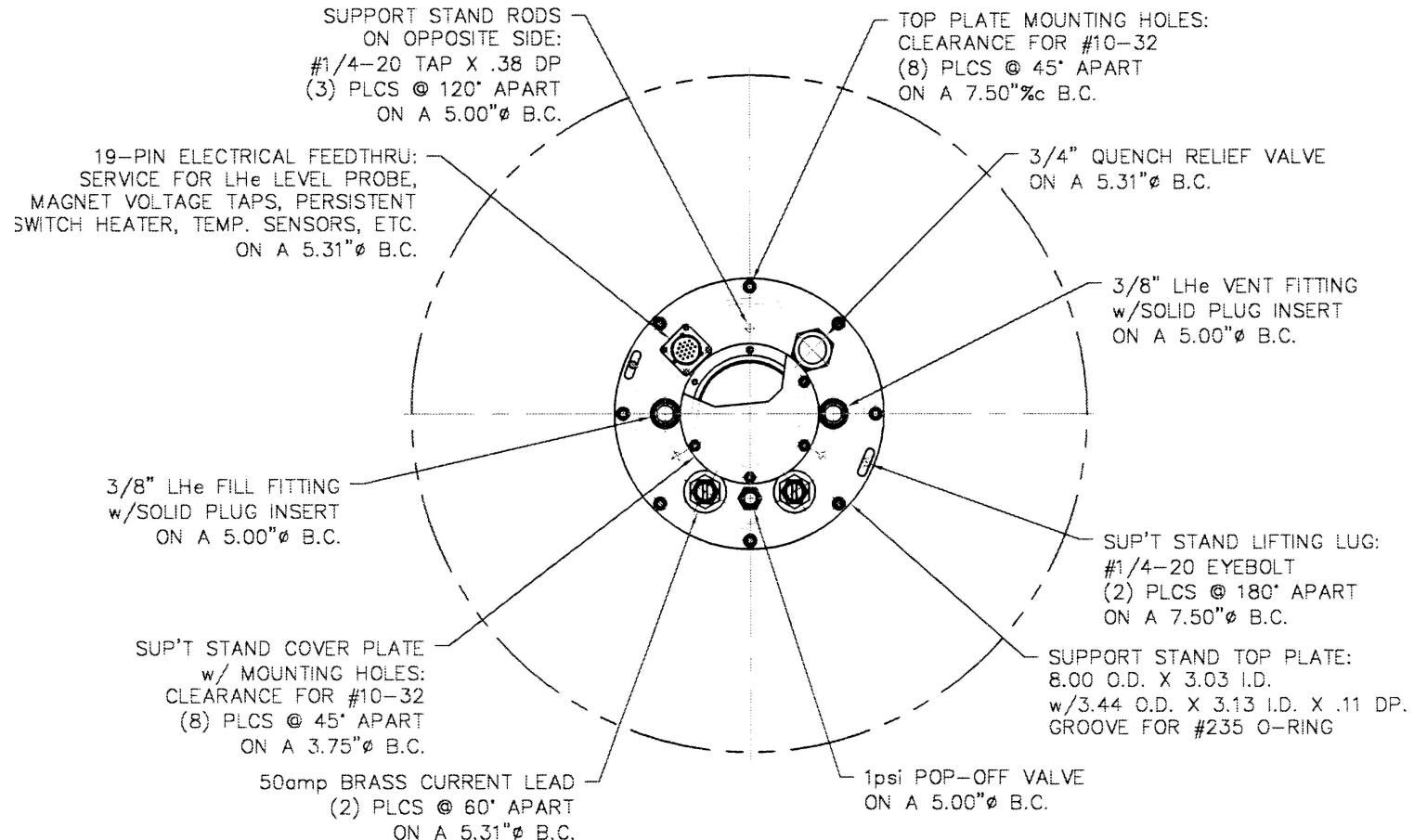
Figure B.5: Design of the dewar top plate. Units are in inches.

SUPPORT STAND RODS
ON OPPOSITE SIDE:
#1/4−20 TAP X .38 DP
(3) PLCS @ 120° APART
ON A 5.00"∅ B.C.

TOP PLATE MOUNTING HOLES:
CLEARANCE FOR #10−32
(8) PLCS @ 45° APART
ON A 7.50"∅c B.C.

19−PIN ELECTRICAL FEEDTHRU:
SERVICE FOR LHe LEVEL PROBE,
MAGNET VOLTAGE TAPS, PERSISTENT
SWITCH HEATER, TEMP. SENSORS, ETC.
ON A 5.31"∅ B.C.

3/4" QUENCH RELIEF VALVE
ON A 5.31"∅ B.C.

3/8" LHe VENT FITTING
w/SOLID PLUG INSERT
ON A 5.00"∅ B.C.

3/8" LHe FILL FITTING
w/SOLID PLUG INSERT
ON A 5.00"∅ B.C.

SUP'T STAND LIFTING LUG:
#1/4−20 EYEBOLT
(2) PLCS @ 180° APART
ON A 7.50"∅ B.C.

SUP'T STAND COVER PLATE
w/ MOUNTING HOLES:
CLEARANCE FOR #10−32
(8) PLCS @ 45° APART
ON A 3.75"∅ B.C.

SUPPORT STAND TOP PLATE:
8.00 O.D. X 3.03 I.D.
w/3.44 O.D. X 3.13 I.D. X .11 DP.
GROOVE FOR #235 O−RING

50amp BRASS CURRENT LEAD
(2) PLCS @ 60° APART
ON A 5.31"∅ B.C.

1psi POP−OFF VALVE
ON A 5.00"∅ B.C.

APPENDIX B REFERENCES

[1] R. C. Richardson and E. N. Smith, *Experimental Techniques in Condensed Matter Physics at Low Temperatures*, Addison-Wesley, Reading, MA, 1988.

[2] W. R. Silveria, *Microscopic View of Charge Injection in a Model Organic Semiconductor*, doctoral dissertaion, Cornell University, 2005.

[3] E. R. I. Abraham and E. A. Cornell, Applied Optics **37**, 1762 (1998).

[4] E. M. Muller, *Electric Force Microscopy of Charge Trapping in Thin-film Pentacene*, doctoral dissertation, Cornell University, 2005.

Appendix C

Superparamagnetism: critical volume

and blocking temperature

Hysteresis will appear and superparamagnetism disappears, when particles of a certain size are cooled to a particular temperature, or when the particle increases beyond a particular volume V_c at constant temperature. To determine the critical values for superparamagnetism, we should consider the rate at which thermal equilibrium is reached. The following derivations are taken from Refs. [1,2].

C.1   Critical volume and blocking temperature

Suppose an assembly of uniaxial particles has been brought to some initial state of magnetization M_i by an applied field, and the field is then turned off at time $t = 0$. Some particles in the assembly will immediately reverse their magnetization because they possess thermal energy larger than average, and the magnetization of the assembly will begin to decrease. The rate of decrease is proportional to the magnetization and to the Boltzmann factor $exp(-KV/k_BT)$, since this exponential gives the probability of whether a particle has enough thermal energy to surmount the energy gap $\triangle E = KV$ required for reversal, where K is the anisotropy constant. Thus

$$-\frac{dM}{dt} = CMe^{-KV/k_BT} = \frac{M}{\tau} \tag{C.1}$$

Here the proportionality constant C is a frequency factor approximately equal to the Larmor precession frequency ($\sim 10^9$ Hz); this value is slightly field dependent, but this dependence will be ignored here. The constant τ is the relaxation

time. To find how the remanence M_r decreases with time we rearrange the terms in Eq. C.1 and integrate to obtain

$$M_r = M_i e^{-t/\tau}. \tag{C.2}$$

The meaning of τ is now apparent; it is the time for M_r to decrease to $1/e$ of its initial value. From Eq. C.1 we have

$$\frac{1}{\tau} = Ce^{-KV/k_B T}. \tag{C.3}$$

Because τ varies so rapidly with V, it follows that relatively small changes in τ do not change the corresponding value of V by much. Therefore it is possible to define an upper limit V_c for superparamagnetic behavior by rather arbitrarily assigning a value of $\tau = 100$ sec to mark the transition to stable magnetization. (If τ is increased to, say, 1000 sec, the corresponding value of V_c would increase only by 9 percent.) Equation C.3 becomes $10^{-2} = 10^9\ exp(-KV_c/k_B T)$. The transition to stable behavior occurs when the energy becomes $\geq 25\ k_B T$, and so $V_c = 25\ k_B T/K$ for uniaxial particles. For particles of constant size there will be a blocking temperature T_B, below which the magnetization will be stable. For uniaxial particles with the same criterion of stability as above, the equation can be rearranged to obtain $T_B = KV/25k_B$.

C.2 Effect of an applied field

Given a uniaxial particle with its easy axis parallel to the z axis, let it be initially saturated in the $+z$ direction. A field H is then applied in the $-z$ direction, so that M_s makes an angle θ with $+z$. The total energy is then $E = V(K \sin^2 \theta + HM_s \cos \theta)$. The energy barrier for reversal is the difference between the maximum

and minimum values of E,

$$\Delta E = KV \left[1 - \left(\frac{HM_s}{2K} \right)^2 \right]. \tag{C.4}$$

The barrier is therefore reduced by the field. Particles larger than V_c are stable in zero field; but when a field is applied, the energy barrier can be reduced to $25 \, k_B T$, which will permit thermally activated reversal in 100 sec. This field will be the coercivity H_c, given by

$$H_c = \frac{2K}{M_s} \left(1 - \frac{25 k_B T}{KV} \right)^{1/2}. \tag{C.5}$$

As V becomes very large or when T approaches zero, H_c becomes $2K/M_s$, the coercivity when the switching field is unaided by thermal energy.

APPENDIX C REFERENCES

[1] B. D. Cullity, *Introduction to Magnetic Materials*, Addison–Wesley Co., Reading, MA, 1972.

[2] E. D. Torre, *Magnetic Hysteresis*, IEEE Press, 1999.